THERMOELECTRIC PROPERTIES OF NATURAL MINERAL BASED TETRAHEDRITE COMPOUNDS

By

Xu Lu

A DISSERTATION

Submitted to
Michigan State University
in partial fulfillment of the requirements
for the degree of

Physics-Doctor of Philosophy

2014

ABSTRACT

THERMOELECTRIC PROPERTIES OF NATURAL MINERAL BASED TETRAHEDRITE COMPOUNDS

BY

Xu Lu

With increasing demand in world's energy market and enormous green house gas emission, thermoelectric (TE) materials have become a hot research topic in condensed mater physics and energy-related materials science, since they can directly generate electricity when temperature gradient is applied, which indicates the potential use for waste heat recovery. A good TE material should have low thermal conductivity, low electrical resistivity and high Seebeck coefficient. However, the above parameters are coupled inherently and it is difficult to optimize one parameter without having negative effects on another. Furthermore, the large scale application of TE materials is limited by the low cost/efficiency ratio due to the component expensive/toxic elements and complex synthesis processes.

In this work, a new compound $Cu_{12}Sb_4S_{13}$ tetrahedrite with predicted intrinsic low thermal conductivity is synthesized and characterized systematically for its thermoelectric properties. The origin of intrinsic low thermal conductivity is investigated by both theoretical and experimental work. The effects of foreign atom substitution on TE properties of tetrahedrite are studied with the conclusion that TE properties of this compound are not as sensitive to impurities as is typically the case for TE materials.

In addition, band structure engineering is performed on tetrahedrite by Ni and Zn co-doping and Se substitution. Nickel substitution introduces new energy levels near the Fermi level, Zn plays the role or raising the Fermi level to the top of valence band, optimizing electrical transport properties for TE application. Selenium substitution in tetrahedrite decouples the three inter-

dependent parameters determining TE behavior by increasing band degeneracy near the Fermi level.

Finally, a rapid and economic method which directly uses natural mineral itself is developed for synthesizing tetrahedrite based TE materials. By high energy mixing of tetrahedrite natural mineral powder and pure elemental powders, TE materials with high performance can be produced in large quantities in a very short time.

Overall, we identify a new family of compounds based on a natural mineral as high performance TE materials with intrinsically low thermal conductivity. Our new method of directly using natural mineral in TE material synthesis demonstrates a new route to large scale thermoelectric applications.

To my parents, grandmother and all my friend

ACKNOWLEDGEMENTS

I would like to sincerely thank those who contributed to this research project. It is my great honor and luck to work in Professor Morelli's lab. He was always kind and patient with me, leading me to the field of thermoelectrics and teaching me experimental skills and the physics hidden behind data. I am also very grateful to my other committee members for their insightful suggestions to improve my research.

Many thanks go to my colleagues Dr. Chen Zhou, Dr. Chang Liu, Dr. Long Zhang, Dr . Eric Skoug, Dr. Hui Sun, Mr. Peng Gao and Dr. Ponnnambalam Vijayabarathi who shared their valuable experience with me. The help from other group members Mr. Hao Yang, Dr. Steve Boona, Dr. Gloria Lehr, Mr. Winston Carr, Mr. Jared Williams, Mr. Spencer Waldrop and Ms. Jing Kong are greatly appreciated.

I was also very fortunate to have the opportunity to work in the RMSSEC Energy Frontier Research Center with talented collaborators from UCLA, Oak Ridge National Lab, University of Michigan, Northwestern University and Wayne State University. Special thanks are given to Professor Vidvuds Ozolins, Mr. Yi Xia and Dr. Edgar Lara-Curzio. Their successful theoretical calculations and advanced characterization are parts of my dissertation work.

Last but not least, I would like to thank my parents and grandmother, who believed in me and gave their unconditional love and support to me when I needed it most. I also want to thank all my friends home and abroad, who encouraged me to work hard and achieve my final goal.

TABLE OF CONENTS

LIST OF FIGURES

Chapter 1 Introduction to Thermoelectrics

1.1 The thermoelectric effects

The thermoelectric (TE) effects include the Seebeck effect and its inverse process - the Peltier effect, which were discovered by Thomas J. Seebeck in 1823 and Jean C. A Peltier in 1834, respectively. The Seebeck effect can generate electricity through temperature gradient and thus has the potential use for waste heat recovery and power generation. Meanwhile the Peltier effect involves the process of producing a temperature gradient when the electrical current is applied. This effect can be used for solid state thermal cooling and accurate temperature control. These two effects associated with flows of heat and electricity are found to be thermodynamically reversible processes. To simplify the demonstration of thermoelectric phenomena and the definitions of their coefficients for isotropic homogeneous media, the "pseudo-thermostatic" method of Kelvin is applied in the later discussion[1].

Figure 1 shows a schematic circuit of two different conductors, A and B, with junctions at temperature $T_0$and $T = T_0 + \Delta T$. In an experiment, an electro-motive force (emf, also considered as open circuit voltage) is observed between A and B when ΔT is applied and satisfies the equation :

$$E_{AB} = S_{AB} * \Delta T \tag{1}$$

Here E_{AB} is the emf between A and B and S_{AB} is defined as the relative Seebeck coefficients between A and B.

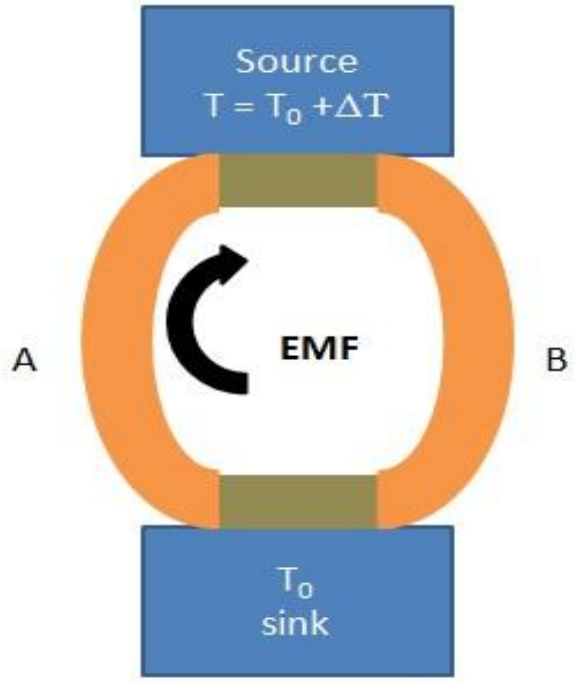

Figure 1 Illustration of Seebeck effect.

It is also found in experiment that for any pair of conductors the relative Seebeck coefficient is the difference between quantities of two individual Seebeck coefficients for each conductor, which are termed as the absolute Seebeck coefficients, S,

$$S_{AB} = S_A - S_B \tag{2}$$

The Peltier effect is described in Figure 2. When an electric current passes through a circuit composed of two different conductors A and B, heat is evolved at one junction and absorbed at the other. In an experiment, the rate of heat absorption or evolution at the junctions is proportional to the current and the nature of these two conductors, following the equation:

$$\dot{Q_{AB}} = \pi_{AB} * I \tag{3}$$

in which, π_{AB} is defined as the relative Peltier coefficient and I is the current. Also, the absolute Peltier coefficients are introduced such that

$$\pi_{AB} = \pi_A - \pi_B \tag{4}$$

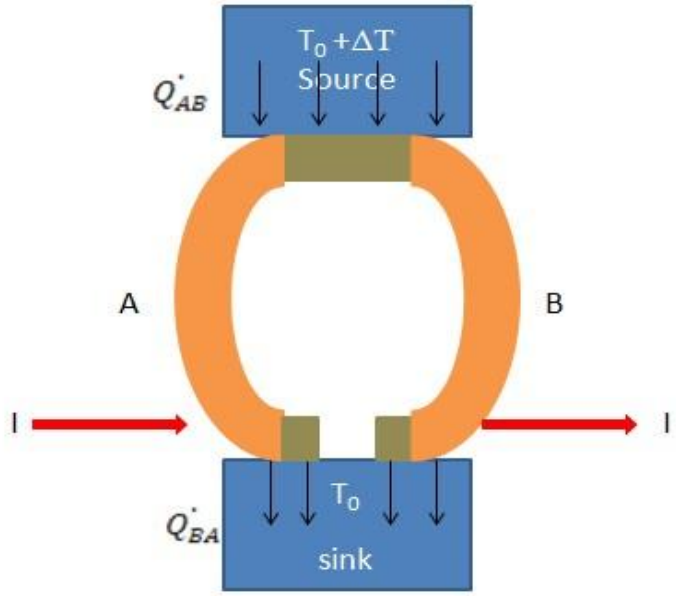

Figure 2 Illustration of Peltier effect.

In order to derive the absolute Seebeck/Peltier coefficients and the relationship between them, William Thomson predicted a new effect related to a thermodynamically reversible heat absorption/evolution in a conductor carrying an electrical current and also with the presence of a temperature gradient. This effect was subsequently proved by experiment and named as the Thomson effect.

$$\dot{q_A} = \tau_A * I * \frac{dT}{dx} \tag{5}$$

Here $\dot{q}_A$ is the rate of heat absorption/evolution per unit length of conductor, τ_A is the Thomson coefficient and $\frac{dT}{dx}$ is temperature gradient. Evidently, the Thomson coefficient can be directly measured in experiment.

In the derivation of the relations among these thermoelectric coefficients, Thomson postulated that the first and second laws of thermodynamics can be applied to these thermoelectric effects, although some irreversible processes like Joule heating and thermal conduction are also involved. In fact, these irreversible processes are the main causes for the fact that the efficiency of thermoelectric generators is always below the Carnot value of an ideal heat engine.

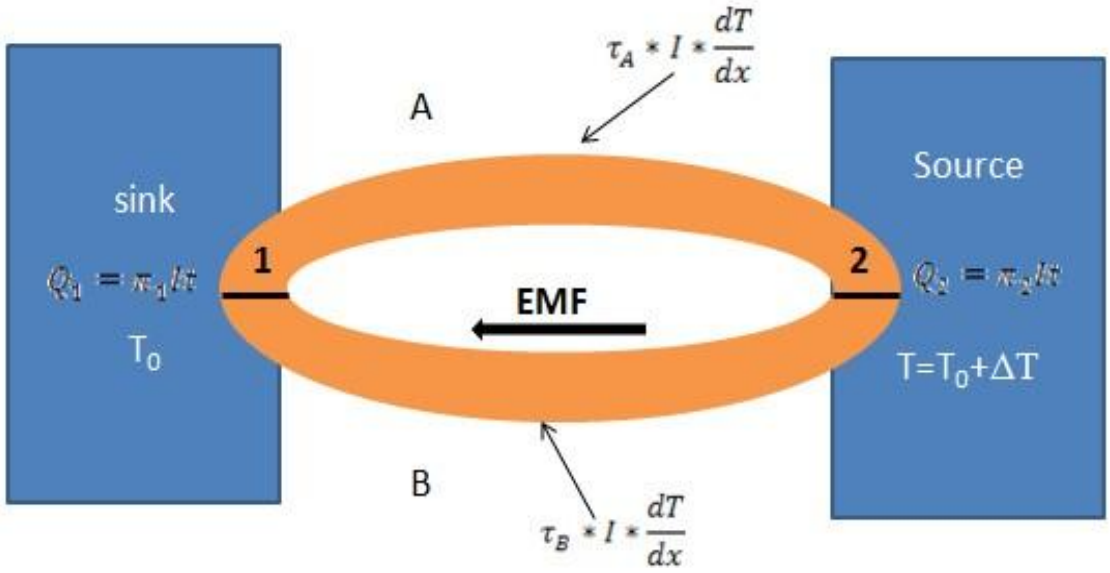

Figure 3 Illustration of an imaginary thermoelectric circuit.

Imagine a thermoelectric cycle depicted in Figure 3, consisting of two different conductors A and B, connected to one heat source and one heat sink. According to the first law of thermodynamics, considering one unit charge q passing completely around the whole circuit in the time interval t, the work done on this charge by the Seebeck emf E must equal the thermal energy absorbed during this process. The work done by the Seebeck effect can be written as :

$$W = EIt = E\frac{q}{t}t = Eq \tag{6}$$

The thermal energy absorbed in this process can be divided into two parts : Q_P by the Peltier effect and Q_T by the Thomson effect. From equation 3, total thermal energy absorbed in the Peltier effect at two ends 1 and 2

$$Q_P = Q_1 - Q_2 = \pi_1 It - \pi_2 It = (\pi_1 - \pi_2)q \tag{7}$$

Consider a charge q passing through an infinite small section of length dx on conductor B with temperature gradient dT in time interval dt. Based on equation 5, the thermal energy absorbed on B $Q_B$is

$$\dot{q_B} = \frac{dQ_B}{dt * dx} = \tau_B * I * \frac{dT}{dx}$$

$$\frac{dQ_B}{dt} = \tau_B * I * dT = \tau_B * \frac{q}{dt} * d$$

$$Q_B = \int_{T_0}^{T_{0+\Delta T}} \tau_B \, q dT$$

Therefore, the total thermal energy absorbed by the Thomson effect is

$$Q_T = Q_B - Q_A = \int_{T_0}^{T_{0+\Delta T}} (\tau_B - \tau_A) q \, dT \tag{8}$$

Combining equation 6-8, we have

$$Eq = Q_P + Q_T = (\pi_1 - \pi_2) q + \int_{T_0}^{T_{0+\Delta T}} (\tau_B - \tau_A) \, q dT$$

and thus

$$E = (\pi_1 - \pi_2) + \int_{T_0}^{T_{0+\Delta T}} (\tau_B - \tau_A) \, dT \tag{9}$$

As required by the second law of thermodynamics, the total change in entropy of the system caused by the passage of unit charge must be zero. Since the change of electrical energy of the system after this process is zero, the change in entropy of the thermal energy part must be zero as well. So we have

$$0 = \frac{Q_1}{T_0} - \frac{Q_2}{T_0 + \Delta T} + \int_{T_0}^{T_{0+\Delta T}} \frac{(\tau_B - \tau_A)}{T} q \, dT$$

$$0 = \frac{\pi_1}{T_0} - \frac{\pi_2}{T_0 + \Delta T} + \int_{T_0}^{T_{0+\Delta T}} \frac{(\tau_B - \tau_A)}{T} dT \tag{10}$$

By taking the derivatives of equations 9 and 10 with respect to temperature,

$$S = \frac{dE}{dT} = \frac{d\pi}{dT} + \tau_B - \tau_A \tag{11}$$

$$0 = \frac{d\pi}{dT} - \frac{\pi}{T} + \tau_B - \tau_A \tag{12}$$

Subtracting equation 12 from equation 11 yields

$$\pi = S * T \tag{13}$$

By differentiating equation 13 on both sides with respect to temperature and replacing S with equation 11we find

$$\frac{d\pi}{dT} = S + T\frac{dS}{dT} = \frac{d\pi}{dT} + \tau_B - \tau_A + T\frac{dS}{dT}$$

Therefore,

$$\tau_A - \tau_B = T\frac{dS}{dT} \tag{14}$$

From equation 14, it is natural to regard the absolute Seebeck coefficient of A at certain temperature T as given by

$$S_A = \int_0^T \frac{\tau_A}{T} dT \tag{15}$$

From equation 13, we have

$$\pi_A = S_A * T \tag{16}$$

Since τ_A is the physical parameter we can measure, the absolute Seebeck coefficient and Peltier coefficient are also measurable.

1.2 The efficiency of thermoelectric device

Thermoelectric devices are usually composed of a series of unicouples, each of which has one p-type leg and one n-type leg connected by a metal plate. As we mention above, these devices can convert heat into electricity (shown in Figure 4 left) as a power generator or generate

temperature gradient under electrical current (Figure 4 right) as a heat pump. Since all the work done here in this research is based on waste heat recovery, we choose the generator model to demonstrate the efficiency of thermoelectric devices[2].

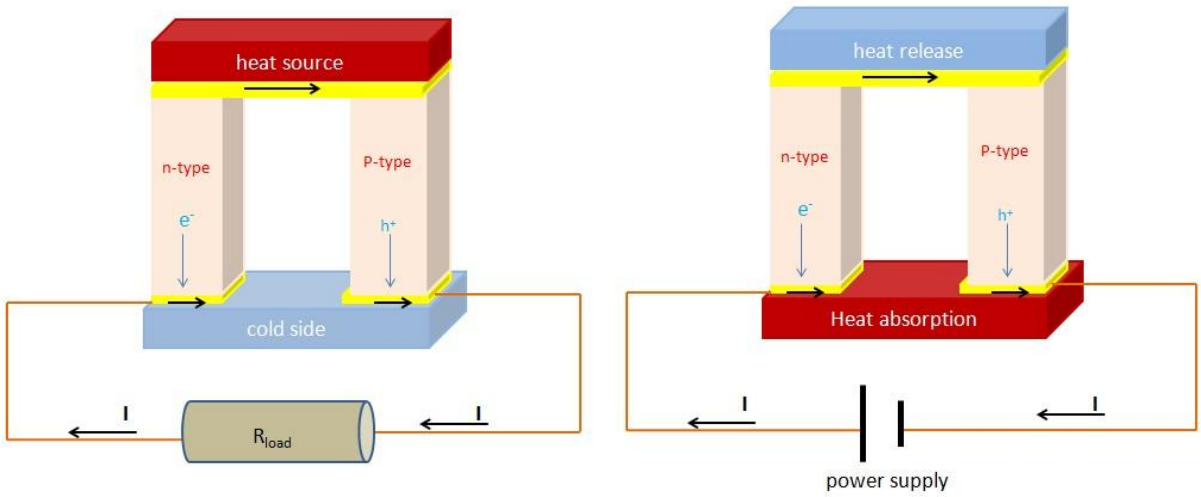

Figure 4 Illustration of a thermoelectric unicouple for power generation (left) and cooling (right).

The definition of efficiency is the output power divided by the total heat absorbed from the heat sink per unit time. According to Ohm's law, the electrical current flowing through the unicouple is written as:

$$I = \frac{V}{R} = \frac{(S_p - S_n)\Delta T}{R_p + R_n + R_L} \tag{17}$$

in which S_p is the Seebeck coefficient of p-type leg, S_n is the Seebeck coefficient of n-type leg (negative number); ΔT is the temperature difference between hot side T_h and cold side T_c; R_p, R_n and R_L are electrical resistivity of p-type leg, n-type leg and load. The total heat absorbed from the heat sink has three parts:

1) the heat absorption from the Peltier effect per unit time according to equations 7 and 16

$$Q_p = (\pi_P - \pi_n) * I = (S_P - S_n) * T_h * I \tag{18}$$

2) the heat transferred from hot to cold side through conductance

$$Q_c = \left(K_p + K_{n)}\right) * \Delta T \tag{19}$$

where K_p and K_n are thermal conductance of p-type and n-type legs; and

3) the subtraction of half of the Joule heat that is returned to the heat sink per unit time

$$Q_J = \frac{1}{2} I^2 \left(R_p + R_n\right) \tag{20}$$

From equation 17-20, we have

$$\eta = \frac{W}{Q} = \frac{I^2 R_L}{\left(S_p - S_n\right) * T_h * I \ + \left(K_p + K_{n)}\right) * \Delta T - \frac{1}{2} I^2 \left(R_p + R_n\right)} \tag{21}$$

Here we introduce the relative Seebeck coefficient $S_{pn} = S_p - S_n$, reduced resistivity $r = \frac{R_L}{R_p + R_n}$, and figure of merit $Z_{pn} = \frac{S_{pn}^2}{\left(K_p + K_{n)}\right) * (R_p + R_n)}$, so equation 21 can be rewritten as

$$\eta=\frac{\Delta T}{T_h}*\frac{r}{(1+r)+\frac{(1+r)^2}{Z_{pn}*T_h}-\frac{\Delta T}{2T_h}} \tag{22}$$

As shown in equation 22, the efficiency is a function of r. So η will reach maximum a value when $\frac{d\eta}{dr}=0$. This leads to $r=(1+\frac{Z_{pn(T_h+T_c)}}{2})^{\frac{1}{2}}$ and thus

$$\eta_{max}=\frac{\Delta T}{T_h}*\frac{\left(1+Z_{pn}\bar{T}\right)^{\frac{1}{2}}-1}{\left(1+Z_{pn}\bar{T}\right)^{\frac{1}{2}}+\frac{T_c}{T_h}} \tag{23}$$

where $\bar{T}$ is the average temperature $(T_h+T_c)/2$. It is easily found out that the maximum efficiency is the product of the Carnot efficiency limit and a function of Z_{pn}. The η_{max} is increasing monotonically with increased Z_{pn} at fixed temperatures. For an actual unicouple, $Z_{pn}$is not fixed, but related to the dimensions of the two legs. It can be maximized when the product $\left(K_p+K_{n)}\right)*(R_p+R_n)$ is minimized.

By definitions, thermal conductance $K=\frac{\kappa A}{l}$ and electrical resistance $=\frac{\rho l}{A}$, in which κ is thermal conductivity, ρ is electrical resistivity, A is the crossing area of legs and l is the length of legs. When the dimensions satisfy the relation $\frac{l_nA_p}{l_pA_n}=\left(\frac{k_n\rho_p}{k_p\rho_n}\right)^{\frac{1}{2}}$, the Z_{pn} is maximized. The figure of merit is then expressed as:

$$Z=\frac{S_{pn}^2}{\left[\left(k_p\rho_p\right)^{\frac{1}{2}}+\left(k_n\rho_n\right)^{\frac{1}{2}}\right]^2} \tag{24}$$

Practically, based on equation 24, we simply choose best p-type and n-type materials by their own Z values:

$$Z = \frac{S^2}{k\rho} \tag{25}$$

Here Z is a function of T and has the dimension of inverse T. From equation 23, it is more convenient to use T , a dimensionless quantity, to evaluate efficiency of thermoelectric devices. Therefore, the primary aim of thermoelectric research is to find materials with high Seebeck coefficient, large electrical conductivity, and low thermal conductivity in order to convert heat to electricity efficiently.

Figure 5 shows the efficiency of ideal TE devices with different ZT values at various temperature and efficiencies of traditional mechanical heat engines[reproduced from ref. 3].

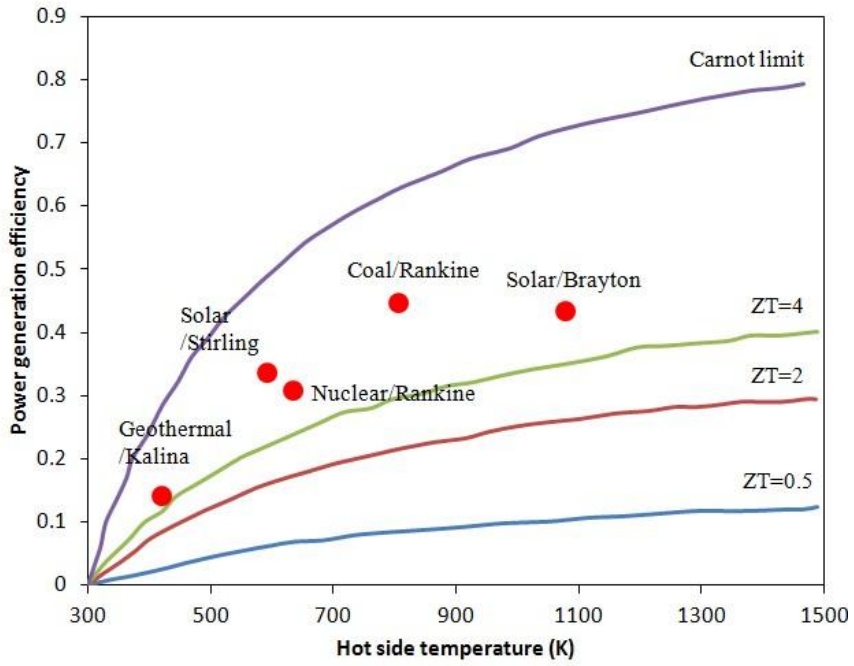

Figure 5 Thermoelectric power generation efficiency in terms of hot side temperature as cold side is fixed at 300 K. Efficiency of other conventional engines are also shown.

As Vining [4] pointed out in his review article, TE devices cannot compete with traditional engine in efficiency in the near future. However, power generation based on TE materials still has some advantages: quietness, compactness and more importantly the fact that the low-level waste heat energy with 0% efficiency may be converted into useful electricity with 7-8% efficiency or higher. In this case, energy cost becomes more meaningful than energy efficiency alone, if we can reduce the cost of TE materials/devices to a reasonable value. Considering the cost/efficiency trade off in TE power generation, we believe it will play an important role in waste heat recovery.

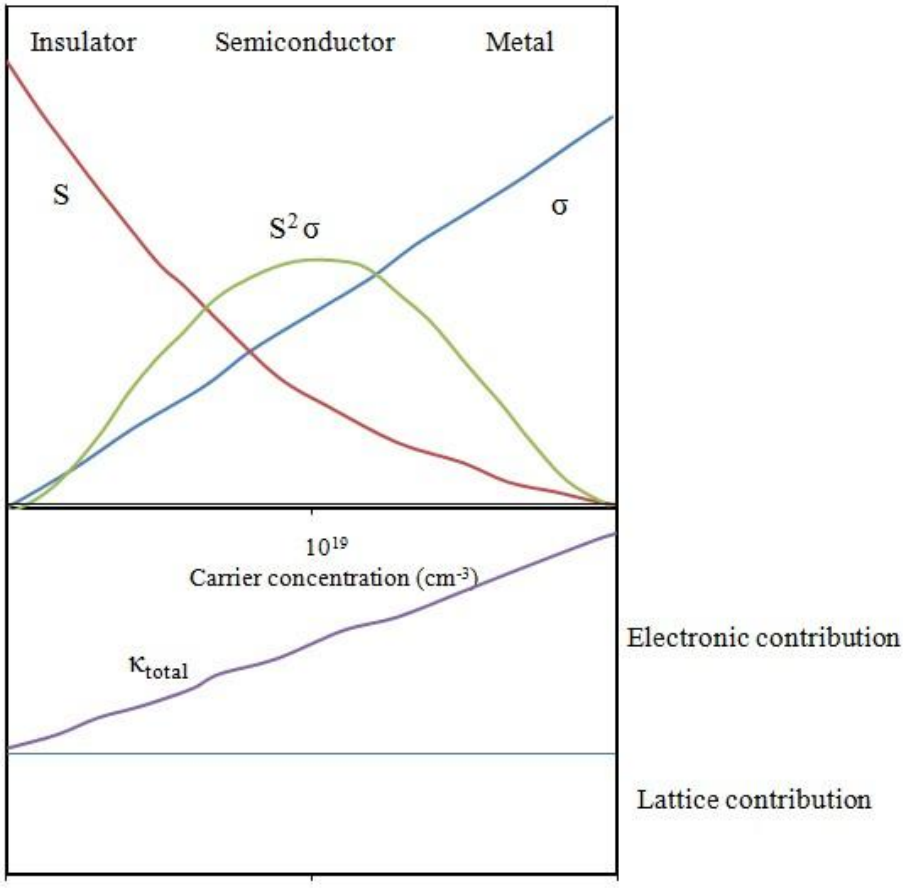

Figure 6 Trade-off between electrical conductivity, Seebeck coefficient, and total thermal conductivity in terms of increasing density of carriers.

Theoretically, the figure of merit ZT can be infinitely large, rendering an efficiency close to the Carnot limit. However, the three parameters, which are all temperature-dependent, are coupled together. Figure 6 shows the relationship between the Seebeck coefficient and electrical conductivity in terms of free carrier concentration, after the so-called Pisarenko relation. Insulators have large Seebeck coefficient but also poor electrical conductivity [reproduced from ref. 3]. With increasing carrier concentration, the materials becomes more conducting but the Seebeck coefficients decrease rapidly. The best thermoelectric materials with high ZT are doped semiconductors. Furthermore, thermal conductivity and electrical conductivity are also related as shown in Figure 6. As is well known, the increase in electrical conductivity also leads to the increase the electronic contribution to total thermal conductivity governed by the Wiedemann-Franz law. Therefore, there is a trade-off between these three parameters for researchers to balance to get the highest possible ZT. The details of electron/thermal transport theory will be discussed in the next section.

1.3 Electronic and thermal transport theory in thermoelectrics

In this section, the electronic transport properties are discussed in terms of conductivity $\sigma = \frac{1}{\rho}$ rather than resistivity. In many solid state physics textbooks, for a simple parabolic band, the electrical conductivity can be expressed as

$$\sigma = \frac{16\sqrt{2}\pi e^2 m^{*\frac{1}{2}}}{3h^3} \int_0^\infty \tau(E)\, E^{\frac{3}{2}} \frac{df(E)}{dE} dE \tag{26}$$

where $m^* = \left(\frac{h}{2\pi}\right)^2 \left(\frac{\partial^2 E}{\partial k^2}\right)^{-1}$ is the effective of mass, h is the Planck constant, $f(E)$ is the Fermi-Dirac distribution function in terms of energy E. For most semiconductors, the charge carriers must be thermally activated to cross the energy gap for conduction to occur, and thus conductivity can be written as

$$\sigma \approx \sigma_0 e^{-\frac{E_g}{2k_B T}} \tag{27}$$

where E_g is the energy gap in semiconductors and k_B is the Bolzmann constant [5]. Also $\sigma = ne\mu$, which means both carrier concentration n and carrier mobility μ are very important parameters for electrical transport. Most of the good TE materials have the electrical conductivity on the order of 10^3 $(\text{Ohm*cm})^{-1}$.

In some semiconductors with disordered structures, a variable-range conducting mechanism will dominate at low temperature. These disordered systems have localized charge-carrier states, and conduction will occur when carriers hop among these states. The conductivity under hopping conditions can be described by [6]

$$\sigma \approx \sigma_0 e^{-\left(\frac{T_0}{T}\right)^{\frac{1}{4}}} \tag{28}$$

where the factor σ_0 is only slightly temperature dependent and the characteristic temperature T_0 is directly related to the density of states at Fermi level $N(E_F)$ and the localization radius a_L

$$T_0 = \frac{C}{k_B N(E_F)\, {a_L}^3} \tag{29}$$

Here c is a constant and usually equals 17.6.

The Seebeck coefficient can be considered as entropy for each charge carrier. It has the general expression

$$S = \pm\left(\frac{(s+2)F_{s+1}(\eta)}{(s+1)F_s(\eta)} - \eta\right) \tag{30}$$

where $F(x)$ is Fermi integral, η is the reduced Fermi energy $\frac{E_F}{k_B T}$ and s is charge carrier scattering parameter, $s = 0, \frac{1}{2}, 2$, for phonon, neutral impurity and ionic impurity scattering respectively, depending on the relaxation time of charge carriers in terms of energy as $\tau = \tau_0 E^{s-\frac{1}{2}}$ for different scattering mechanism [6].

The Mott equation is often used to describe the temperature dependent of the Seebeck coefficient for metals and semiconductors [7]

$$S = \frac{\pi^2 k_B^2 T}{3q}\left(\frac{dln\sigma}{dE}\right)_{E=E_F} = \frac{\pi^2 k_B^2 T}{3q}\left(\frac{1}{n}\frac{dn(E)}{dE} + \frac{1}{\mu}\frac{d\mu(E)}{dE}\right)_{E=E_F} \tag{31}$$

This concept can also be expressed in terms of effective of mass for degenerate semiconductors

$$S = \frac{8\pi^2 k_B^2 T}{3qh^2} m^* \left(\frac{\pi}{3n}\right)^{\frac{2}{3}} \tag{32}$$

with the relation of density of states [8]

$$N(E) = \frac{(m^*)^{\frac{3}{2}}\sqrt{2E}}{(2\pi h)^3 \pi^2} \tag{33}$$

For hopping semiconductors, Parfenov and Shklyyaruk [9] proposed another equation to describe temperature dependence of the Seebeck coefficient

$$S \approx \frac{{k_B}^2}{q}\left(\frac{\pi-2}{\pi}\sqrt{TT_0}+\frac{2\pi}{3}T\right)\left(\frac{dlnN(E)}{dE}\right)_{E=E_F} \tag{34}$$

At characteristic temperature $T_0 > 10^4$ K, the square-root term will prevail while at $T_0 < 10^3$ K , and the Seebeck coefficient will show a linear temperature dependence.

For some materials, there is more than one type of carrier (electrons or holes) from different conducting mechanisms (variable range hopping conducting or traditional band conducting). Assuming there are two types of carrier in one system, the Seebeck coefficient is given by the weighted average of their electrical conductivity values [5]

$$S \approx \frac{S_1\sigma_{1+}S_2\sigma_2}{\sigma_1+\sigma_2} \tag{35}$$

The typical values for good TE materials should be above 150-250 μV/K at the operating temperature.

The total thermal conductivity k has two contributions from electron and phonon transport and therefore can be separated into two parts: the electronic thermal conductivity and the lattice thermal conductivity

$$k = k_e + k_l \tag{36}$$

Governed by the Wiedemann-Franz law, the electronic thermal conductivity can be calculated by$k_e = L\sigma T$. Here L is Lorenz number and for a semiconductor it has a general expression of

$$L = \frac{(1+s)(3+s)F_s(\eta)F_{s+2}(\eta)-(s+2)^2F_{(s+1)}^2(\eta)}{(s+1)^2F_s^2(\eta)}\left(\frac{k_B}{e}\right)^2 \tag{37}$$

where F, η, and s have the same definitions in equation 30. Constant Lorenz numbers L_0 calculated from the Sommerfeld theory are usually used to calculate the electronic thermal conductivity. For metals and highly degenerate semiconductors, $L_0 = 2.45 * 10^{-8}$ W*Ω/K^2 while for intrinsic semiconductors, $L_0 = 1.49 * 10^{-8}$ W*Ω/K^2. For partially degenerate semiconductors, the Lorenz numbers will fall between these two numbers. Even though taking a constant Lorenz number in the metallic limit would not cause huge errors when estimating the lattice thermal conductivity for most of TE materials, in which the lattice thermal conductivity plays a more important role in thermal transport, the Lorenz number must be carefully calculated from equation 37 for materials with low lattice thermal conductivity.

Lattice thermal conductivity involves the transport of phonons, namely the lattice vibrational modes in crystals. It depends on the crystal structure, type of atoms and bond strength among atoms. In modern quantum theory, the vibrational modes can be considered as quasi-particles-phonons, with quantized energy $\hbar\omega$. The general form of the lattice thermal conductivity is described as [10]

$$k_l = \frac{1}{2\pi^2 v}\int_0^{\omega_{max}} \hbar\omega^3 \tau \frac{(\hbar\omega/k_B T^2) e^{\frac{\hbar\omega}{k_B T}}}{\left(e^{\frac{\hbar\omega}{k_B T}} - 1\right)^2} d\omega \tag{38}$$

where v is the average phonon velocity, ω_{max} is the maximum frequency of all phonon modes and τ is the phonon scattering time. The model, proposed by Debye, assumes that the frequency of each phonon mode can be described as $\omega = vq$ by the elastic wave approximation, where q is wave vector in *k*-space. The total number of phonon modes

$$3N = \int_0^{\omega_D} g(\omega) d\,\omega \tag{39}$$

Here the density of modes $g(\omega) = \frac{3\omega^3}{2\pi^2 v^3}$ and thus the Debye frequency $\omega_D = v(6\pi^2 N)^{\frac{1}{3}}$. If we set $\hbar\omega_D = k_B\theta_D$, equation 38 can be rewritten as

$$k_l = \frac{{k_B}^4 T^3}{2\pi^2 \hbar^3 v} \int_0^{\frac{\theta_D}{T}} \tau(x) \frac{x^4 e^x}{(e^x - 1)^2} dx \tag{40}$$

The total phonon scattering time is calculated by taking all the possible phonon scattering mechanism into account by formula

$$\tau^{-1} = \sum_i \tau_i^{-1} \tag{41}$$

For solids that have fewer than about 10^{19} to 10^{20} free carriers per cm^3, which is the case for most of insulators and semiconductors, phonon-phonon scattering mechanism will dominate. In fact, acoustic phonons play main role in heat transfer since they have high velocities. For phonon-phonon scattering, one must consider two scattering processes. At temperatures much lower than the Debye temperature, only long-wavelength phonons exist, and the collisions between two phonons will give rise to a third phonon with momentum (wave vector) still in the first Brillouin zone. This is called a normal scattering process (N-process), in which the momentum of phonons after scattering is conserved. The N-process only changes the momentum distribution of phonons and has no effect on direction of heat current. Therefore, an N-process has no direct contribution to the thermal resistance. When temperature is near or above the Debye temperature, the population of phonons with short-wavelength, in other words possessing wave vectors near the edge of first Brillouin zone, increases and the collisions between those

phonons are likely to result in a third phonon whose wave vector does not fit in the first Brillouin zone. So in this process, which is called an Umklapp process (U-process), the momentum of phonons after scattering is not conserved, causing the changes in the direction of phonon momentum in first Brillouin zone. Therefore, the intrinsic lattice thermal conductivity originates from phonon-phonon U-process scattering. The Umklapp scattering rate is given by [11]

$$\tau_U^{-1}(x) = \frac{{k_B}^2 \gamma^2}{\hbar M v^2 \theta_D} x^2 T^3 e^{-\frac{\theta_D}{3T}} \tag{42}$$

where γ is the Gruneisen parameter which characterizes the anharmonicity of lattice vibrations and M is average mass of atoms.

The scattering rate of phonon-point defect scattering is given by

$$\tau_D^{-1}(x) = \frac{{k_B}^4 \Gamma \mathrm{V}}{4\pi \hbar^4 v^3} x^4 T^4 \tag{43}$$

where Γ is the impurity scattering parameter, which characterizes the disorder in the lattice caused by impurity atoms and is governed by differences in size/mass and bonding forces between host atoms and impurity atoms; V is the average volume per atom.

For scattering by boundaries or interfaces, the common expression for scattering rate is

$$\tau_B^{-1}(x) = \frac{v}{d} \tag{44}$$

where d is the grain size for polycrystal or sample size for single crystal.

There are still other scattering mechanisms, e. g. precipitate scattering, resonant scattering, magnetic scattering, etc., all of which should be taken into account in equation 41 when these scattering mechanisms play important roles in thermal transport. The typical value of thermal conductivity required for good TE materials is below 2 W/m K and $k_l \approx k_e$.

1.4 The strategies to improve the figure of merit

As pointed out by Sofo and Mahan [12], good TE materials should be narrow gap semiconductors with energy gap between 6 k_BT and 10 k_BT (0.26 eV at room temperature). Also, in order to maintain high electrical conductivity, the mobility of carriers should remain high, whereas the lattice thermal conductivity must be minimized.

There are two main methods to improve *ZT* for TE materials depending on the transport theory we discussed in the previous section. One approach is to increase the power factor (*PF*) = S^2/ρ , while a second is to reduce the lattice thermal conductivity.

As is shown in Figure 5 and equation 32, the traditional way to maximize *PF* is to adjust the carrier concentration to the optimum range on the order of 10^{-19}- 10^{-20} cm^{-3}. However, the application of this method is limited by two facts: the maximum in the power factor is given by the nature of materials themselves, and the Seebeck coefficient and electrical conductivity are usually coupled as shown in the Pisarenko relation, which makes it challenging to enhance one property without sacrificing the other.

Some new strategies were proposed to avoid the dilemma mentioned above based on equation 31. Heremans [8] reported the Seebeck coefficient enhancement without increasing electrical resistivity by adding 2% Tl in Na doped PbTe system. It was claimed that the impurity level from Tl introduces resonant states near the Fermi level and thus cause a local increase in density of states over a narrow energy range. Another way to enhance the Seebeck coefficient is to increase the energy dependence of the mobility by the scattering mechanism, which strongly depends on energy of carriers. This was realized in nanostructured PbTe with grain size on the order of electron mean free path (30-50 nm) by high energy ball milling [13]. This method

significantly increases the electron scattering parameter, resulting in an energy filtering effect, in which high energy electrons are scattered more effectively than low energy electrons. Nevertheless, the Seebeck coefficient enhancement through local density of states modification or energy filtering scattering may have the risk of reducing the mobility of charge carriers and thus the electrical conductivity. More recently, Pei and Snyder [14] reviewed the advances in band structure engineering, a more general method to enhance power factor in bulk TE materials. One successful example is the enhancement of power factor in Na-doped PbTe by manipulating the band convergence [15]. The substitution of Te with Se will tune the energy of the high degeneracy hole band and make the convergence of two hole bands occur at higher temperature.

In fact, it is more practical and easy to improve figure of merit by decreasing lattice thermal conductivity, which is largely independent of the electrical properties. A classic approach to decrease lattice thermal conductivity is by creating a bulk solid solution for TE materials, which means mixing two compounds with similar crystal structure. This approach can introduce point defects in the mixture without causing structural change and will strongly enhance the phonon-defect scattering as described in equation 43. As pointed out by Ioffe [16], in most cases, the solid solution method will decrease the lattice thermal conductivity more than the carrier mobility, which makes it plausible for an increase overall figure of merit. For example, $Bi_{2-x}Sb_xTe_3$ and $Si_{1-x}Ge_x$ solid solutions are among the best TE materials for low temperature and high temperature applications, respectively [17].

Slack proposed another approach to reduce lattice thermal conductivity of TE materials with empty cages or voids in crystal structure by adding heavy rattling atoms into voids [18]. In contrast to the solid solution method mentioned above, these alien atoms occupy empty interstitial sites of system rather than substitute atoms in host compound structure. The advantage

of this approach lies in the fact that these rattling atoms will effectively scatter phonons without affecting the transport properties governed by the host compound framework. The best example of application of rattling atoms in TE materials is skutterudites [19,20]. By adding rare earth elements into voids of $CoAs_3$ or $CoSb_3$, the lattice thermal conductivity of these compounds can be reduced by more than one order of magnitude, which makes filled/ partial filled skutterudites among the best of both p and n-type TE materials[21-23] .

Recent progress in nanoscience makes it possible to reduce lattice thermal conductivity by nanostructuring. One way is to directly make TE materials with grain size on the order of several nanometers to scatter acoustic phonons, which have mean free path on this order. This was claimed to be successful in nanostructured Si-Ge alloy synthesized by high energy ball milling [24, 25]. Another successful approach to reduce lattice thermal conductivity is by introducing nanoprecipitates into host compounds. These precipitates can scatter a large portion of the phonon spectrum as was proven in PbTe and PbS system with SrTe, CaS as precipitates [26-29]. The whole spectrum of phonons including phonons with long wavelength can be effectively scattered through a hierarchical structure engineering from atomic scale lattice disorder and nanoscale precipitates to mesoscale grain boundaries. This approach has resulted in minimum lattice thermal conductivity and world-record *ZT* around 2.2 in PbTe/SrTe system [29].

From equation 42, we know Umklapp phonon-phonon scattering is an intrinsic property of crystals, and is governed by the anharmoncity of lattice vibrations. Therefore, it is straightforward to design TE materials with intrinsic low lattice thermal conductivity, where most of thermal resistance is contributed by phonon-phonon scattering without affecting electrical transport properties [30]. This is the main strategy used in the whole study of this

dissertation in order to maintain low thermal conductivity. The details of anharmonicity and intrinsic low thermal conductivity will be discussed in Chapter 3.

1.5 The state of art TE materials

The best TE materials now used in devices have *ZT* value around unity. Figure 7 displays the figure of merit of the most important bulk TE materials [reproduced from ref. 31], which are considered for practical applications. For thermal cooling around room temperature, the TE materials with best performance are among Bi_2Te_3 family [32, 33]. In the mid-temperature range for waste heat recovery, PbTe compounds have the highest figure of merit. For high temperature generators, Si-Ge alloys have advantage over others, because of their high operating temperature and thermal stability [24, 34].

Here we may focus on TE materials in mid-temperature applications since most of the waste heat is in the temperature range of 400K-800K. There are several candidates including lead chalcogenides (PbTe/Se/S) [15, 35], MgSnSi alloys [36, 37], skutterudites [22, 38], and half Heusler compounds (HfZrNiSn and related alloys) [39, 40]. However, they all have some drawbacks, which impede their large-scale application in waste heat recovery. Lead chalcogenides contain toxic elements e.g. Pb, which is forbidden for industry use in some countries. Some of them have expensive or rare elements (Te, Bi, Hf...), which will largely increase the cost of TE devices. The MgSnSi alloy is sensitive to moisture and also has a phase stability problem at operating temperature. Skutterudites and half Heusler have good mechanical properties and stability but they do not have p-type materials with comparable *ZT* values to n-type materials. In all, most TE materials with high figure of merit synthesized in research labs

require raw materials in the form of high purity elements and careful doping, which again will largely increase the expense of making real TE devices.

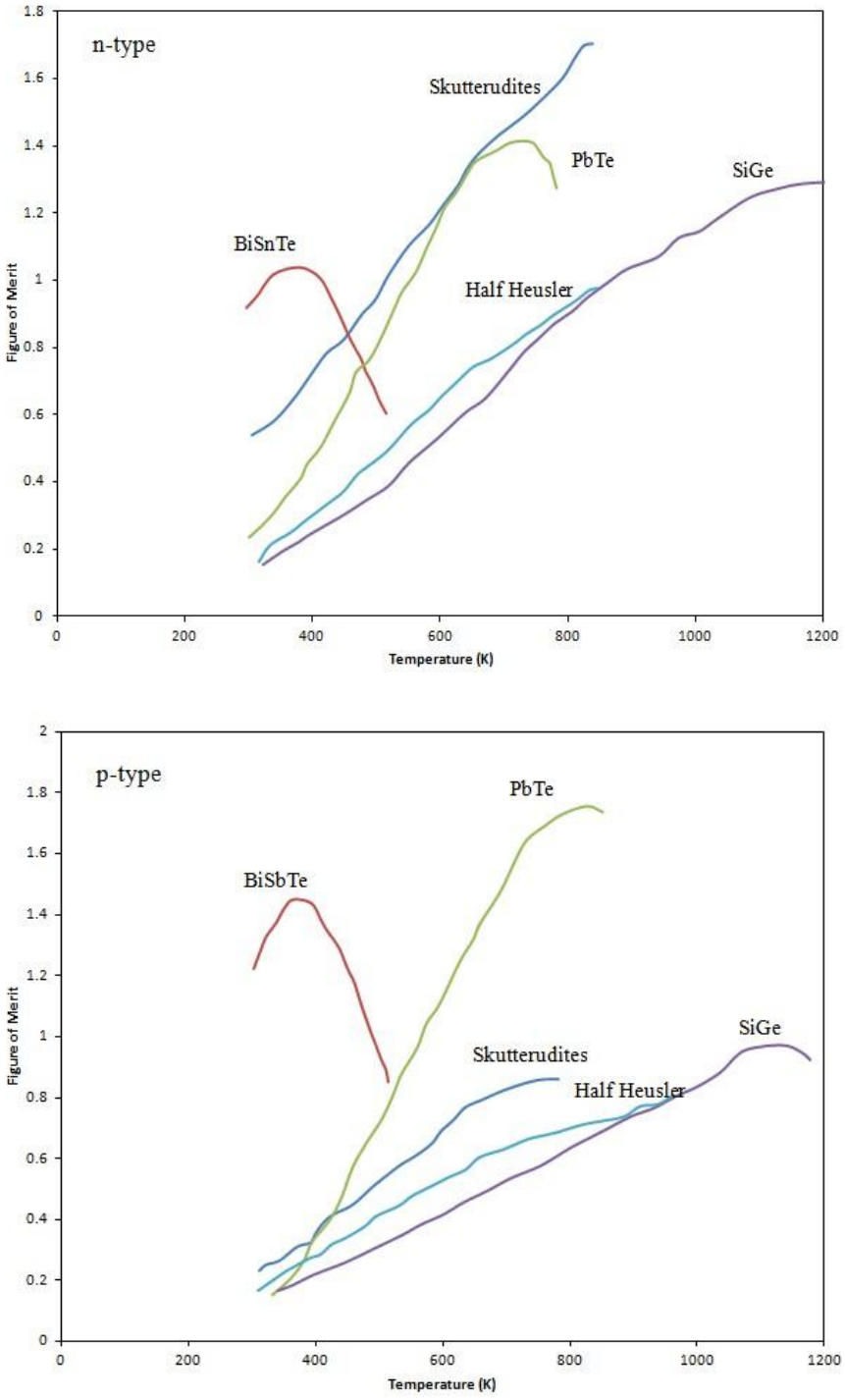

Figure 7 Figure of merit of state of art n-type and p-type TE materials.

Here in this work, we seek new TE materials, especially p-type, with *ZT* value comparable to or higher than that of commercial TE materials present in use but without toxic or expensive elements. More importantly, we will show how to avoid complicated processing commonly required in semiconductor industry and directly use untreated natural minerals as a raw source, which will reduce the cost of TE devices to an acceptable level for large-scale applications.

Chapter 2 Synthesis and Characterization Techniques

The synthesis and subsequent consolidation process used in this study are the same for all the samples except for those synthesized using high energy ball milling, as mentioned in Chapter 6. All of the phase, microstructure and composition analysis, and thermoelectric properties measurement employed in this study are also the same for all the samples.

2.1 Materials synthesis

The synthesis of all samples started from weighing stoichiometric ratios of high pure elements (>99.99%, Alfa Aesar Puratronic) by using a high-precision digital scale. The pure elements were then put into quartz ampoules for evacuation on the home-made sealing station shown in Figure 8. When the vacuum reached $<10^{-5}$ Torr, the ampoules were sealed by a methane-oxygen torch. The sealed ampoules were hung in a digital vertical furnace for a direct melting/fusion reaction. For the compounds containing S and Se in this study, the initial heating rate is very important, since both elements have low melting point and high vapor pressure. If the heating rate is large at the initial stage (below 300 ℃), the evaporated S and Se will adhere to the ampoule wall and cause the composition of the synthesized sample to deviate from the target stoichiometric ratio. Therefore all of the materials studied here were heated at the speed of 0.3 ℃/min to 750 ℃ ,soaked at this temperature for 12 hours and then slowly cooled at the rate of 0.5 ℃/min.

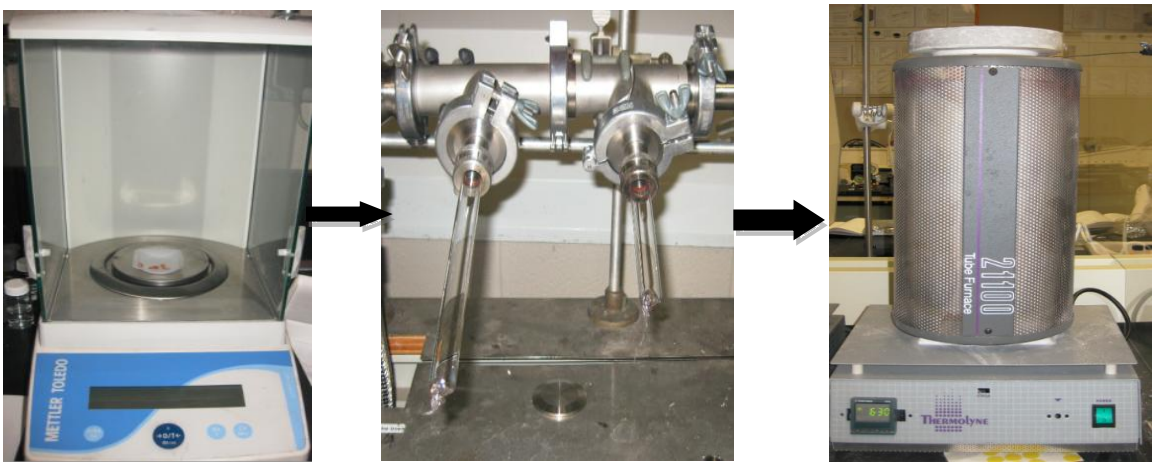

Figure 8 Materials synthesis processes : weighing stoichiometric quantities of elements with high purity (left), evacuating ampoules (middle), hanging ampoules in vertical furnace (right).

Subsequently, the compound ingots were taken out and loaded into a stainless ball milling jar for ball milling of 3 minutes in a SPEX SamplePrep Mix/Mill 8000M machine. The powders were then cold pressed into pellets and encapsulated in a new ampoule for evacuation and sealing. The sealed ampoules were put in a box furnace for annealing for one week at 450 ℃ for homogenization. To prove the validation of the synthesis process described above, the phase purity was checked by X-ray diffraction pattern analysis as mentioned in section 2.3. Figure 9 displays different XRD patterns from powders with different synthesis processes. Additionally , a water quench process was also attempted in a trial experiment and it gave rise to multiple phases. A further annealing of the quenched samples up to 2 weeks had no effect on the elimination of these multiple phases and thus we concluded that water quenching is not suitable for synthesizing tetrahedrite, while a slow cooling process is required to obtain tetrahedrite with high purity.

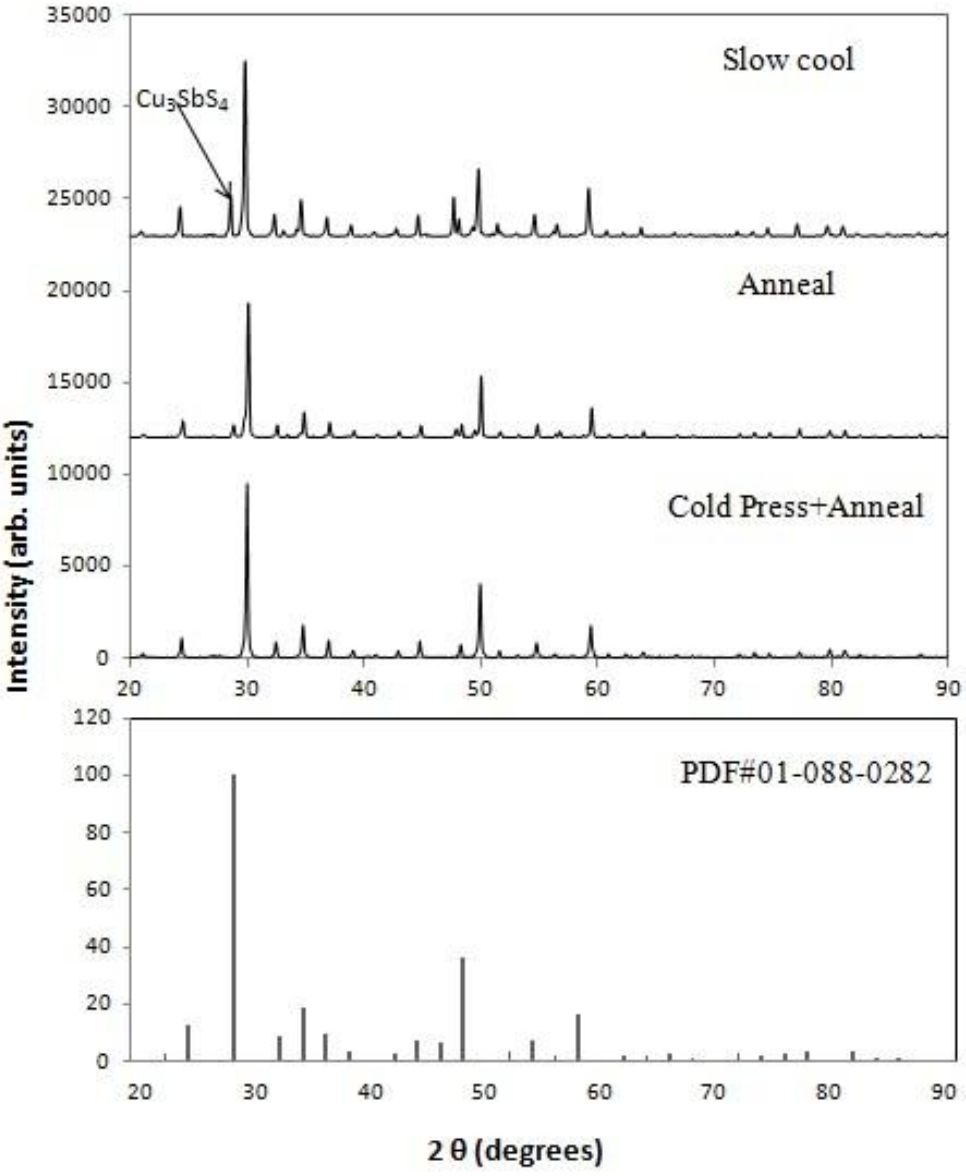

Figure 9 X-ray diffraction patterns for $Cu_{12}Sb_4S_{13}$ under different synthesis process.

2.2 Sample preparation

After checking the phase purity of annealed pellets, the specimens were ball-milled for another 30 min with the ball-milling jar back-filled with argon in order to avoid oxidization. The fine powders obtained after this procedure were loaded under argon into a graphite die with a diameter of 10 mm and hot-pressed for 30 min at 450 ℃ and 70 MPa. All the hot-pressed pellets are over 98 % of theoretical density.

The final products were cut by a diamond saw into two sample geometries: bars of dimensions 3 *3 *8 mm^3 for electronic transport property measurement (electrical resistivity and Seebeck coefficient), and disks of dimensions 10 mm diameter by 1.5 mm thickness for thermal conductivity tests, respectively.

2.3 Phase, microstructure and composition analysis

Before doing any physical property measurement, the phase purity and the crystal structure of these phases should be determined first. The phase purity of samples was checked by performing X-ray diffraction analysis on a Rigaku Miniflex II bench-top X-ray diffractometer (Cu Kα radiation, λ=0.154 nm) on powders obtained from small pieces of the pellets. The diffraction patterns were analyzed using a Jade software package with JCPDS XRD pattern database.

As mentioned in the previous chapter, grain boundary scattering is one crucial mechanism for phonon scattering and it depends on the grain size. The micromorphology of hot-pressed samples including grain size and porosity was investigated by using a JEOL 7500F scanning electron microscope (SEM) on the fractured surfaces of samples. An Oxford energy dispersive x-

ray spectroscopy (EDS) attached with the same SEM was used to check the elements distribution, i.e., homogeneity, on the polished surfaces of samples.

2.4 Low temperature transport property measurement

Low temperature (80K-300K) electrical and thermal transport measurements were performed on a homemade continuous liquid nitrogen flow cryostat using a standard steady state technique under high vacuum. A bar-shaped sample with an 800 Ω resistor attached on its free end was glued on a copper base with a conducting silver epoxy. Figure 9 shows the illustration of sample set up for low temperature measurement. Along the length of the bar sample, two copper-constantan thermocouples were soldered on two copper strips, which are anchored on the sample surface also by silver epoxy. These two thermocouples can not only read the temperature difference between positions of two strips, but, using the copper legs of each thermocouple, also measure the voltage difference if there is any. Before taking any measurement, the environmental temperature of the cryostat is kept at desired temperature for 1200 seconds for stabilization. After that, a constant current is applied through sample and the voltage difference along the length of the sample will be measured. The resistivity is then calculated by using Ohm's law. Since the temperature gradient on the sample may cause additional Seebeck voltage, which would result in error during the measurement, a polarized DC current was used in our measurement. By subtracting the measured voltage difference with current in negative direction from the measured voltage difference with current in positive direction, the influence of Seebeck voltage can be eliminated in resistivity measurement.

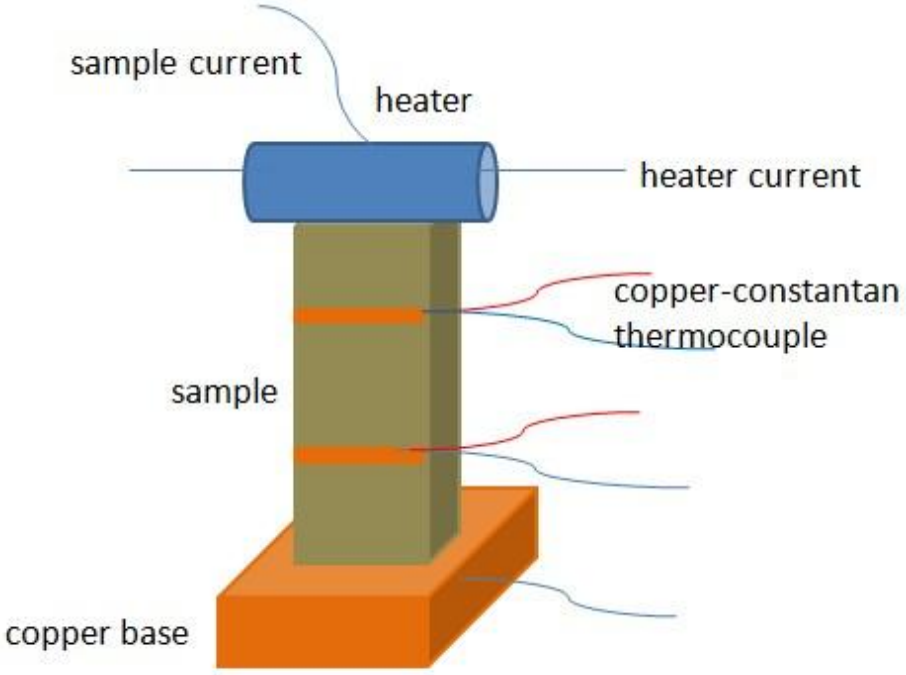

Figure 10 Schematic representation of experimental setup for low temperature thermoelectric properties measurement.

After the resistivity was measured, the current through sample was turned off and a current through the heater on top of sample is applied, which will generate a heat flow and a temperature gradient along the sample. By adjusting the current magnitude, the temperature difference between two thermocouples can be set to close to 1 K- an optimum value for measurement. After 1800 seconds, it was assumed that the temperature gradient distribution is stabilized, and the two thermocouples will read the temperature difference (ΔT) and voltage difference ($V_{Seebeck}$). Then the Seebeck coefficient is calculated by its definition in equation 1 and the thermal conductivity is given by

$$k = K * \frac{l}{A} = \frac{Pl}{\Delta T * A} = \frac{VIl}{\Delta T * A} \tag{45}$$

where V is the voltage across the heater and I is the current applied through the heater, l is the distance between the two copper strips and A is the cross section area of samples.

In equation 45, it is assumed that all the heat generated by the heater passes through the sample. In fact, the part of the heat is lost by radiation, which leads to an overestimation of thermal conductivity. When the thermal conductivity measurement is taken near room temperature, the error caused by radiation loss cannot be ignored, especially for TE materials having low thermal conductivity. For most of the samples in this study, the radiation loss accounts for 30%-50% in overestimation of actual thermal conductivity at room temperature. Here we used an approximation method to correct radiation loss error. The measured thermal conductance can be divided into two parts

$$K_{measure} = K_{actual} + K_{loss} \tag{46}$$

K_{loss} is the thermal conductance caused by radiation and calculated as

$$K_{loss} = \frac{dP_{loss}}{dT} \tag{47}$$

According to Stefan–Boltzmann law, the radiant power from an object (P_{loss}) is related to its total area (A_{total}), emissivity ε and temperature T

$$P_{loss} = A_{total}\varepsilon\sigma T^4 \tag{48}$$

where σ is Stefan constant. So the thermal conductance from radiation is

$$K_{loss} = 4A_{total}\varepsilon\sigma T^3 \tag{49}$$

For given samples with similar compositions and dimensions, it is assumed that $4A_{total}\varepsilon\sigma$ is a constant and K_{loss} is a constant at fixed temperatures for all samples. K_{loss} at 300 K is measured by taking samples off the copper base so there is no convection thermal conductance. K_{loss} at any temperature is calculated as

$$K_{loss} = K_{loss\ 330K}\left(\frac{T}{300}\right)^3 \tag{50}$$

By subtracting K_{loss} from $K_{measure}$, the corrected thermal conductivity is obtained. Another way to minimize the influence of radiation loss is making samples with large cross section areas and small length for thermal conductivity measurement. In this case, $K_{actual} \gg K_{loss}$ and K_{loss} can be ignored. For low temperature measurement, the error in electrical transport measurement is estimated to be 5%. While the error in thermal conductivity measurement is rather hard to estimate due to heat loss described above.

2.5 High temperature transport measurement

High temperature (300K-723K) electrical transport measurements were performed on a commercial ULVAC ZEM-3 system under helium atmosphere. The basic principle for the high temperature measurement is similar to that of low temperature electrical transport measurement. The high temperature thermal conductivity is calculated by

$$k = D\rho C_P \quad (51)$$

where D is thermal diffusivity, ρ is sample density and C_P is the heat capacity at constant pressure. The thermal diffusivity was measured using the laser flash method (Netzsch, LFA 457) with all samples coated with carbon. Differential scanning calorimetry (Netzsch, DSC200F3) was used to measure the heat capacity (C_P). All the heat capacity data were close to or higher than the Dulong–Petit value. The densities of the samples were measured using the Archimedes method with ethanol as the suspending fluid. All the samples used for thermal properties measurements were cut from the same pellets as those used for transport properties. We estimate that the uncertainties in our electrical and thermal transport measurement are 5% and 10%, respectively for high temperature measurement.

2.6 Theoretical calculation, mechanical properties and other measurement

It should be noted that this thesis includes collaboration work/data from outside of our group. The Ozolins group from UCLA performed Density-Functional Theory (DFT) calculations based on the highly efficient Vienna Ab Initio Simulation Package (VASP) [41-43]. Self-consistent spin-polarized calculations were performed using the Perdew-Becke-Ernzerhof (PBE) generalized gradient approximation (GGA) for the exchange-correlation (xc) functional [44, 45] and plane wave basis with the cutoff energy of 450 eV. Calculations were performed using the primitive cell of $Cu_{12}Sb_4S_{13}$ and electronic Bloch functions were calculated on regular Monkhorst-pack **k** point meshes of 10×10×10. Phonon dispersion curves were calculated using an in-house DFT linear response code. Phonon modes were calculated by taking finite differences between phonon frequencies with two lattice parameters separated by 2%.

Mechanical properties including Young's modulus (E) shear modulus (G) and bulk modulus (B) were measured via a non-destructive technology, namely, the resonant ultrasound spectroscopy [46] (RUS), RUSpec, Quasar International, Albuquerque, NM, USA) by Professor Eldon Case's group in MSU. Specimens were excited with mechanical vibration through a frequency range of 20–600 kHz, and the resonance modes of the specimens were detected and recorded. The elasticity can be calculated from the resonance frequencies along with the mass, shape, and the dimensions of the specimens using a commercial software package (RPModel, Quasar International, Albuquerque, NM, USA). Additional details of RUS measurement technique can be found in elsewhere [47, 48]. Low temperature specific heat, thermal expansion coefficient and phonon density of states measurement were finished in Oak Ridge National Lab.

Chapter 3 Mineral Thermoelectrics and Tetrahedrites

3.1 History of mineral thermoelectrics

When Thomas Seebeck first discovered the Seebeck effect, he conducted experiments on 25 metals and 30 minerals [49]. In his study, all the metals had low Seebeck coefficient while some of minerals such as PbS, Bi_2S_3,$CoAs_2$ hade fairly large Seebeck coefficient. However, the Seebeck effect was not considered for practical use at that time so the electrical resistivity was not taken into account. In 1950, Telkes did systematic research on thermoelectric power and electrical resistivity of more than 100 natural minerals [50]. Measurements were usually performed on several samples from different sources of the same mineral. Although the presence of heterogeneous or non-stoichiometric impurities, cracks inside specimens or irregular shapes of specimens can cause large variations in the resistivity or thermopower of different specimens for the same mineral, the results may help us understand the correlation between these two properties and establish order of magnitude correlations on the same minerals. In this study, some of these minerals show low electrical resistivity and high thermopower, which indicates the potential for thermoelectric application. Tetrahedrite was investigated and one specimen was found to have properties suggesting good TE behavior.

3.2 Introduction to tetrahedrites

Tetrahedrite is a common copper antimony sulfosalt mineral with formula of Cu_{10}(Ag, Zn, Fe)$_2Sb_4S_{13}$. It is an important ore of copper and sometimes of silver and forms gray to black metallic crystals or masses in veins [51] (Figure 11). Pure endmembers of the series are seldom

if ever seen in nature. Tetrahedrite forms a solid solution series with the similar mineral tennantite ($Cu_{12}As_4S_{13}$), in which arsenic replaces antimony in the crystal structure. They are widely spread around the world [52-54]. For example, large quantities are found in Europe, Japan, Peru, and Chile, and both minerals occur in large amounts in Colorado and Idaho in the United States as well.

Figure 11 Picture of tetrahedrite crystal (with quartz) from Peru.

Composition variation and crystal structure of tetrahedrite have been studied in the past twenty years [55-58]. It possesses a cubic structure of $I\bar{4}3m$ symmetry with six of the twelve Cu atoms occupying trigonal planar 12*e* sites and the remaining Cu atoms distributed on tetrahedral 12*d* sites (Figure 12). The Sb atoms also occupy a tetrahedral site but are bonded to only three sulfur atoms, leading to a void in the structure and a lone pair of electrons surrounding each Sb atom. In terms of a simple crystal-chemical formula, four of the six tetrahedral sites are thought

to be occupied by monovalent Cu, while the other two are occupied by Cu^{2+} ions; the trigonal planar sites are occupied solely by monovalent Cu.

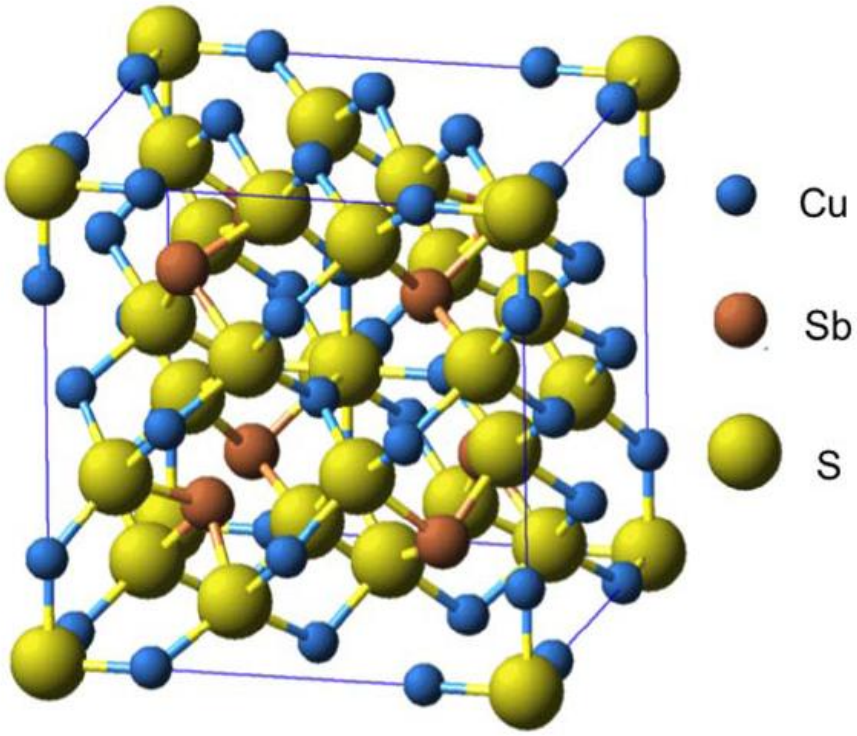

Figure 12 Crystal structure of tetrahedrite.

3.3 Intrinsic low thermal conductivity and anharmonicity in tetrahedrite

As described in chapter 2, the main approach to develop good TE materials is to identify semiconductors that have good electronic transport property and at same time very low thermal conductivity. Slack proposed the concept of a "phonon-glass electron-crystal" (PGEC) semiconductors, which possess electronic properties like good semiconductor single crystal and low thermal conductivity like amorphous materials [18]. The key task to realize PGEC concept

is to find a semiconductor with intrinsically low lattice thermal conductivity, which is close to theoretical minimum [59, 60]. The origin of intrinsically low thermal conductivity can be attributed to strong anharmonicity and resultant strong phonon-phonon interactions. The strategy of designing TE materials with intrinsically low thermal conductivity is attractive to researchers since the anharmonic phonon-phonon interaction is intrinsic for solids and independent of grain size, impurity levels and other properties related to the microstructure. Morelli and Heremans identified intrinsically minimal thermal conductivity in cubic I-V-VI_2 semiconductors $AgSbTe_2$ and $AgBiSe_2$ [61]. In their study, they ascribed the low thermal conductivity to the non-bonding lone pair electrons in the outer shell of Sb, which result in anharmonicity when the wave functions of these non-bonding electrons overlap during thermal vibrations atoms as approach each other. Furthermore, Skoug and Morelli found the role of lone pair electrons in nitrogen-group chalcogenide compounds ($CuSbSe_2$ and $Cu3SbSe_3$) with minimum thermal conductivity [62, 63]. They showed that in these compounds lone-pair electrons from the group V atom (Sb) will give rise to minimum lattice thermal conductivity due to anharmonicity caused by electrostatic repulsion between the lone-pair electrons and neighboring chalcogen ions (Se), which are confirmed by both previous study and theoretical calculation [64, 65]. The strength of anharmonicity depends on the bond length and angle between the group V atom and the chalcogen atom and the coordination number of the group V atom. Most recently, a combined work with both theoretical calculation and experimental data performed by Nielsen *et al*. [66] found a similar phenomenon in I-V-VI_2 compounds based on the rocksalt structure. Marginally stable I-V-VI_2 compounds with the lone-pair electrons from group V atoms have anharmonic bonds that result in strong phonon-phonon interactions, which cause their thermal conductivity to reach to the amorphous limit, in spite of the fact that these are crystalline materials.

In order to investigate the origin of intrinsically low thermal conductivity found in tetrahedrite structure, $Cu_{10}Zn_2Sb_4S_{13}$ was synthesized and consolidated following the procedures described in Chapter 2. Since $Cu_{10}Zn_2Sb_4S_{13}$ is almost insulating and the atomic mass difference between Cu and Zn is small, we can assume that the lattice thermal conductivity is the dominant heat conduction channel in this case and the thermal conductivity of $Cu_{10}Zn_2Sb_4S_{13}$ is then representative of the lattice thermal conductivity of the tetrahedrite family. Furthermore, in order to minimize the effect of radiation loss, the sample used for low temperature thermal conductivity measurement is chosen to have a large cross sectional area/length ratio (a circular disk with 10 mm diameter and 1.5 mm length). The synthetic sample with the same composition was sent to our collaborator in Oak Ridge National Lab for low temperature specific heat, thermal expansion coefficient and inelastic neutron scattering measurement.

In solid state physics theory, a simple description of anharmonicity is the anharmonic terms in the expansion of the ionic interaction potential energy in solids. The lattice thermal conductivity of a solid is limited only if there are anharmonic terms whereas a perfect harmonic crystal would have an infinite thermal conductivity if the boundary scattering is not taken into account. The direct measure of anharmonic strength in solid is Grüneisen parameter, which is defined as the negative of the logarithmic derivative of each phonon mode's frequency ω_i with respect to the crystal value V [67]:

$$\gamma_i = -\frac{\partial \ln(\omega_i)}{\partial \ln V} \tag{52}$$

The definition of Grüneisen parameter reflects how much the chemical bond stiffness in solids is affected by changes in the distances between atoms. In the experiment, the average Grüneisen parameter in solids can be determined by [68]

$$\gamma = \frac{9\alpha B V_m}{C_V} \tag{53}$$

where α is the linear thermal expansion coefficient, B is the bulk modulus, V_m is the molar volume and C_V is the specific heat. For $Cu_{10}Zn_2Sb_4S_{13}$, α is $10.35*10^{-6}$ K^{-1}, B is 44.05 GPa [69] and C_V is 4.06 $Jg^{-1}K^{-1}$ at 300 K, so the calculated Gruneisen parameter ≈ 2.06 at 300 K, which is a typical large value for solids with strong anharmonicity (for $AgSbTe_2$ γ = 2.05 and for $AgBiSe_2$ γ = 2.9).

Here we are interested in the system where anharmonic Umklapp process dominates in phonon-phonon interactions. Therefore, it is assumed that only the acoustic phonon modes participate in the heat conduction process and the intrinsic thermal conductivity expression derived by Slack is [70, 71] :

$$\kappa_L = A\frac{\bar{M}\theta^3\delta}{\gamma^2 n^{2/3} T} \tag{54}$$

Here $\bar{M}$ is the average mass of the atoms in the compound, n is the number of atoms in the primitive unit cell, δ^3 is the volume per atom, θ is the Debye temperature and γ is Grüneisen parameter. For thermal conductivity in the unit of $Wm^{-1}K^{-1}$, $\bar{M}$ is in amu, δ is in Angstroms and A is a physical constant ≈ $3.04*10^{-6}$. For $Cu_{10}Zn_2Sb_4S_{13}$, $\overline{M}$ = 57.46, δ = 3.36 Å, θ = 239 K and γ = 2.06 as calculated above. This yields a room temperature thermal conductivity of 0.54 W/m* K, in quite good agreement with the experimental value of 0.51 W/m* K .

Equation 54 only applies for the condition that the temperature is close to or above Debye temperature, since as we discussed in Chapter 1 about phonon-phonon scattering mechanism only under this condition the high probability of phonon collisions and the large amount of

momentum loss will give rise to intrinsic lattice thermal conductivity governed by anharmonicity. In fact, the lattice thermal conductivity has an amorphous limit value given by [72]

$$\kappa_{min} = \left(\frac{\pi}{6}\right)^{\frac{1}{3}} k_B n^{\frac{2}{3}} \sum_i \left[v_i \left(\frac{T}{\theta_i}\right)^2 \int_0^{\frac{\theta_i}{T}} \frac{x^3 e^x dx}{(e^x - 1)^2} \right] \tag{55}$$

where v_i is the sound velocity of mode i, θ_i is the acoustic mode-dependent Debye temperature. The increased value of Grüneisen parameter , namely the strength of anharmonicity will cause the lattice thermal conductivity to approach theoretical minimum value.

A much simpler model for minimum thermal conductivity is often used by assuming the phonons have a mean free path λ on the order of interatomic spacing. In this case, the minimum thermal conductivity is predicted as [61]

$$\kappa_{min} = \frac{1}{3} C_V v \lambda \tag{56}$$

where C_V is the specific heat, v is the sound velocity and λ is the phonon mean free path. For this estimate we use specific heat C_v obtained from our experimental data and a mean sound velocity $v = 2500$ m/s [69] as measured by the resonant ultrasound spectroscopy. For the phonon mean free path we use the interatomic distance l = 0.226 nm [55].

For $Cu_{10}Zn_2Sb_4S_{13}$ disk sample measurement, the heater was attached on top of a circular copper foil which has the same area as that of the disk sample. Then the disk sample was sandwiched between copper foil and copper base by epoxy glue (shown in Figure 13).

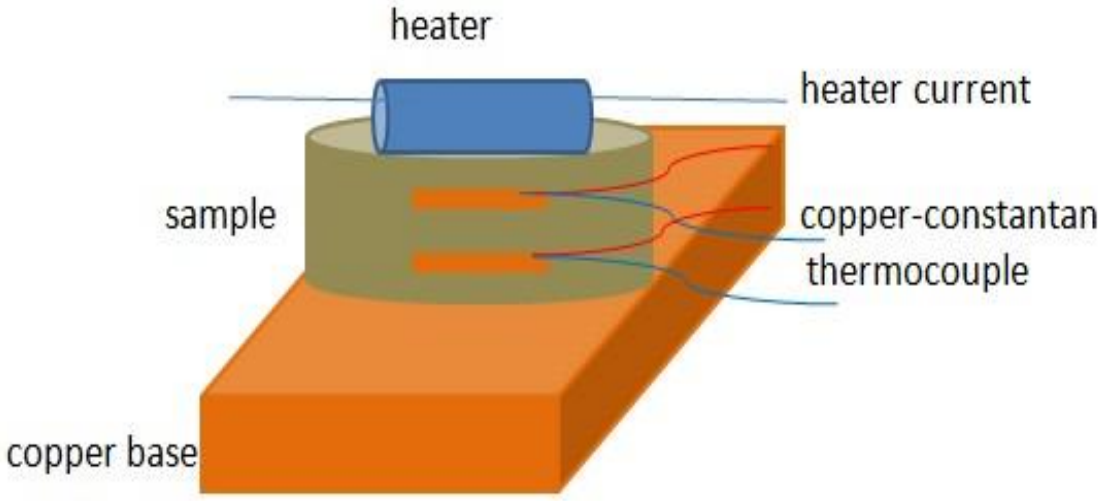

Figure 13 Schematic illustration of sample setup for low temperature thermal conductivity measurement of disk sample.

Two different thermocouple setups were tried in this measurement : 1) setting one thermocouple on top of the copper foil and the other on the side wall of disk sample; 2) setting both thermal couples on the side wall of the disk sample. The results of thermal conductivity are shown in Figure 14. To validate the disk sample thermal conductivity measurement, the high temperature data from room temperature to 723K measured by laser flash method, the comparison data from a bar sample (3 mm*3 mm*8 mm dimensions) measurement and the calculated minimum thermal conductivity based on the constant mean free path assumption were all included.

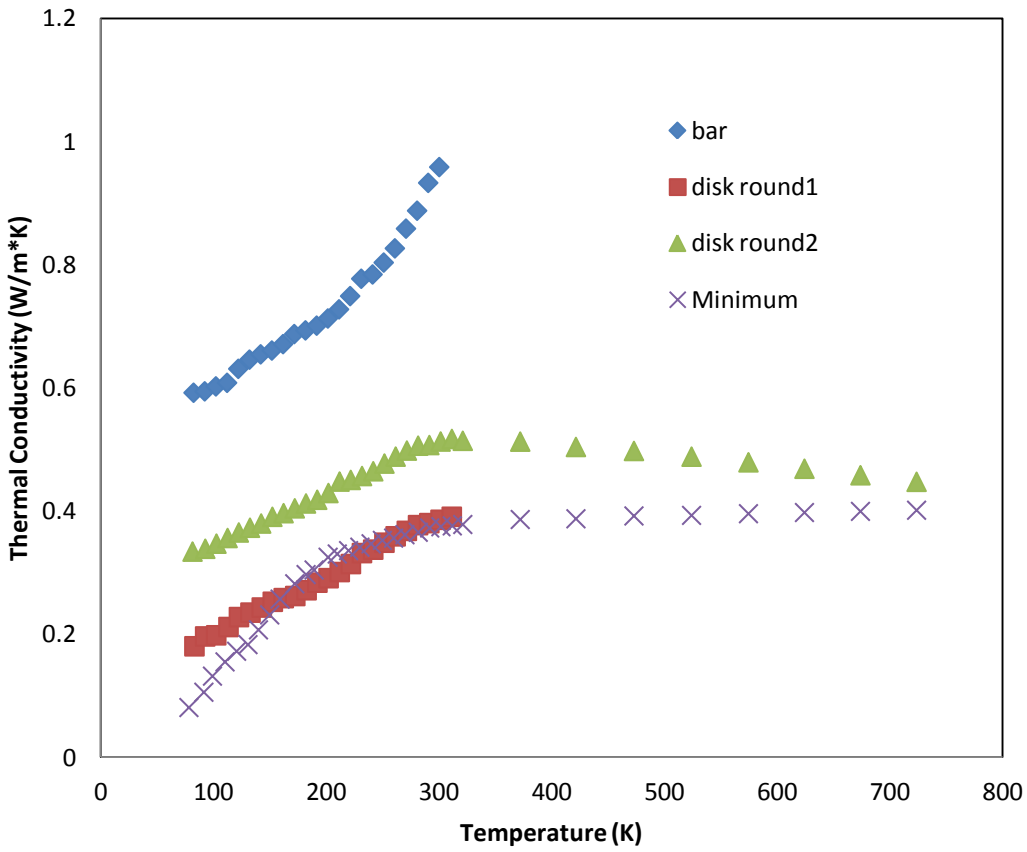

Figure 14 Thermal conductivity of $Cu_{10}Zn_2Sb_4S_{13}$ on the sample but different methods. Bar : data from bar sample measurement. Disk round 1: data from method of setting one of thermal couple on the top of foil. Disk round 2: data from method of setting both thermal couples on side of disk sample. Minimum : calculated minimum thermal conductivity.

From the data above, it is clear that the bar sample measurement doubles the value of thermal conductivity, compared to the data from laser flash method at room temperature, although the radiation loss error has already been taken into account in post data analysis. On the other hand, the method of setting one of thermocouple on top of copper foil underestimates the thermal conductivity, since a large thermal resistance between copper foil and sample was introduced into the measurement by this method. The data obtained from measurement with both thermocouples on the side wall of disk sample agrees well the data from high temperature

measurement. From 80 K to room temperature, the thermal conductivity of $Cu_{10}Zn_2Sb_4S_{13}$ increases with increasing temperature, which violates the Slack 1/T law shown in equation 54, since the strong phonon scattering reduces the phonon mean free path to close to interatomic spacing. In this case, the thermal conductivity is dominated by the increasing specific heat as stated in equation 56. Near room temperature, which is above the Debye temperature of tetrahedrite, the value of specific heat begins to saturate, approaching the Dulong-Petit high temperature limit, and the thermal conductivity curve becomes flat or slightly decreases. At higher temperatures, the phonon mean free path is further reduced to interatomic spacing limit, reducing the thermal conductivity closer to the theoretical minimum.

In order to determine the origin of strong anharomonicty and the resultant intrinsic low thermal conductivity, our collaborators at Oak Ridge National Laboratory performed low temperature specific heat, inelastic neutron scattering measurements and theoretical calculations to identify the phonon mode distribution and specific lattice vibrations for tetrahedrites [73].

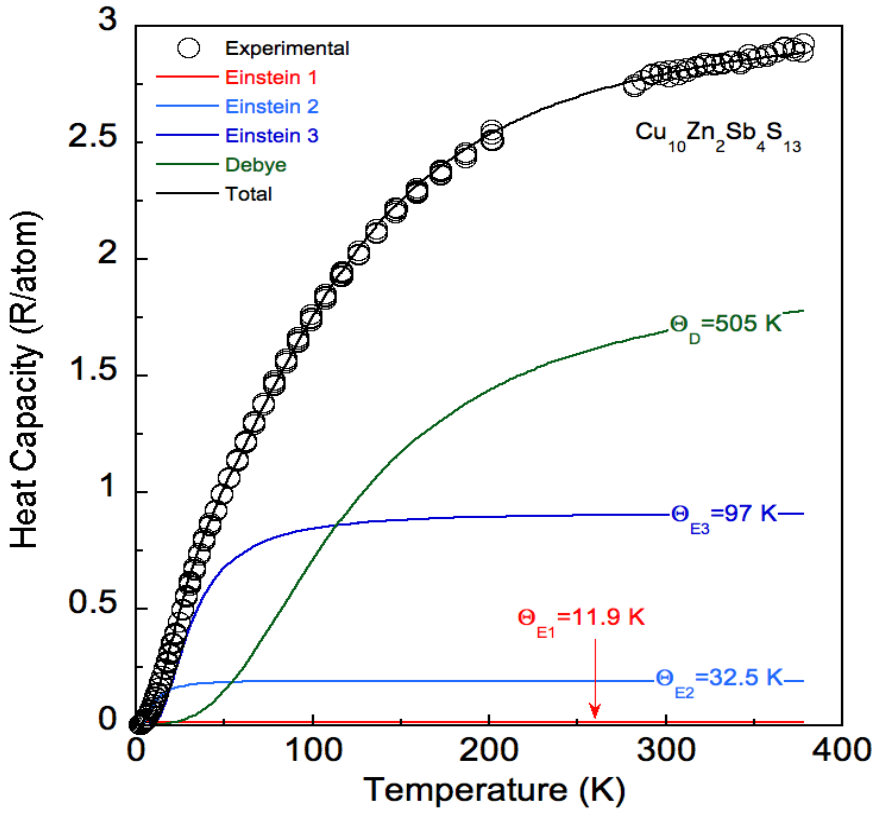

Figure 15 Specific heat data of synthetic sample of composition $Cu_{10}Zn_2Sb_4S_{13}$ and fitting curve. The contributions from the Debye lattice and the three Einstein oscillators are included and the corresponding temperatures indicated.

Figure 15 shows the temperature dependence of specific heat of $Cu_{10}Zn_2Sb_4S_{13}$ from 2 K to 380 K. It was found that by using a Debye lattice and three Einstein oscillators, associated with three localized modes from trigonally coordinated Cu atoms, the experimental specific heat data can be well reproduced as follows :

$$C(T) = 9\,a_D R\left(\frac{T}{\theta_D}\right)^3 \int_T^{\frac{\theta_D}{T}} \frac{e^x x^4}{(e^x-1)^2}dx + 3R\sum_{i=1}^{3} a_{Ei}\,\frac{e^{\frac{\theta_{E_i}}{T}}\left(\frac{\theta_{E_i}}{T}\right)^2}{\left(e^{\frac{\theta_{E_i}}{T}}-1\right)^2} \qquad (57)$$

where $a_D = \frac{23}{29}$ and $a_{Ei} = \frac{2}{29}$, θ_D and θ_{E_i} are characteristic temperatures for Debye mode and Einstein oscillators, used as fitting parameters. The characteristic temperatures of three Einstein oscillators were found to be θ_{E_1} = 11.9 K, θ_{E_2} = 32.5 K and θ_{E_3} = 97 K. The idealized phonons density states based on the fitting is shown in Figure 16.

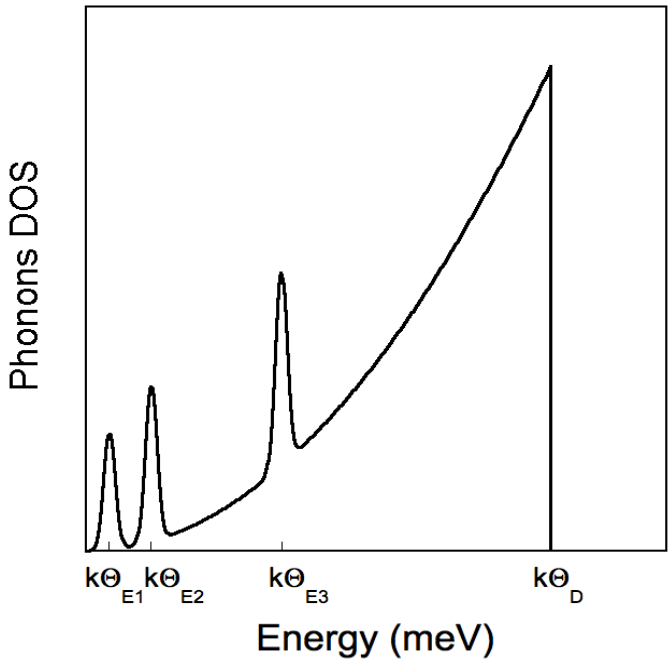

Figure 16 Idealized phonons density of states of $Cu_{10}Zn_2Sb_4S_{13}$.

As shown above, the energy values associated with the characteristic temperatures of these oscillators are 1.0 meV, 2.8 meV and 8.4 meV, respectively. The high energy Einstein oscillator is believed to be from the vibration of the trigonally coordinated Cu atoms normal to the plane of the sulfur triangle. The large amplitude vibration of this oscillator is a clear sign of strong anharmonicity resulting from the unstable overlap of Cu *d*-orbitals with S *p*-orbitals, which was proved by the predicted double-well potential with energy minima while Cu atoms buckling

above and below the Cu-S trigonal plane through theoretical calculation. Furthermore, the motion of Cu atoms leads to strong repulsions with neighboring Sb atoms with lone-pair electrons in the direction perpendicular to this plane. Two low energy Einstein oscillators result from the motion of trigonlly coordinated Cu atoms perpendicular to the trigonal plane. In previous study, this less important but strongly anharmonic displacement was considered to be due to the fact that the distances among three S atoms are not equal and Cu atoms prefer to be towards the longer edge of the S triangle.

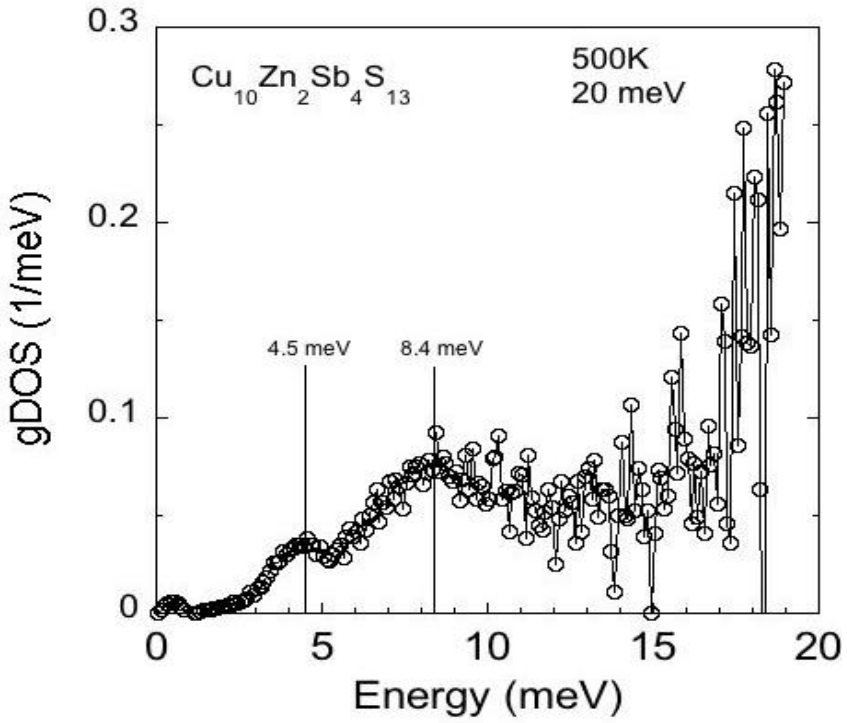

Figure 17 Measured phonon density of states of $Cu_{10}Zn_2Sb_4S_{13}$ by inelastic neutron scattering.

The measured phonon density of states of $Cu_{10}Zn_2Sb_4S_{13}$ through inelastic neutron scattering is displayed in Figure 17. The high energy Einstein oscillation peak was found at the

exact energy of 8.4 meV as extrapolated from specific heat, which proves that the strong anharmonicity in phonon-phonon interactions results from the motion of Cu atoms above and below S triangle planes. However, the other two low energy Einstein modes cannot be identified in experimental phonon density of states spectrum, since the assumption of a delta-function Einstein mode is usually unrealistic. Compared to the idealized phonon spectrum, in reality, the amplitude of phonon density from the Einstein oscillators corresponding to the trigonally coordinated Cu atoms would be smaller and their spectra may have some overlap with the Debye mode spectrum in low energy, which makes it hard to find these low energy Einstein mode peaks. Nevertheless, it is still a great success to identify the strongest anharmonicity mode in experimental phonon density of states spectrum .

Lattice dynamics calculations were performed to demonstrate the lattice vibrational spectrum of the tetrahedrite structure. Figure 18 shows the calculated phonon dispersion curve in *k*-space. Unstable vibrational modes with imaginary frequencies were found and believed to be associated with the trigonally coordinated Cu atoms. Furthermore, transverse acoustic (TA) branches also become harmonically unstable near the zone-boundary N and P points. The double-well potential related to motion of the trigonally coordinated Cu predicted by calculation is displayed in Figure 19. The buckling of Cu atoms approximately 0.3 Å away from the planar towards to the energy minima with depth of energy about 70 meV per formula unit.

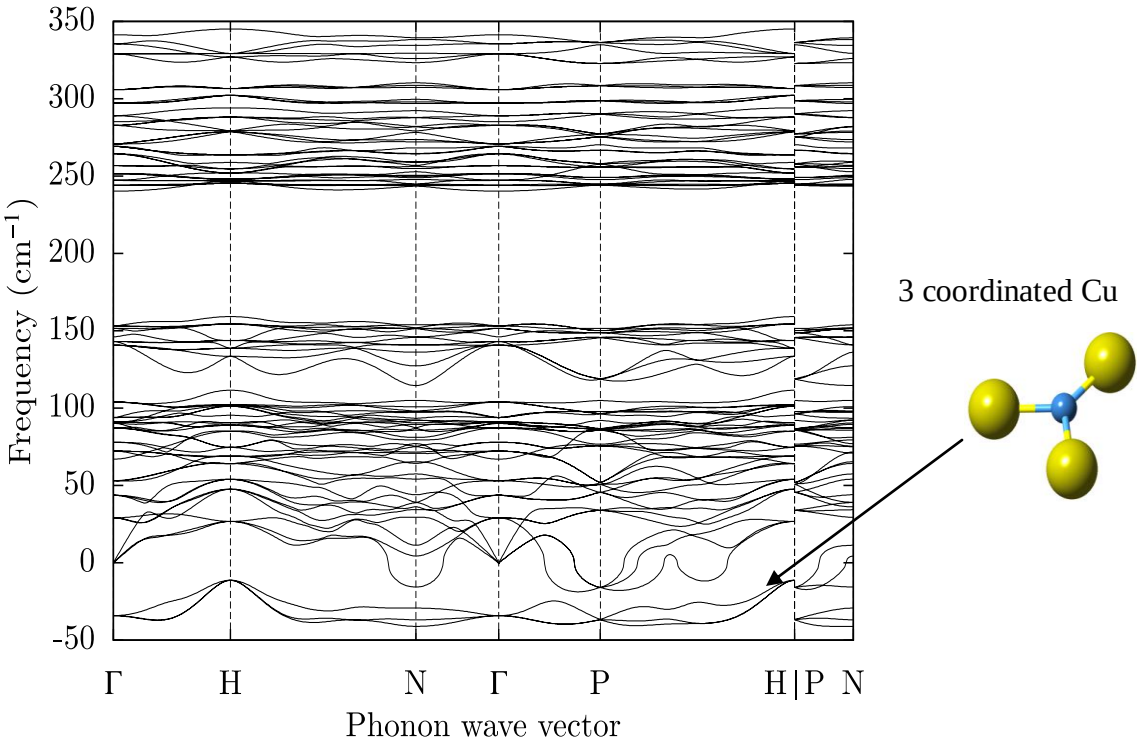

Figure 18 Calculated phonons dispersion curve of $Cu_{12}Sb_4S_{13}$.

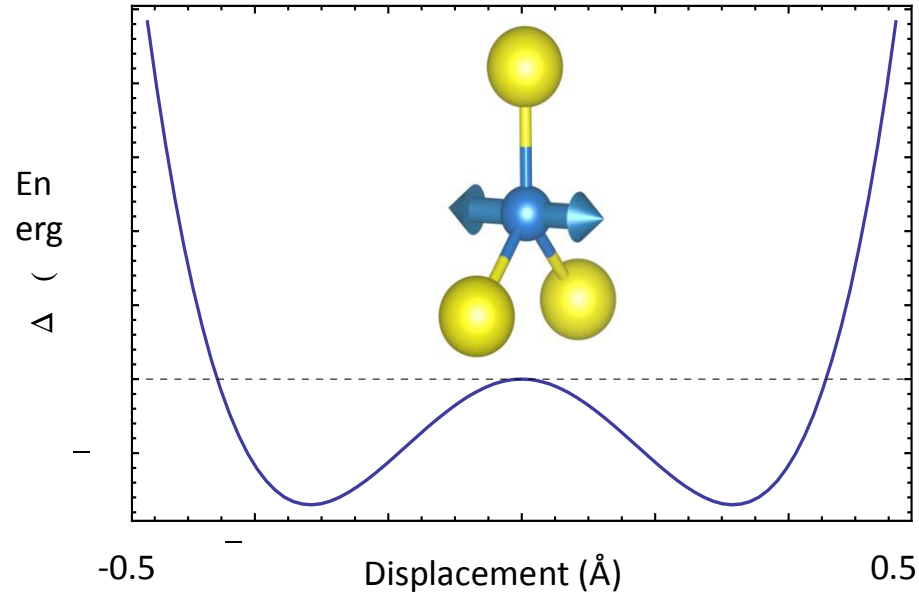

Figure 19 The illustration of motion of Cu atoms in a double well potential.

It is assumed that significant structural disorder may be induced by freezing-in of displacements of the trigonally coordinated Cu atoms at low temperatures, while at the same time leading to highly anharmonic vibrations and possible anharmonic stabilization of the cubic structure at high temperatures. The calculated phonon densities-of-states at two volumes (equilibrium volume and expanded by 6%) are shown in Figure 20. The unstable modes show strong frequency shifts towards harmonic stabilization upon increasing volume, manifesting in high Grüneisen parameters for the TA branches at zone boundaries indicated by Figure 18.

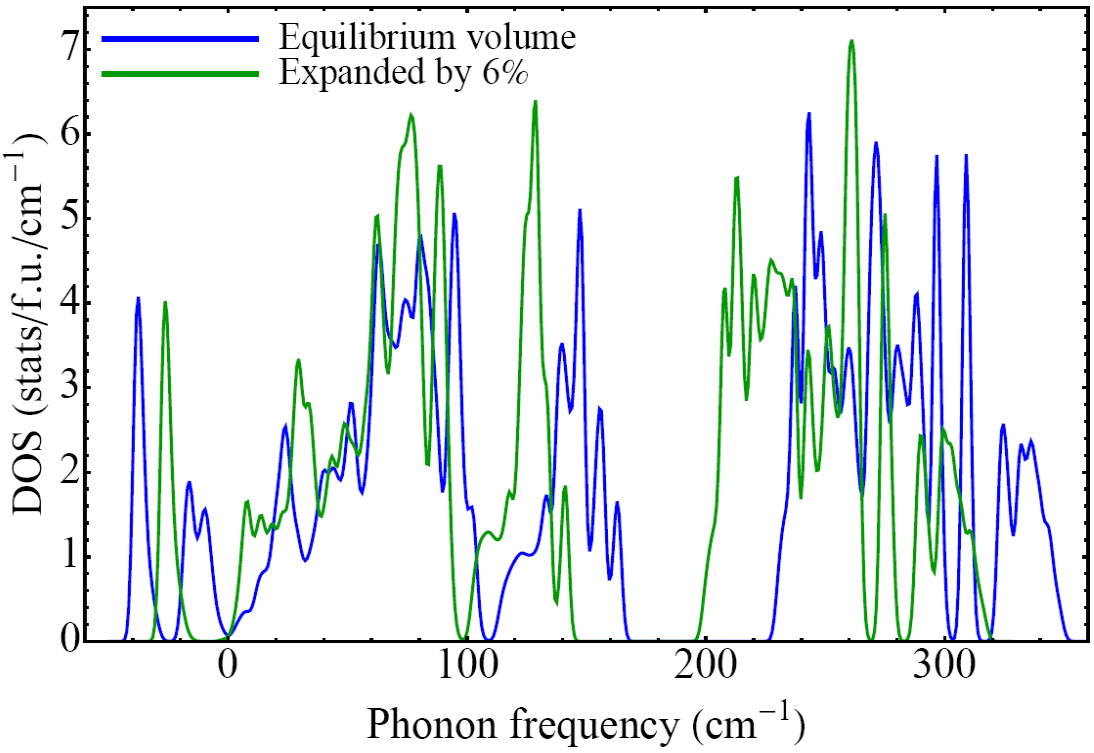

Figure 20 Calculated phonon density-of-states at the equilibrium volume V_0 (blue lines) and at V=1.06 V_0 (green lines); harmonically unstable imaginary phonon frequencies are shown as negative values.

In conclusion, by analyzing experimental data from thermal conductivity, specific heat and mechanical properties measurement, the large Grüneisen parameter and the intrinsic low thermal conductivity of tetrahedrite were confirmed. The strongest anharmonic vibration mode was predicted by specific heat analysis and found in phonon spectrum obtained by inelastic neutron scattering. Furthermore, the combined results from experimental and theoretical calculation indicated that the motion of Cu atoms out of S triangle plane in tetrahedrite structure gives rise to the strong anharmonicity and thus intrinsic low thermal conductivity. Therefore, exploration of similar crystal structure may help researchers find new TE materials with intrinsic low thermal conductivity.

Chapter 4 Thermoelectric Properties of Synthetic Tetrahedrites

Tetrahedrite is one of a family of common sulfosalt minerals with a great capacity to accommodate different metals and semimetals. It has the chemical formula $A_{10}B_2C_4D_{13}$, where A = Cu, Ag; B = Cu, Ag, Zn, Fe, Hg, Cd, Pb, Mn, Ni; C = Sb, As, Bi,Te; D = S, Se. In Chapter 3, we have already proved that the compounds with the tetrahedrite crystal structure have intrinsically low lattice thermal conductivity due to the special arrangement and valence state of the atoms comprising this material. For thermoelectric studies, the improvement in figure of merit for tetrahedrite is made by adjusting the power factor by doping/substitution. The large variation in composition of tetrahedrites on all of its four different sites gives us a good opportunity to adjust the electronic structure by substituting Cu, Sb, S using impurity atoms [74-77]. Although there are so many different combinations of substitution, here in this synthetic tetrahedrite study, we choose Zn /Fe for B site and Te for C site, which are most common impurities in naturally-occurred minerals.

4.1 Characterization and TE properties of Zn substituted $Cu_{12-x}Zn_xSb_4S_{13}$

$Cu_{12-x}Zn_xSb_4S_{13}$ samples were synthesized and prepared as described in Chapter 2. XRD patterns of $Cu_{12-x}Zn_xSb_4S_{13}$ (x = 0, 0.5, 1, 1.5) are shown in Figure 21. It is clear that after a long term annealing process, Zn atoms completely occupy the sites of stoichiometric vacancy sites of Cu atoms and cause no change in crystal structure. All peaks index to the tetrahedrite phase, and no additional peaks due to second phases are detected.

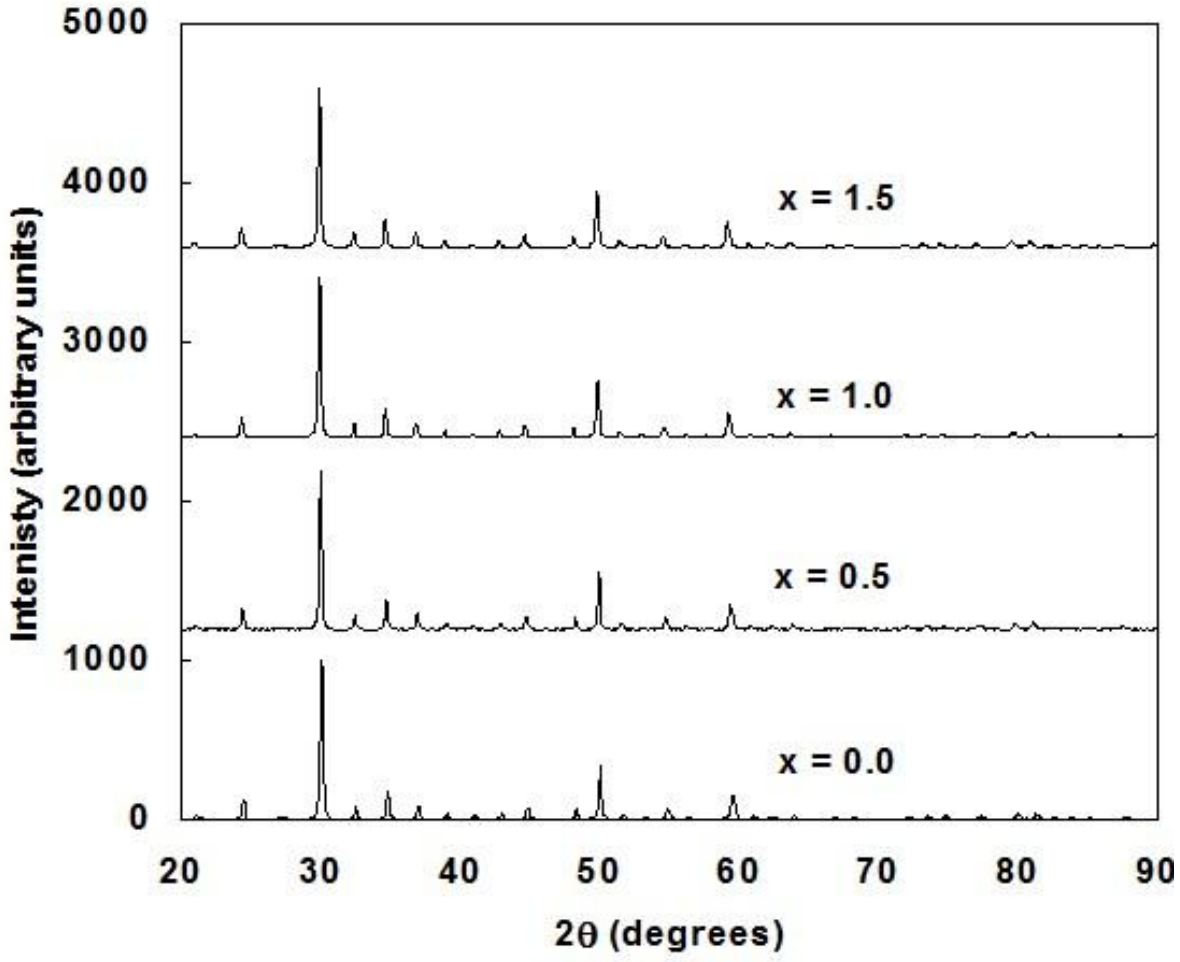

Figure 21 X-ray diffraction patterns for $Cu_{12-x}Zn_xSb_4S_{13}$ (x = 0, 0.5, 1, 1.5) .

Figure 22 shows the low temperature (80 K-330 K) electronic transport properties of $Cu_{12-x}Zn_xSb_4S_{13}$ (x = 0, 0.5, 1, 1.5). The resistivities of all samples decrease with increasing temperature, acting like other semiconductors with thermally activated carriers. The pure tetrahedrite $Cu_{12}Sb_4S_{13}$ has the lowest resistivity over all temperature range compared to other Zn substituted samples. The Seebeck coefficients of all samples increase linearly with increasing temperature. The increased Zn content will cause increase both in electrical resistivity and the Seebeck coefficients, which is typical for reduced carrier concentration in semiconductors

according to equation 32. However, the power factor is decreased by substituting Cu atoms with Zn atoms.

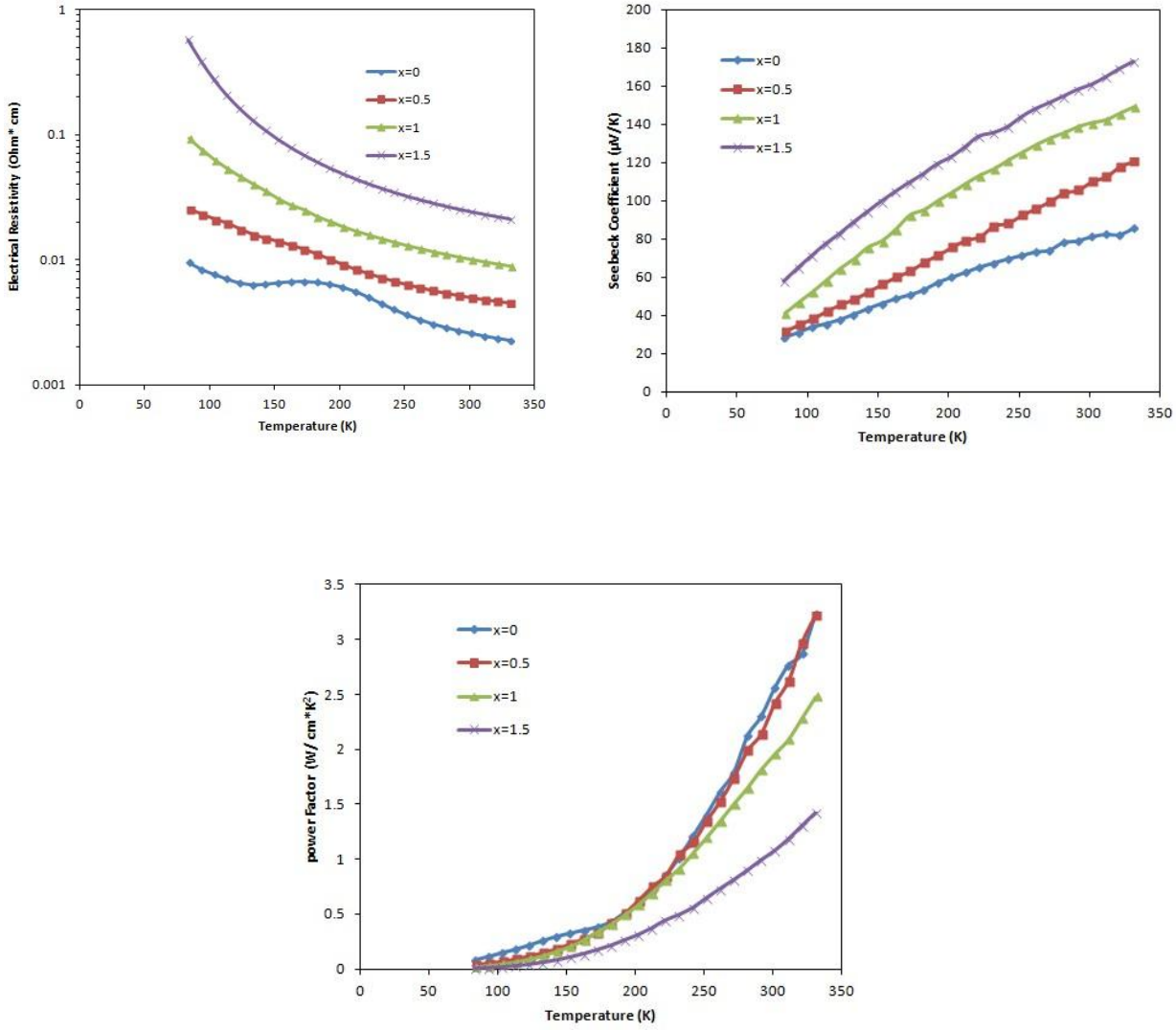

Figure 22 Temperature dependence of the electronic transport properties of $Cu_{12-x}Zn_xSb_4S_{13}$ (x = 0, 0.5, 1, 1.5)compounds at low temperature.

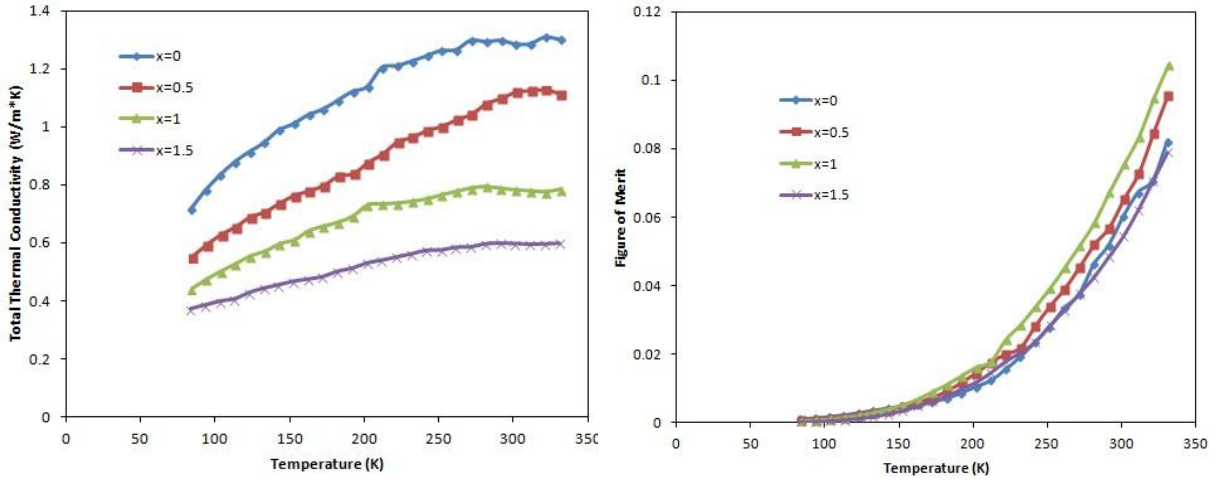

Figure 23 Temperature dependence of the total thermal conductivity and the figure of merit of $Cu_{12-x}Zn_xSb_4S_{13}$ (x = 0, 0.5, 1, 1.5) compounds at low temperature.

The total thermal conductivity shown in Figure 23 increases with temperature due to both an increased electronic part governed by Wiedemann–Franz law and a lattice part dominated by the specific heat . The calculated overall *ZT* values are enhanced by Zn substitution, especially for x = 1 sample with *ZT* over 0.1 at 330 K, which is 20 % improvement compared to pure sample.

In terms of the crystal-chemical argument given in Chapter 3, Cu atoms on B sites are divalent. It is possible that at least some of the nominally divalent Cu ions are in a monovalent or mixed valence state, giving rise to a partially filled Brillouin zone. This is proved by the results of electronic structure obtained by DFT calculation shown in Figure 24. $Cu_{12}Sb_4S_{13}$ is a metal where the Fermi level falls near a sharp peak in the density of states (DOS) at the top of the valence band, and a semiconducting gap separates the valence bands from the conduction bands. The valence bands are formed by hybridizing sulfur 3*p* and copper 3*d* orbitals; the resulting complex has two unoccupied states per formula unit. Contrary to the naive valence counting

argument given above, all copper ions are found to be in the monovalent Cu^{+} state. It is also verified that these conclusions remain qualitatively unchanged irrespective of the employed exchange-correlation functional. The absence of divalent Cu atoms in synthetic $Cu_{12}Sb_4S_{13}$ makes it has low resistivity. However, isolated divalent Cu atoms were found to exist in synthetic $Cu_{12}Sb_4S_{13}$ by magnetic and EPR measurements [58], which indicates that not all Cu atoms are in monovalent state in the real case and excess of Cu in interstitial sites may occur [78]. We will further discuss this issue in Chapter 7.

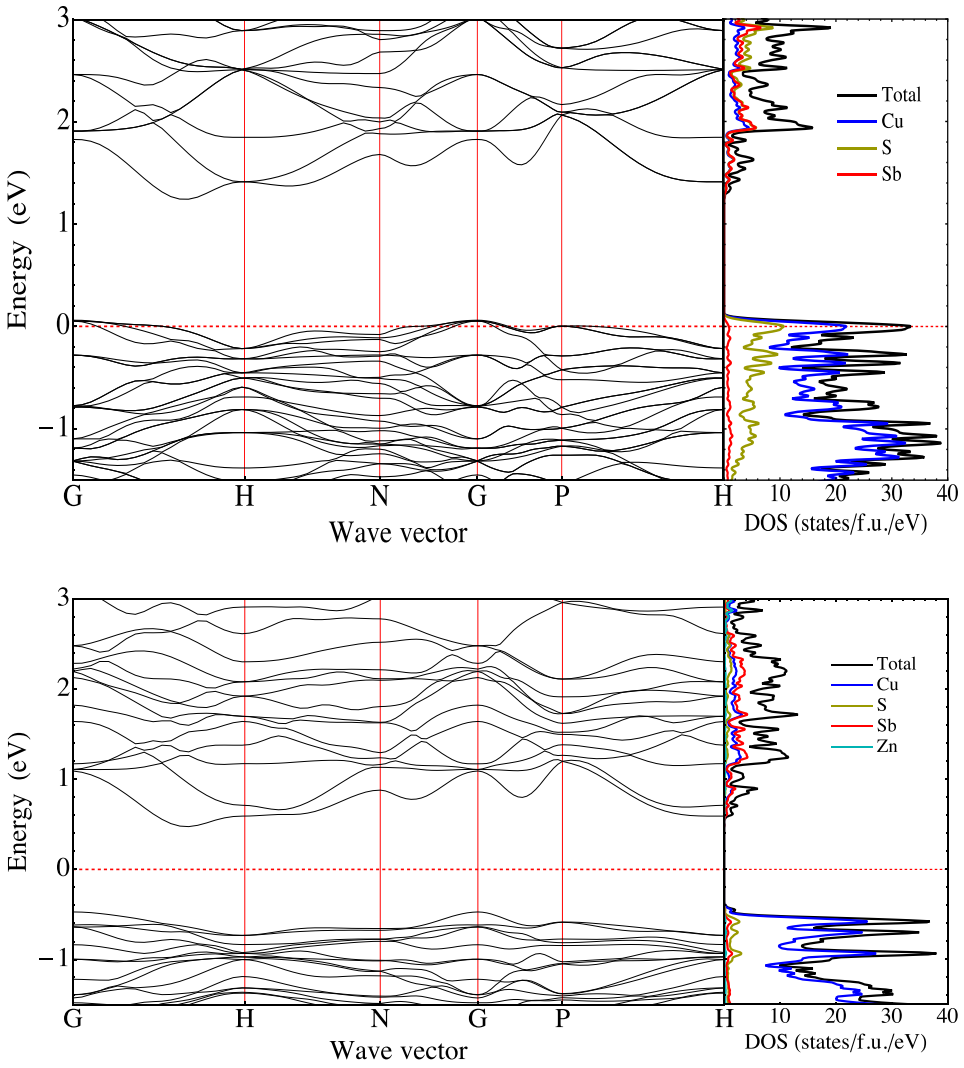

Figure 24 Calculated electronic band structure and density of states for $Cu_{12}Sb_4S_{13}$ and $Cu_{10}Zn_2Sb_4S_{13}$. The position of the Fermi level is denoted by a red dashed line.

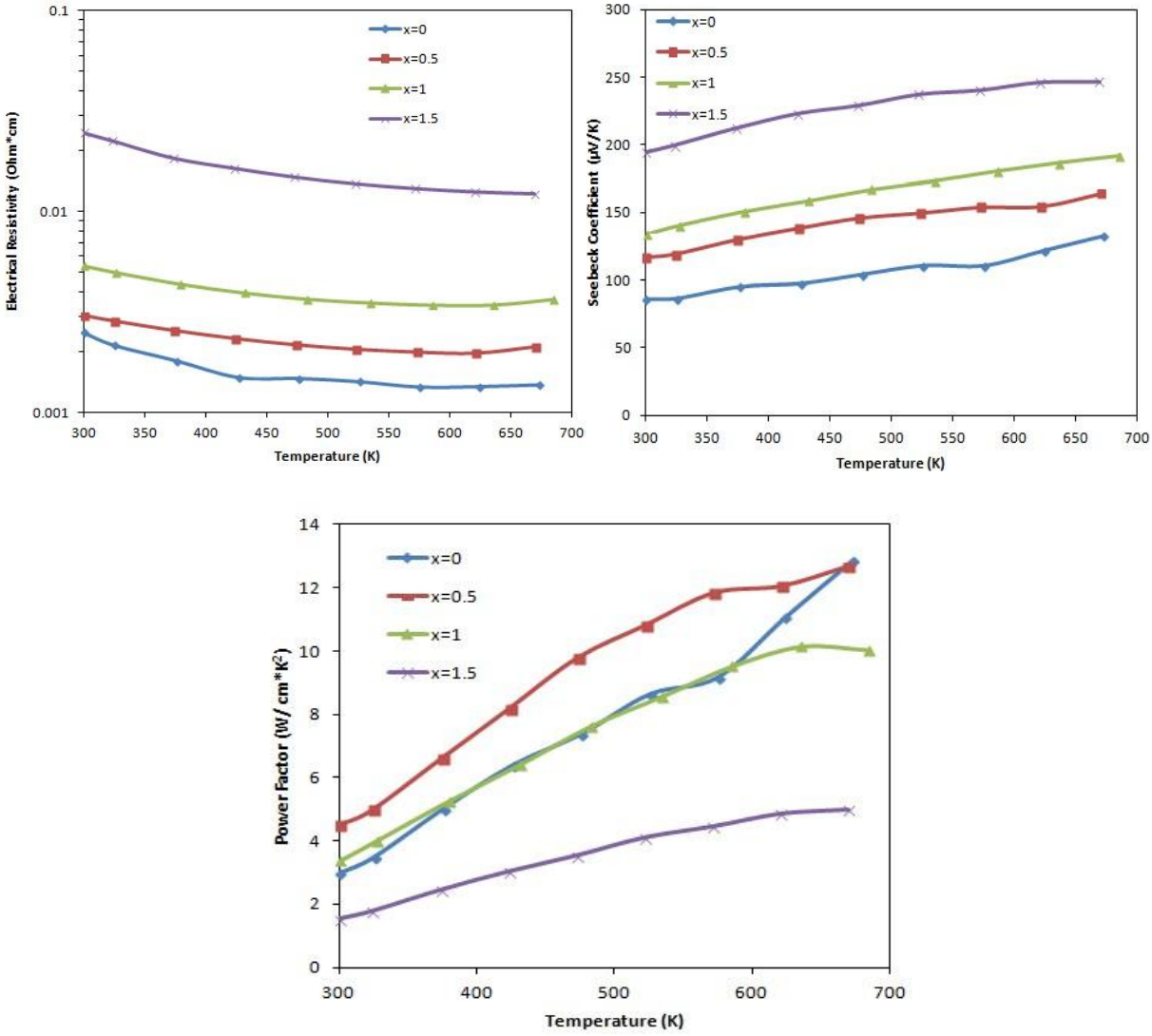

Figure 25 Temperature dependence of the electronic transport properties of $Cu_{12-x}Zn_xSb_4S_{13}$ (x = 0, 0.5, 1, 1.5) compounds at high temperature.

High temperature transport results are shown in Figure 25. In pure and lightly Zn-substituted samples (x = 0, 0.5, 1), resistivities are on the order of 10^{-3} Ohm*cm, comparable to other good thermoelectric materials. When the Zn content is increased to x = 1.5, the resistivity increases by

one order compared to the pure sample, and we find that for a Zn-substituted sample with x = 2.0 the sample is electrically insulating. Since it is expected that the Zn ion will be strictly in the Zn^{2+} state, this is consistent with complete filling of the valence bands and the occurrence of a true semiconducting state [79]. Our DFT calculations for $Cu_{10}Zn_2Sb_4S_{13}$ (as can be seen in Figure 24) confirm this conclusion. As the Zn concentration is increased the Seebeck coefficient rises considerably, exceeding 200 μV /K at the highest temperatures for the x = 1.5 sample. This is consistent with the filling of holes in the valence band and pushing the Fermi level towards the steep slope of the DOS peak (Figure 24) as zinc replaces copper. Above room temperature, with resistivity values in the 10^{-3} Ohm cm range and Seebeck coefficients ~100 – 200 μV/K, these tetrahedrites have thermoelectric power factors comparable to some of the best thermoelectric materials (such as PbTe) in this temperature range. The pure $Cu_{12}Sb_4S_{13}$ has the highest power factor of 12 W/cm*K^2 at 700 K.

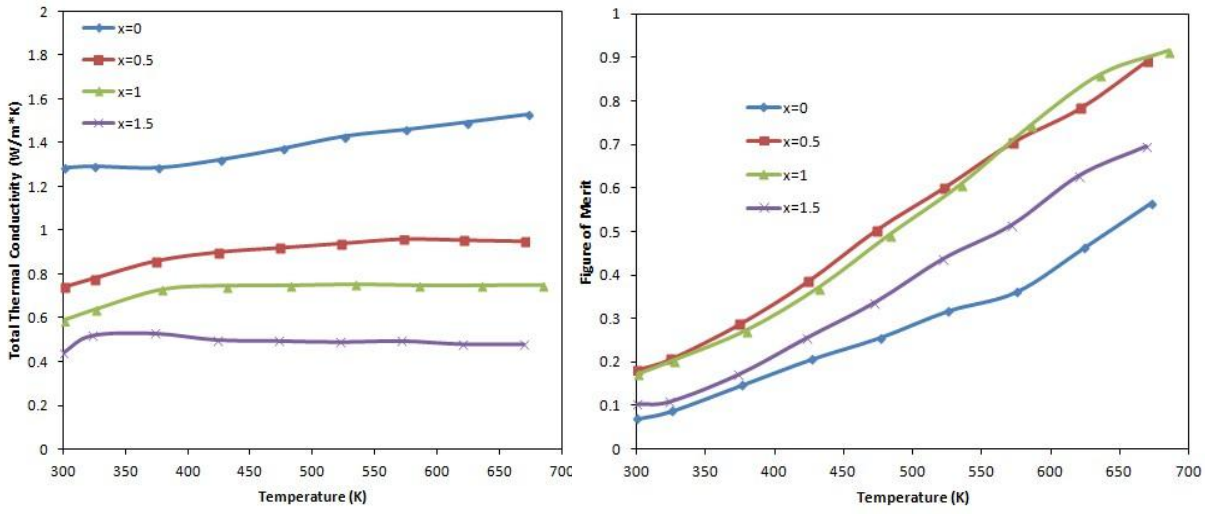

Figure 26 Temperature dependence of the total thermal conductivity and the figure of merit of $Cu_{12-x}Zn_xSb_4S_{13}$ (x = 0, 0.5, 1, 1.5) compounds at high temperature.

Turning now to the thermal conductivity, Figure 26 displays thermal conductivity derived from our thermal diffusivity measurements above room temperature. The thermal conductivity falls monotonically with increasing Zn substitution. This reflects the combined effects of a reduced electronic component of thermal conductivity and a decreasing lattice contribution. The thermal conductivity curves of all Zn substituted samples are flat and all lie below 1 W/m*K. By simply subtracting the electronic part from the total thermal conductivity, the lattice thermal conductivities of these compounds should be close to the theoretical minimum we discussed in Chapter 3. The combination of high thermoelectric power factor and low thermal conductivity in these compounds leads to large thermoelectric figure of merit. Although the power factor of the x = 1.5 sample is less than half that of the x = 0 sample, the *ZT* value at x = 1.5 is still higher than that of pure sample, approaching 0.7 at 700 K. The maximum *ZT* value near unity is attained for x = 1 at 700 K. The high *ZT* values are maintained for relatively large Zn substitutions due to the compensating effect from the reduction in thermal conductivity. As can be seen from Figure 26, the total thermal conductivity of the x = 1.5 sample was reduced to one third of that of pure sample at high temperature. The reduction in total thermal conductivity can be mainly attributed to the decreased electronic thermal conductivity. Because the lattice thermal conductivity in these compounds is so low, we find, somewhat ironically, that reducing the power factor actually leads to a 60% enhancement in *ZT* value for the case of the x = 1 for Zn substitution, due to reduction in electronic thermal conductivity.

4.2 Characterization and TE properties of Fe substituted $Cu_{12-x}Fe_xSb_4S_{13}$

$Cu_{12-x}Fe_xSb_4S_{13}$ (x = 0.2, 0.5, 0.7) compounds were synthesized to investigate the effect of Fe substitution for Cu in tetrahedrite. XRD patterns of synthetic $Cu_{12-x}Fe_xSb_4S_{13}$ are shown in Figure 27. All the main peaks index to the tetrahedrite phase.

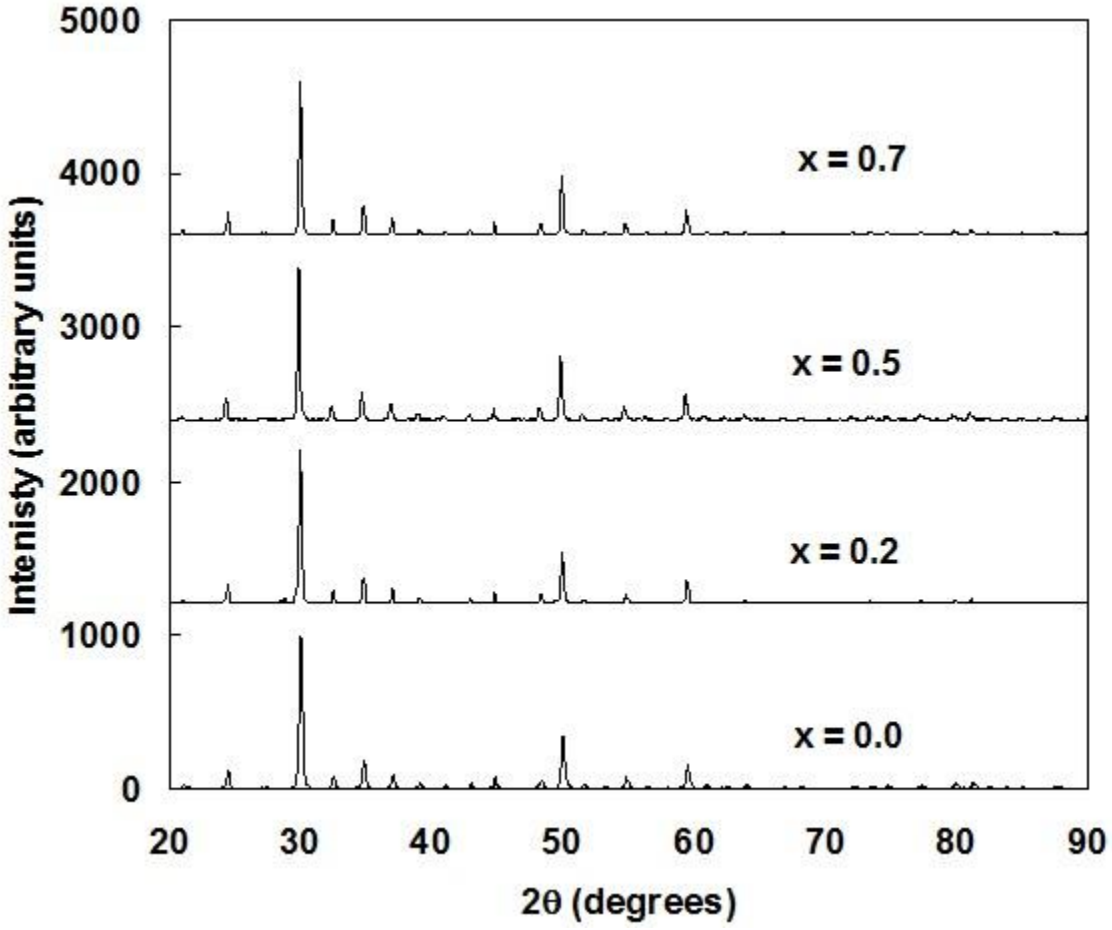

Figure 27 X-ray diffraction patterns for $Cu_{12-x}Fe_xSb_4S_{13}$ (x = 0.2, 0.5, 0.7).

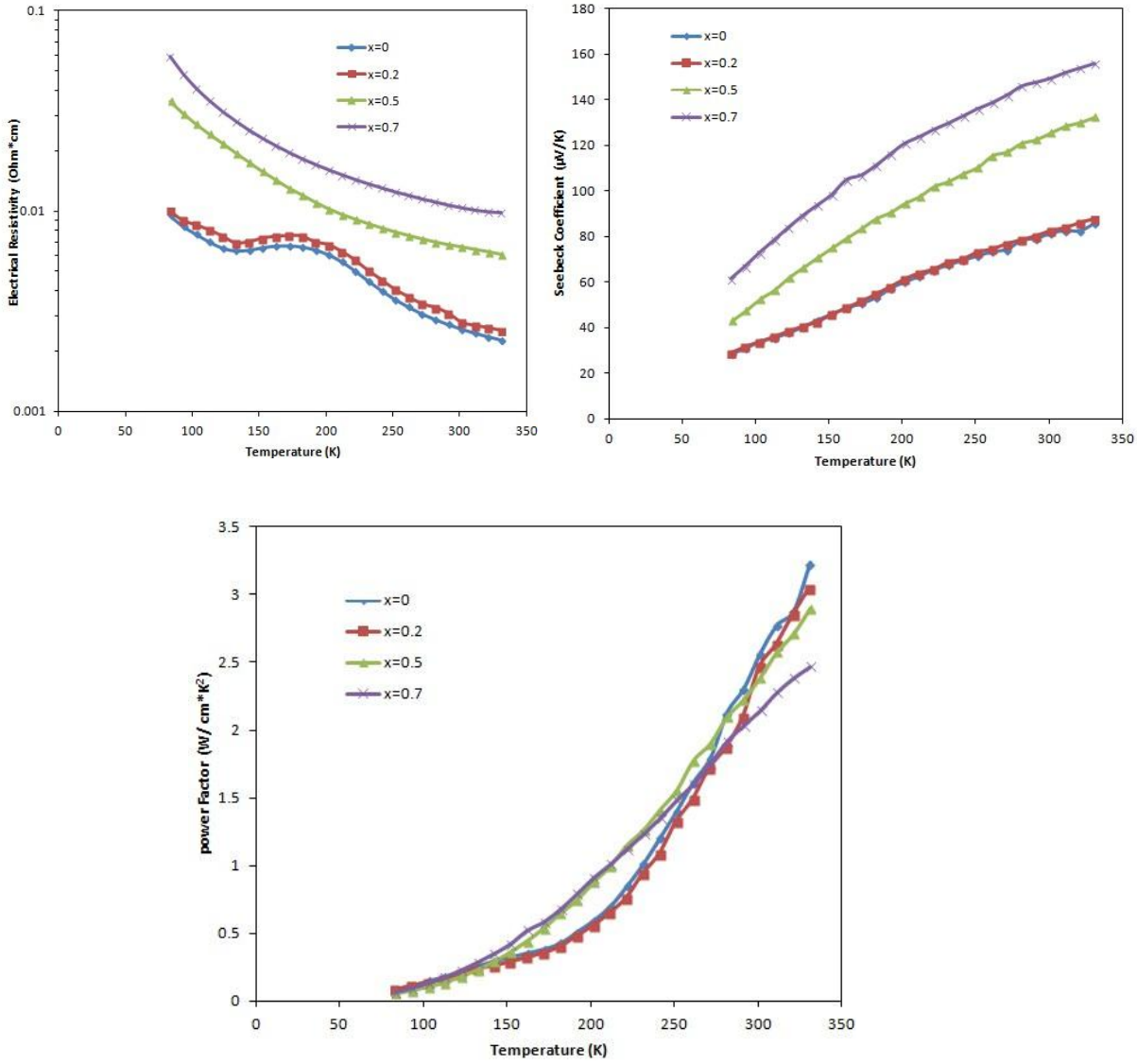

Figure 28 Temperature dependence of the electronic transport properties of $Cu_{12-x}Fe_xSb_4S_{13}$ (x = 0.2, 0.5, 0.7) compounds at low temperature.

As shown in Figure 28, for x < 1 Fe substituted samples, their electrical transport properties are similar to those of Zn substituted samples. All the samples behave like semiconductor sand both electrical resistivities and Seebeck coefficients increase with increased Fe content. For

those samples, the power factors do not change too much compared to the pure sample. For example, in x = 0.7 case, the power factor drops from 3.2 (pure sample) to 2.5 W/cm*K^2.

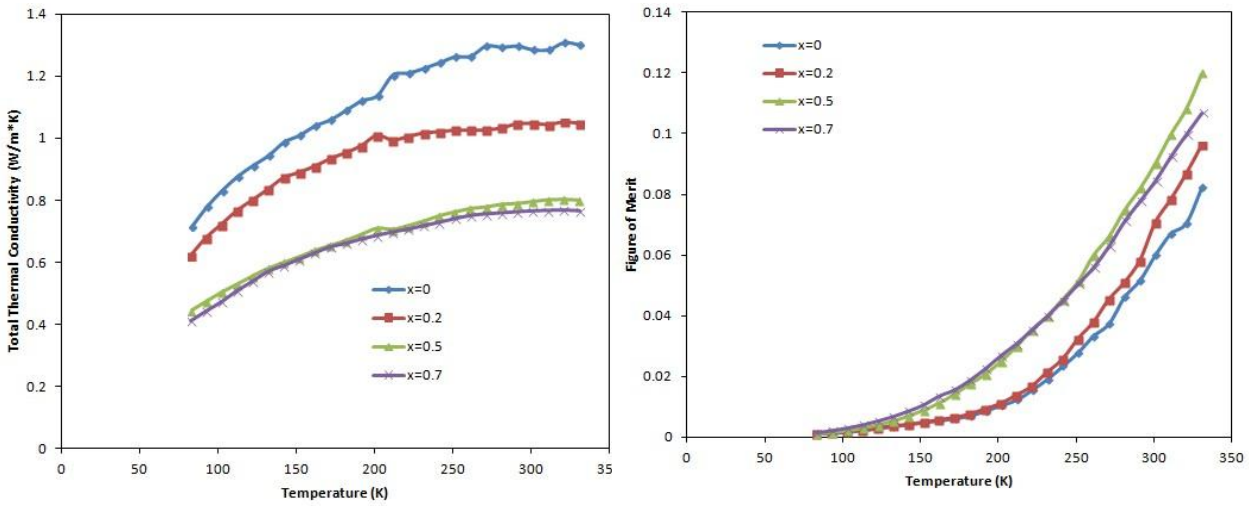

Figure 29 Temperature dependence of the total thermal conductivity and the figure of merit of $Cu_{12-x}Fe_xSb_4S_{13}$ (x = 0.2, 0.5, 0.7) compounds at low temperature.

Figure 29 shows the total thermal conductivity and the figure of merit of $Cu_{12-x}Fe_xSb_4S_{13}$ (x = 0.2, 0.5, 0.7) compounds at low temperature. Compared to Zn substituted samples, Fe substitution reduces the thermal conductivity more effectively, presumably due to the additional phonon scattering from magnetic ions, although we do not explore this possibility further here The figure of merit is enhanced for all samples up to 330 K and the maximum *ZT* value is obtained in x = 0.5 sample with *ZT* close to 0.12 at 330 K. This difference between Fe and Zn substitution has its origin in the different valence states of Fe and Zn in tetrahedrite. Makovicky et al. have shown that Fe in synthetic $Cu_{12-x}Fe_xSb_4S_{13}$ is trivalent for $0 < x < 1$ and divalent for 1

$\leq x \leq 2$ [80]. This implies that, in the composition range measured here, each Fe atom can provide an extra electron to fill holes in the valence band compared to that of each Zn atom, and explains why Fe substitution causes a larger increase in resistivity for the same x value. The DFT calculations (shown in Figure 30) confirm this interpretation, showing that iron in $Cu_{11}FeSb_4S_{13}$ is indeed in the Fe^{3+} s^0d^5 configuration due to the formation of an exchange gap of approximately 3 eV between the Fe majority and minority spin states, which pushes the latter above the valence band maximum. Majority-spin Fe e_g and t_{2g} states are, respectively, at approximately -3 and -2.5 eV relative to the Fermi level, which is shown as a dashed red line. The minority spin states are just above the Fermi level; e_g states are slightly split by crystal field effects due to deviations from tetrahedral symmetry on the Cu sites. So iron is found to be in the high-spin d^5 configuration of Fe^{3+} in this calculation.

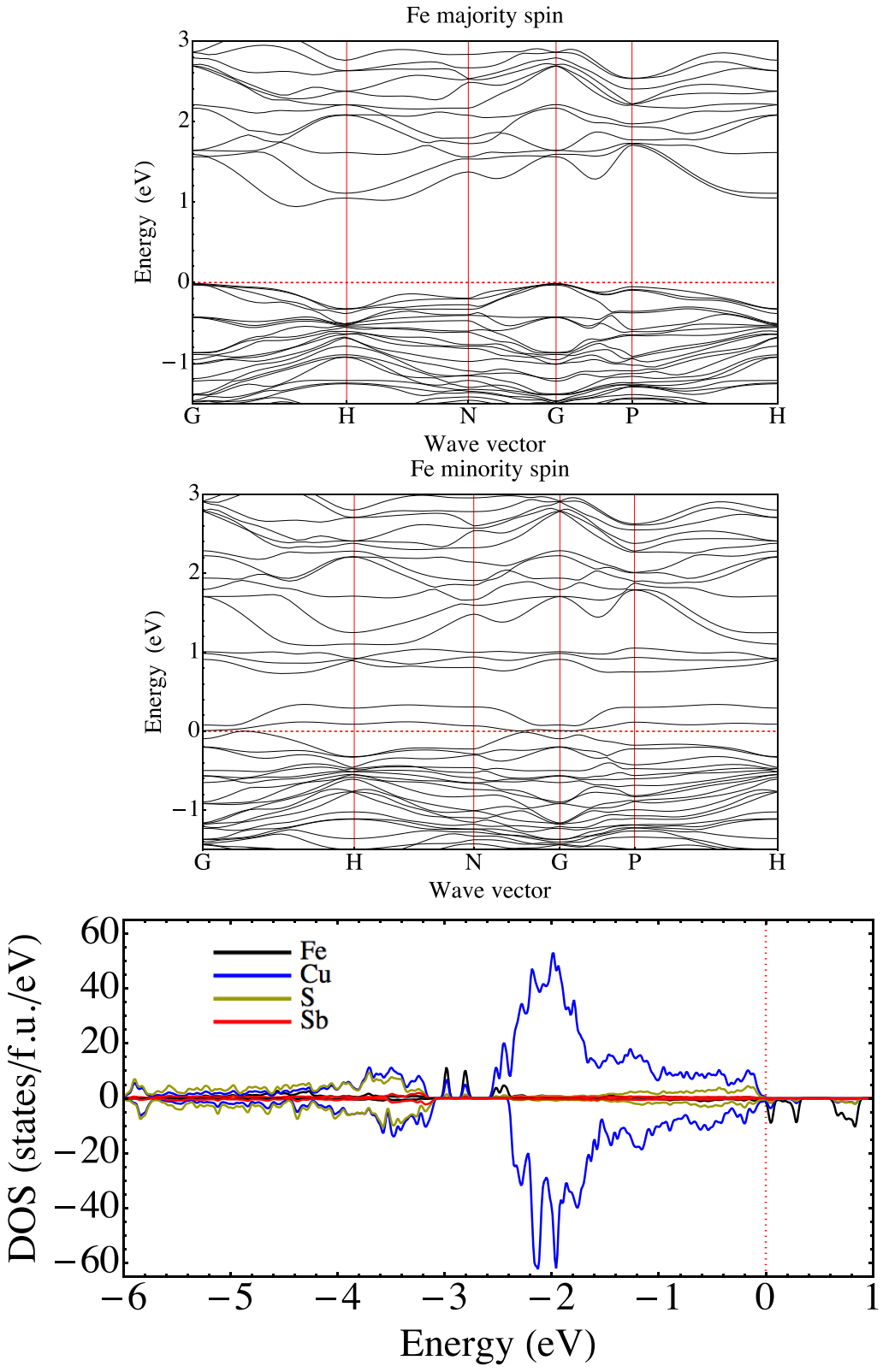

Figure 30 Calculated electronic band structure and density of states for $Cu_{11}FeSb_4S_{13}$. Fe atom substitutes on a tetrahedrally coordinated Cu site.

In order to understand more about the effect of different valence states of Fe on tetrahedrite transport properties, further Fe substitution was performed with x = 1, 1.2 and 1.5. Figure 31 shows the results of XRD patterns of $Cu_{12-x}Fe_xSb_4S_{13}$ (x = 1, 1.2, 1.5), indicating all the three samples are single phase tetrahedrite.

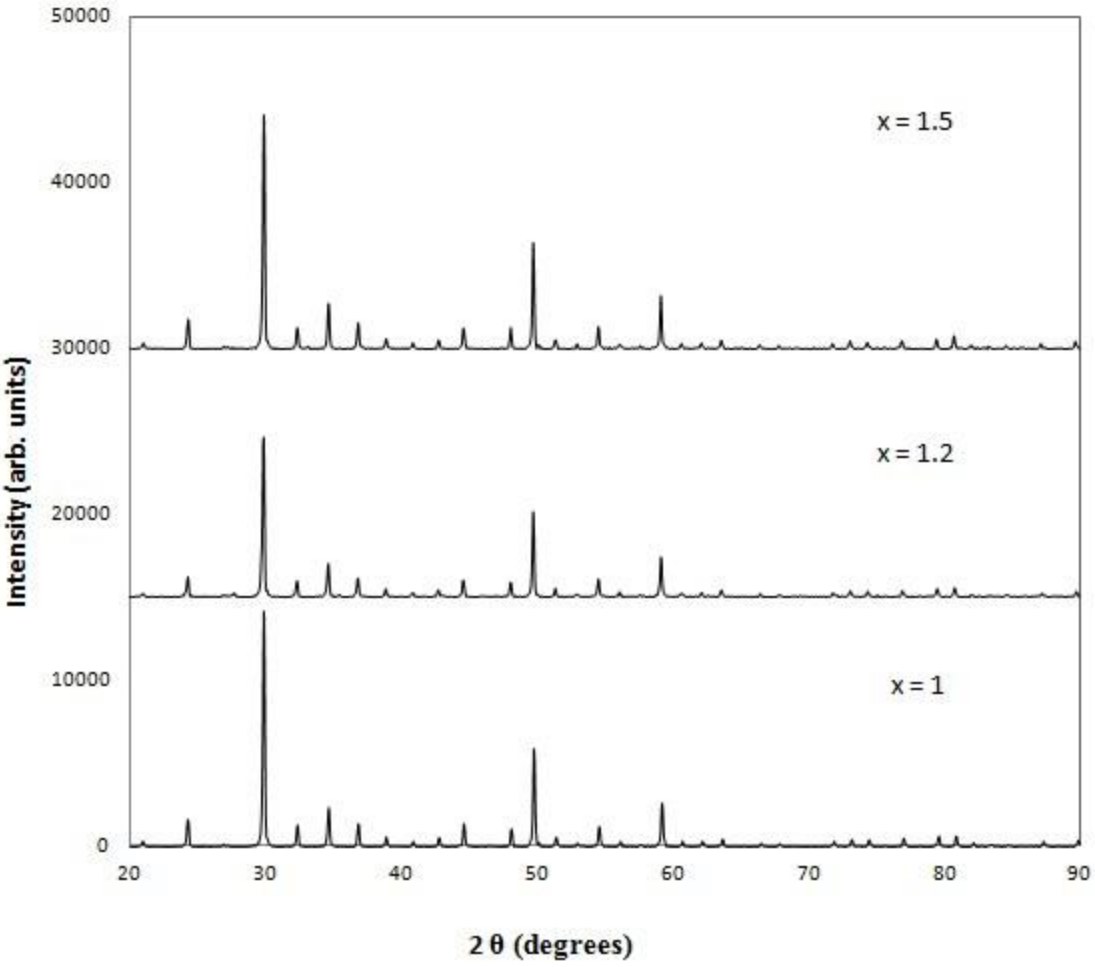

Figure 31 X-ray diffraction patterns for $Cu_{12-x}Fe_xSb_4S_{13}$ (x = 1, 1.2, 1.5).

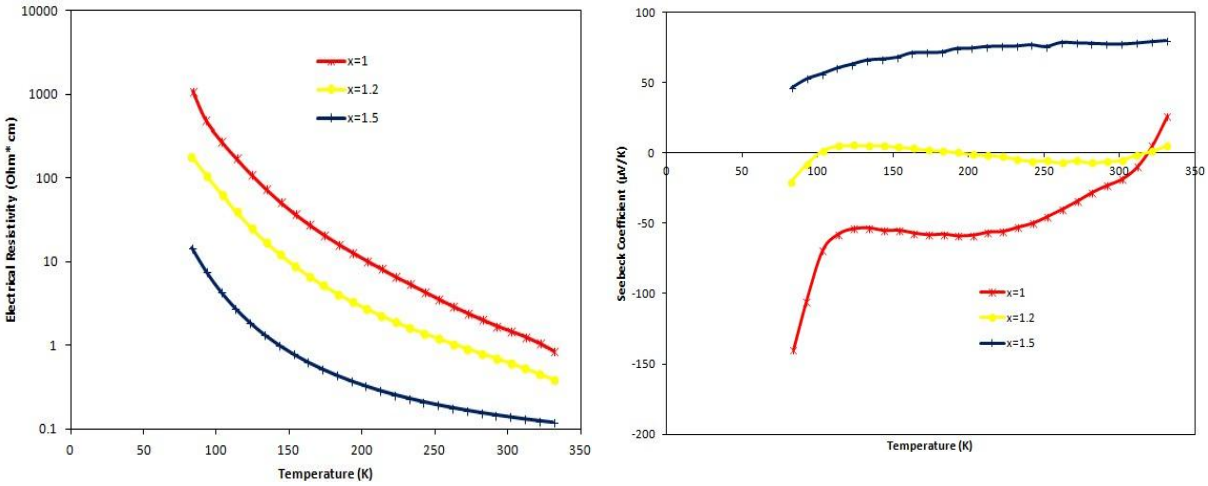

Figure 32 Temperature dependence of the electronic transport properties of $Cu_{12-x}Fe_xSb_4S_{13}$ (x = 1, 1.2, 1.5) compounds at low temperature.

Figure 32 displays the resistivities and the Seebeck coefficients of $Cu_{12-x}Fe_xSb_4S_{13}$ (x = 1, 1.2, 1.5). The resistivity of $Cu_{11}FeSb_4S_{13}$ is two orders of magnitude larger than that of $Cu_{11}ZnSb_4S_{13}$ at 330 K. This confirms our argument above that the two electrons provided by Fe^{3+} will completely fulfill the hole states in valence band, rendering $Cu_{11}FeSb_4S_{13}$ insulating. When x is larger than 1, some of Fe atoms are turned into Fe^{2+}, giving rise to new holes in valence band. This explains why Fe content is increased to 1.5, the resistivity drops almost 1 order of magnitude. Interestingly, the Seebeck coefficient of $Cu_{11}FeSb_4S_{13}$ is negative before the temperature reaches 320 K. This is because the stoichiometry of $Cu_{11}FeSb_4S_{13}$ may not be perfect, and excess Fe atoms near the critical point for valence change will cause excess electrons in this system. At low temperatures, the negative carriers dominate in the electrical transport, making the $Cu_{11}FeSb_4S_{13}$ n-type. With increasing temperature, more positive carriers are activated, participating in the transport process, first reducing the absolute value of Seebeck coefficient, and then eventually causing it to become positive above 320 K. For x = 1.2 sample, the added Fe atoms create new hole states in the compound, making the number of two types of

carriers to become comparable. Due to the compensation effect from equation 35, the Seebeck coefficient of $Cu_{10.8}Fe_{1.2}Sb_4S_{13}$ fluctuates below and above zero. When x = 1.5, the positive carriers become predominant but negative minority carriers still exist. Therefore, $Cu_{10.5}Fe_{1.5}Sb_4S_{13}$ has a positive but small Seebeck coefficient. Compared to pure $Cu_{12}Sb_4S_{13}$ with more than 1 order of magnitude smaller resistivity than that of $Cu_{10.5}Fe_{1.5}Sb_4S_{13}$, the Seebeck coefficients are the same at room temperature. In all, for $x \geq 1$ Fe substituted tetrahedrite samples, two type of carriers coexist and resistivities are high, resulting in power factor less than 0.1 $W/cm*K^2$ at room temperature. Therefore, no further high temperature measurement were taken on these samples.

At high temperature, like their Zn substituted counterparts, the Fe substituted samples display similar trends of an increase in resistivity, enhancement in the Seebeck coefficient and reduction in the total thermal conductivity. The *ZT* value reaches a maximum of over 0.8 at x = 0.5 and decreases for higher values of x. The high temperature results are shown in Figure 33 and Figure 34.

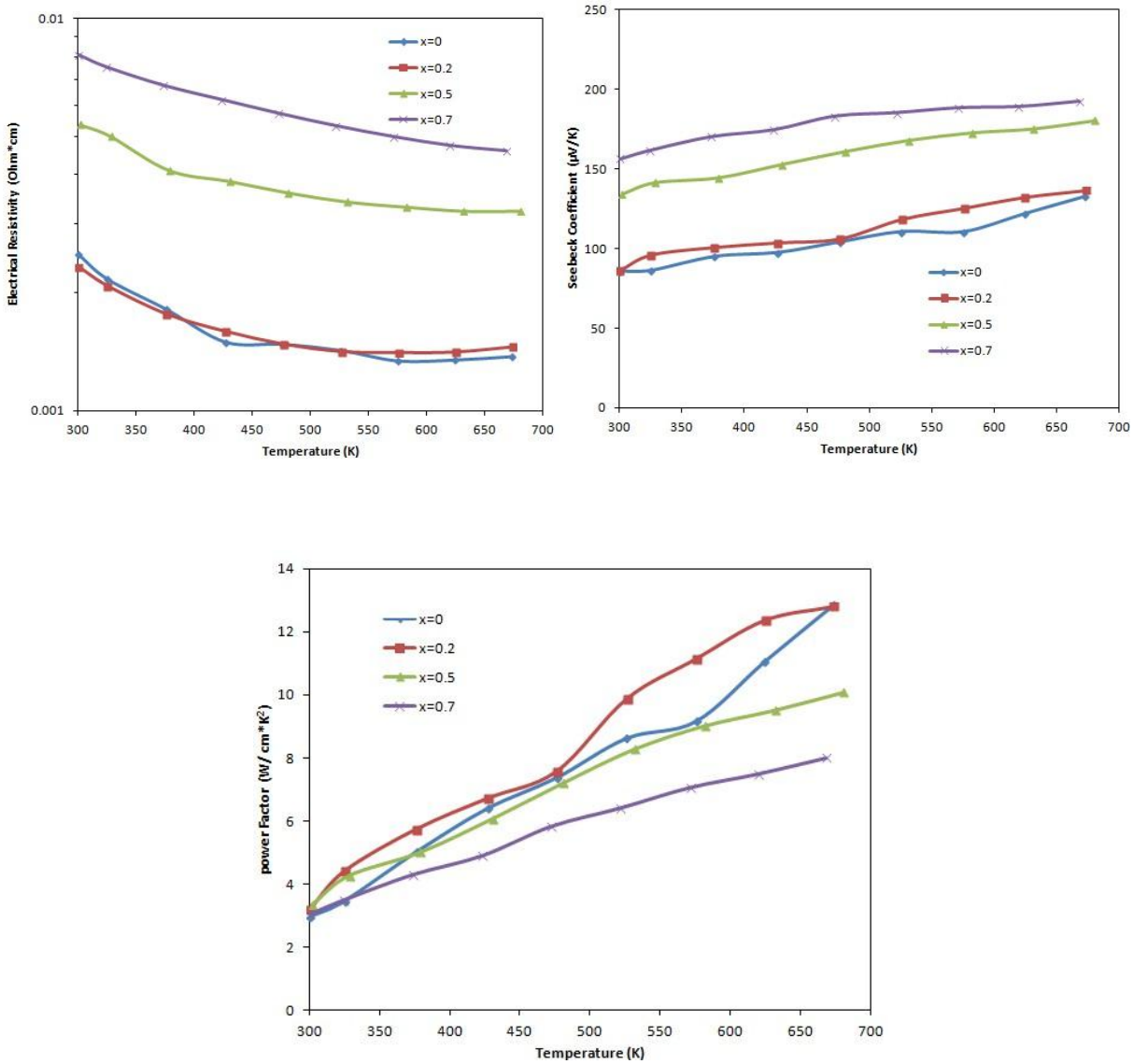

Figure 33 Temperature dependence of the electronic transport properties of $Cu_{12-x}Fe_xSb_4S_{13}$ (x = 1, 1.2, 1.5) compounds at high temperature.

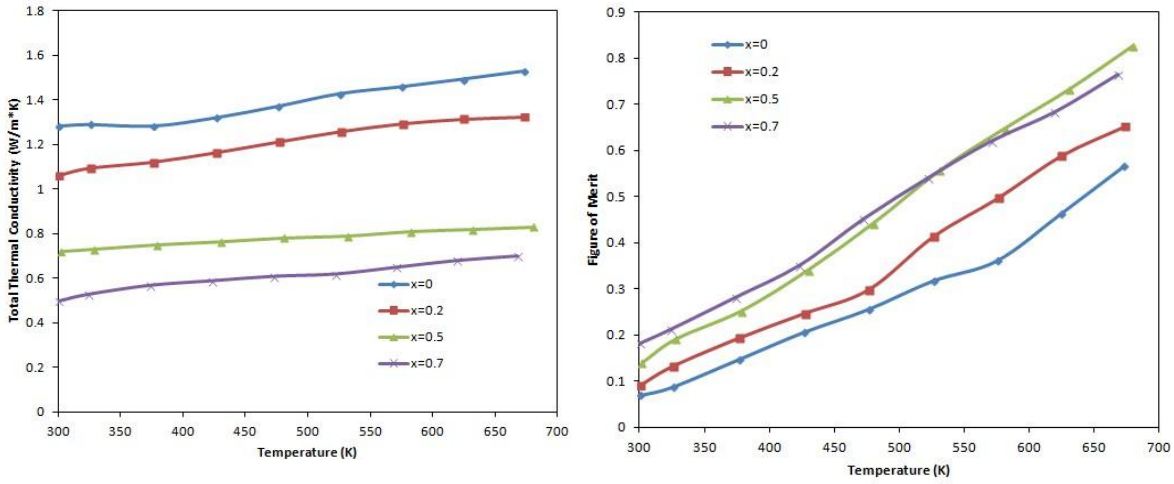

Figure 34 Temperature dependence of the total thermal conductivity and the figure of merit of $Cu_{12-x}Fe_xSb_4S_{13}$ (x = 0.2, 0.5, 0.7) compounds at high temperature.

4.3 A Simple Brillouin Zone hole filling model for Zn and Fe substituted tetrahedrite

As discussed in the previous section, there is balance between power factor and figure of merit, which means the maximum power factor does not naturally lead to maximum *ZT* value. . Because the lattice thermal conductivity of these compounds is so small, the electronic thermal conductivity plays a special role in controlling their thermoelectric properties. With increasing impurity content, the resistivity rises, causing the power factor to decrease, but this is more than made up for by a decrease in electronic thermal conductivity. In order to understand the relationship between composition and the resulting *ZT* values, we introduce the notion of the fraction (*f*) of hole states filled in the valence band upon substitution: $f = xN_e/2$, where N_e is the number of excess contributed electrons from each M ion [81]. For example, for x = 0.5 Fe substitution (N_e = 2), the fraction is 0.5, while for x = 0.5 Zn substitution (N_e = 1), the fraction is 0.25. In order to simplify the model, we assume all the Cu atoms are monovalent here. Figure 35

displays the relationship between filling fraction of holes and the measured *ZT* values. For both substitutions, the maximum *ZT* values are reached at 0.5 and *ZT* begins to diminish for higher filling fraction. From this plot we see that *ZT* values above 0.8 can be attained over a surprisingly large range of composition; high *ZT* is extremely robust against impurity substitution on the copper site in $Cu_{12}Sb_4S_{13}$, with high values maintained up to a hole filling fraction of 0.8, even if the substitution is a mixture of more than one kind of atom. Since this range of substitution over which high *ZT* is maintained exceeds significantly the range of composition of natural tetrahedrites, it is quite likely that natural mineral tetrahedrites can be used directly as thermoelectric materials, which we will discuss in Chapter 6.

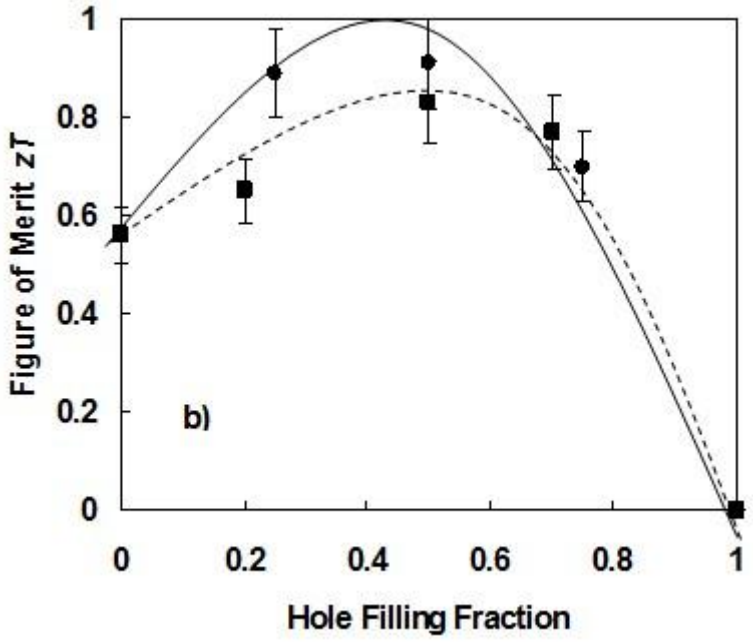

Figure 35 Figure of merit versus fraction of hole states filled in the valence band for $Cu_{12-x}M_xSb_4S_{13}$ (M = Zn :circle, Fe: square).

4.4 Characterization and TE properties of Te substituted $Cu_{12}Sb_{4-x}Te_xS_{13}$

The above study on tetrahedrites was focused on the substitution of transition metal elements (Zn, Fe, Ni...) for Cu and no substitution effect was investigated for Sb atoms. In natural minerals, the Sb sites in tetrahedrite are invariably replaced by As, Bi or Te atoms. In the last case, the tellurium phases of the tetrahedrite solid solution series will maintain the chemical formula $Cu_{12}Sb_{4-x}Te_xS_{13}$ up to x = 2, whereas higher levels of Te substitution result in reduced Cu concentration and vacancies, giving rise to another endmember of the tetrahedrite family, $Cu_{10}Te_4S_{13}$, known as goldfieldite [82]. Unlike As and Bi substitutions, which are not expected to affect the transport properties, the Te atom has an extra electron with respect to Sb, and thus can change the Fermi level in the electronic structure [83].

$Cu_{12}Sb_{4-x}Te_xS_{13}$ (x = 0.1, 0.5, 1, 1.5, 2) and $Cu_{10}Te_4S_{13}$ samples were synthesized by the method described in Chapter 2. As expected, the substitution of Te for Sb does not cause a change in the crystal structure up to x = 2. The XRD patterns of all the $Cu_{12}Sb_{4-x}Te_xS_{13}$ (x = 0.1, 0.5, 1, 1.5, 2) are those of single phases. However, for $Cu_{10}Te_4S_{13}$ sample with two missing Cu atoms in each unit cell, an additional peak related to the vacancies appears.

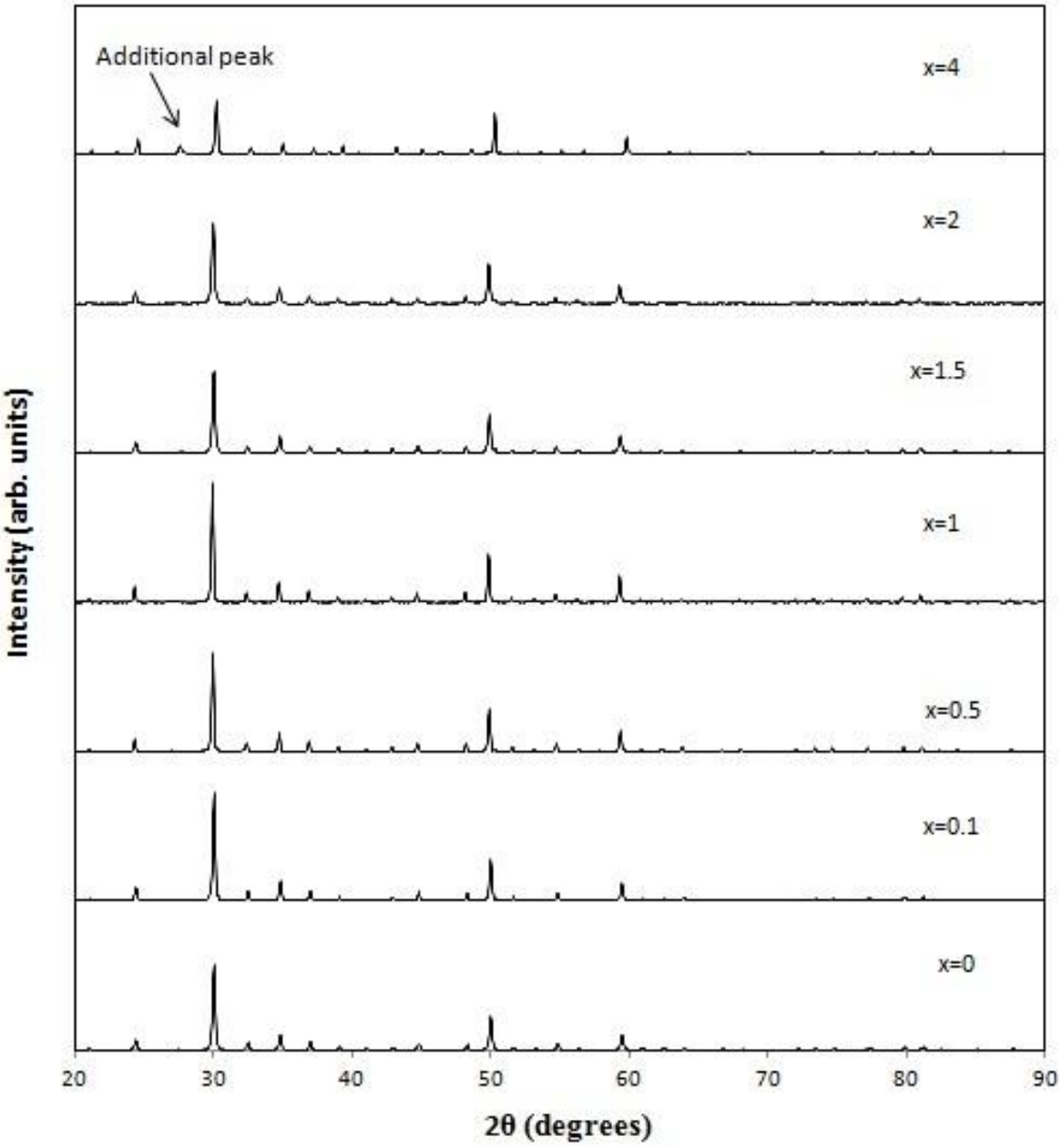

Figure 36 X-ray diffraction patterns for $Cu_{12}Sb_{4-x}Te_xS_{13}$ (x = 0.1, 0.5, 1, 1.5, 2) and $Cu_{10}Te_4S_{13}$.

Figure 37 shows SEM images of the fractured surface of $Cu_{12}Sb_3TeS_{13}$ after hot pressing. A high magnification image shows that the particle size of this sample ranges from 50 nm to 200

nm. The smaller particle size, which may cause more phonon scattering, is another factor for the low thermal conductivity. A lower magnification image was also taken on a polished flat area of the same sample (Figure 37). No second phases are observed in image.

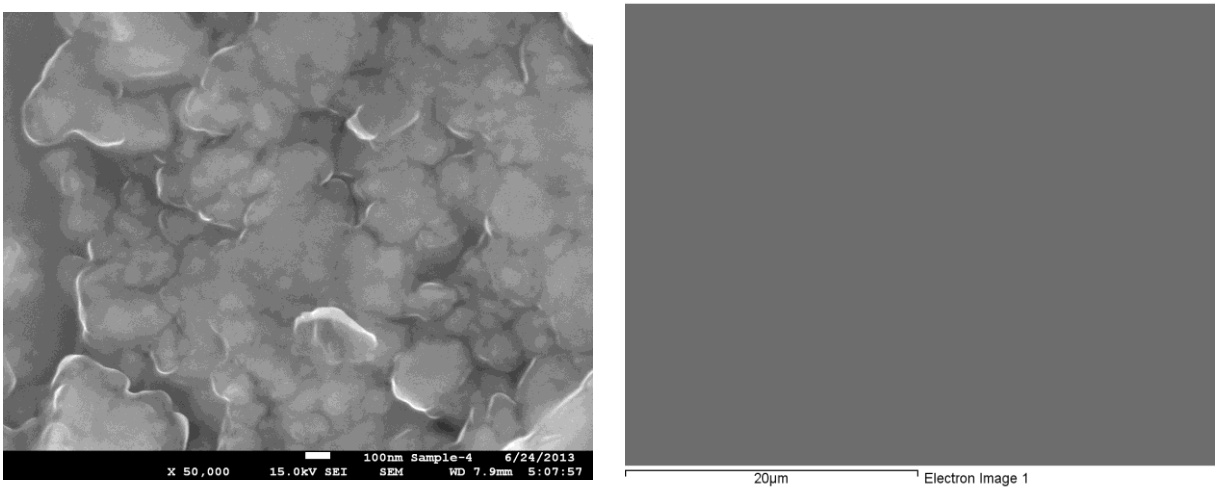

Figure 37 SEM images of $Cu_{12}Sb_3TeS_{13}$. Left : fractured surface; Right : polished surface.

The surface looks clean and dense without any precipitates or impurity clusters. EDS analysis was also performed on the same flat area of the low magnification SEM image. The major elements distribution mapping results (Figure 38) show that all these elements are homogeneously distributed throughout the sample, further indicating the successful Te substitution.

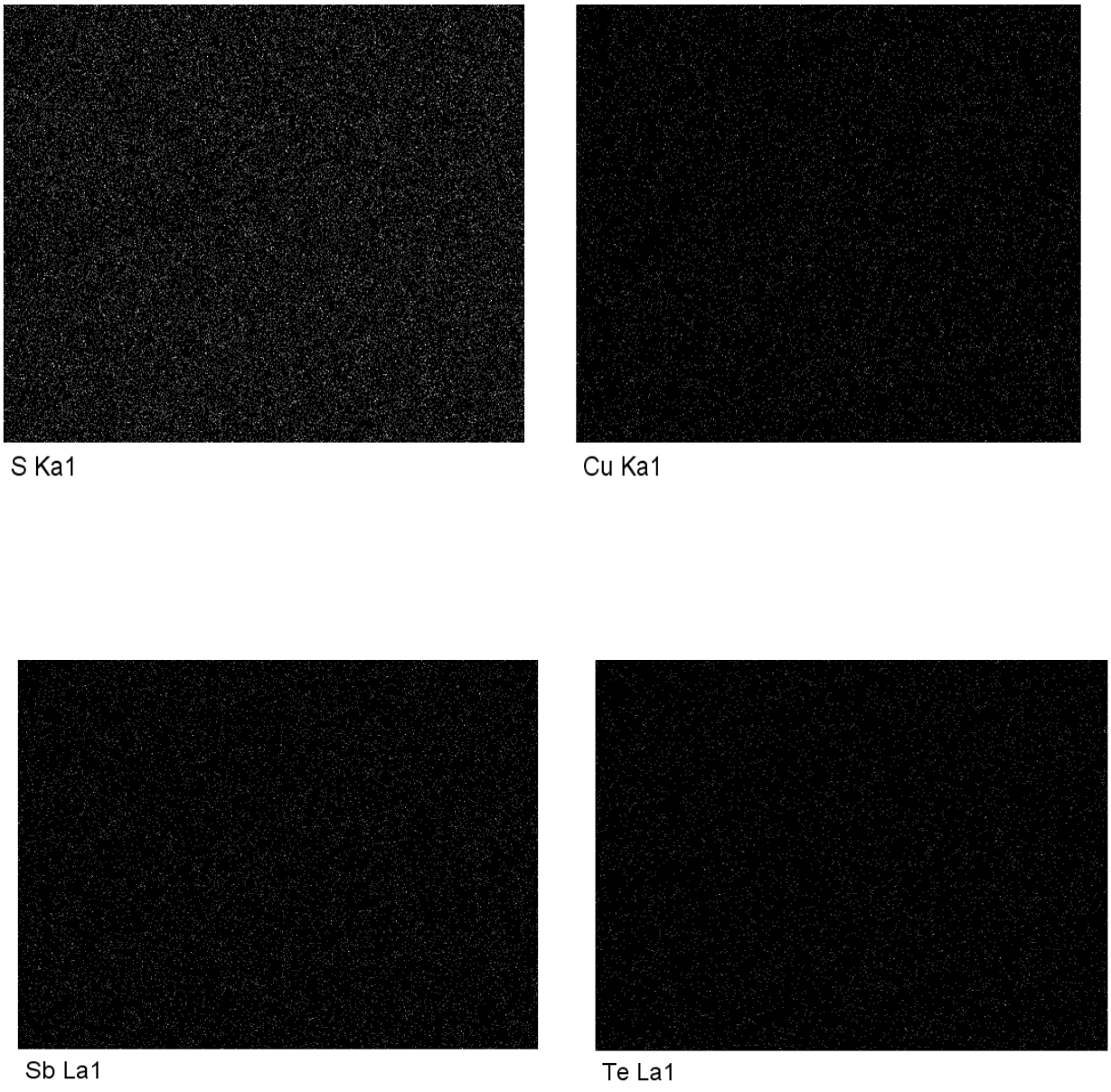

Figure 38 EDS elemental mapping of on a polished surface of $Cu_{12}Sb_3TeS_{13}$.

Figure 39 gives the temperature dependence of electronic transport properties for $Cu_{12}Sb_{4-x}Te_xS_{13}$ (x = 0, 0.1, 0.5, 1). Starting at room temperature, the resistivity first decreases with increasing temperature as more carriers are activated by thermal energy. However, when the temperature reaches 500 - 600 K, carrier-phonon scattering begins to dominate, leading to a decreased mobility and thus increased resistivity. On the other hand, upon increasing the Te substitution level from 0.1 to 1, the resistivity doubles from $1.5*10^{-3}$ Ohm*cm to $3.7*10^{-3}$ Ohm*cm at 723 K. Based on our previous study, pure $Cu_{12}Sb_4S_{13}$ is a highly degenerate semiconductor with the Fermi level located below the top of the valence bands. Addition of elements such as Te, Zn, or Fe will introduce more electrons, partially filling the valence bands and reducing the number of available holes. This can be proven by our observation that the resistivity of the x = 1.5 sample reaches $340*10^{-3}$ Ohm*cm at room temperature (not shown in the figure since it is so large), three orders of magnitude larger than that of the x = 1 sample. In this case, we believe all the holes in the valence bands are filled and this sample turns into a typical intrinsic semiconductor with a band gap around 1.7 eV. The Seebeck coefficients are greatly enhanced over the entire temperature region with increasing Te substitution. For example, the highest Seebeck coefficient for the x = 1 sample is 194 μV/K, a 50% enhancement compared to that of pure $Cu_{12}Sb_4S_{13}$. The enhanced Seebeck coefficients originate from moving the Fermi level closer to the top of the valence band manifold, resulting in a reduction in carrier concentration.

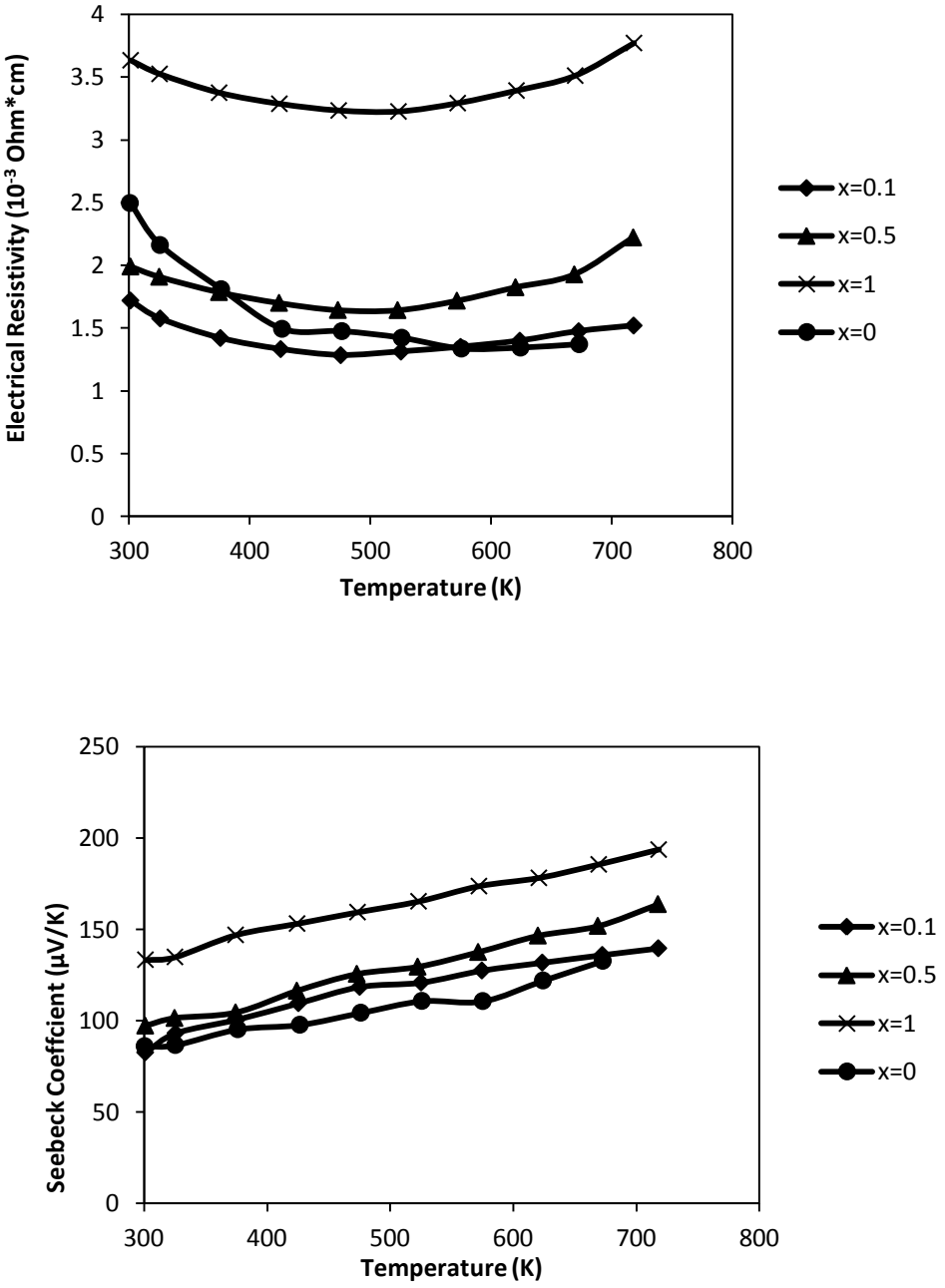

Figure 39 Temperature dependence of the electronic transport properties of $Cu_{12}Sb_{4-x}Te_xS_{13}$ (x = 0.1, 0.5, 1) compounds at high temperature.

The total thermal conductivity is shown in Figure 40. In contrast to traditional thermoelectric materials, in which lattice thermal conductivity is predominant and total thermal conductivity decreases with increasing temperature, the total thermal conductivity of all samples increases with rising temperature. As we mentioned in the previous sections, compounds in the tetrahedrite family display strong anharmonicity and thus intrinsically low lattice thermal conductivity, estimated to be 0.4 - 0.5 W/ m* K. In this case, the dominant part of the thermal conductivity is the electronic portion, which increases with temperature according to the Wiedemann–Franz law. For the x = 1 sample, the total thermal conductivity ranges from 0.64 to 0.77 W/m*K, approximately half that of pure $Cu_{12}Sb_4S_{13}$. The reduction of total thermal conductivity is caused by the decreased electronic thermal conductivity and the substitution effect of Te. The calculated *ZT* values based on our results are displayed in Figure 40. All of the $Cu_{12}Sb_{4-x}Te_xS_{13}$ samples (x = 0.1, 0.5, 1) have dimensionless figure of merit in excess of 0.8 at 723 K and the maximum value we obtain in this study is 0.92 for x = 1 sample. Both thermopower enhancement and reduction in total thermal conductivity contribute to the improved figure of merit but at the expense of increasing electrical resistivity. By adjusting the Te substitution content, the optimal balance between power factor and total thermal conductivity is found to occur at x = 1.

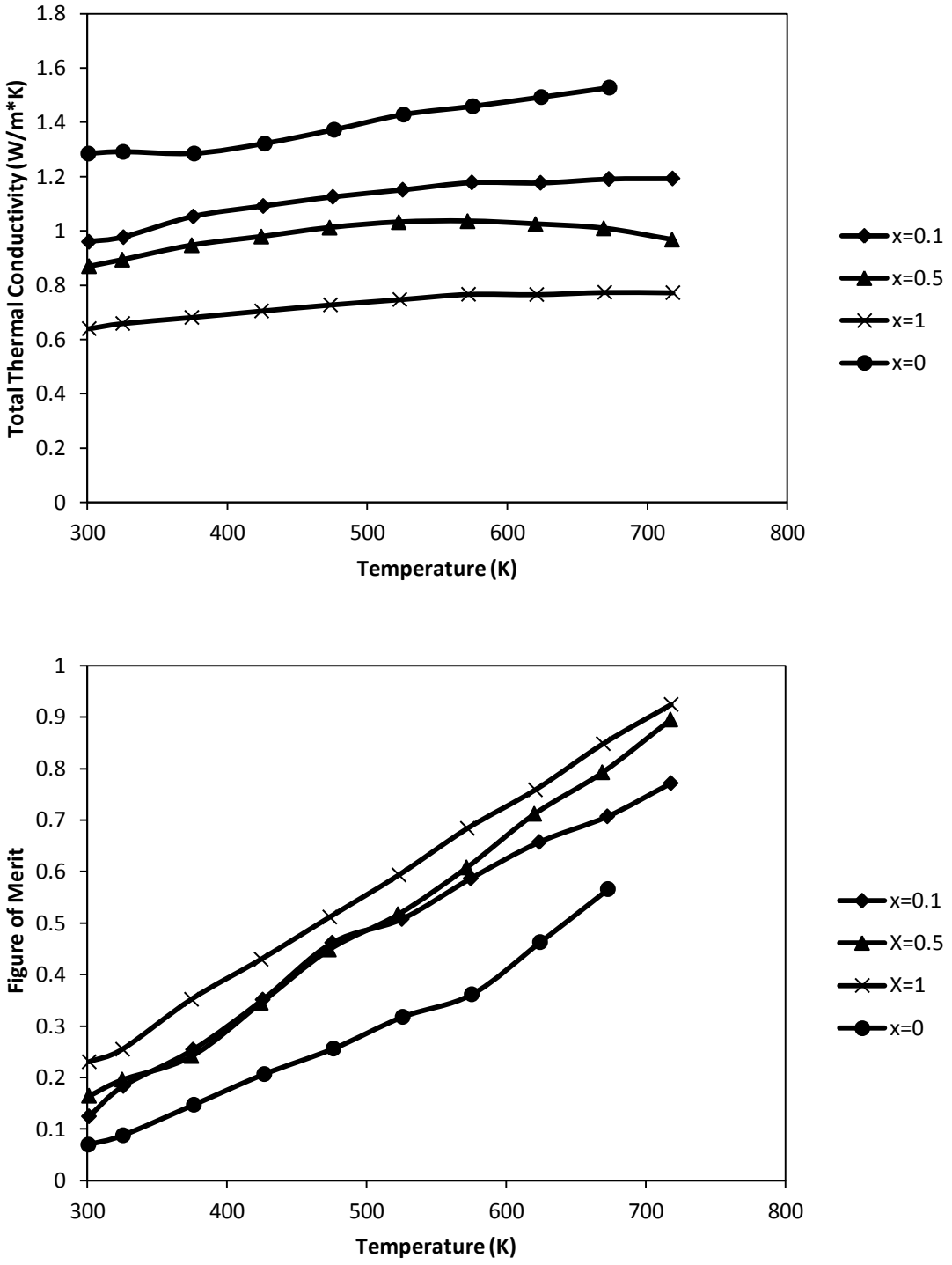

Figure 40 Temperature dependence of total thermal conductivity and figure of merit of $Cu_{12}Sb_{4-x}Te_xS_{13}$ (x = 0.1, 0.5, 1) compounds at high temperature.

In addition, as mentioned above, the $Cu_{12}Sb_{4-x}Te_xS_{13}$ (x = 1.5, 2) and $Cu_{10}Te_4S_{13}$ samples are insulating since most of hole states in valence band are filled by electrons. So these compounds have no electronic part of thermal conductivity. By comparing the thermal conductivity of these samples to that of $Cu_{10}Zn_2Sb_4S_{13}$, we can gain a further understanding of the relationship between lattice thermal conductivity and Te substitution. The data are shown in Figure 41.

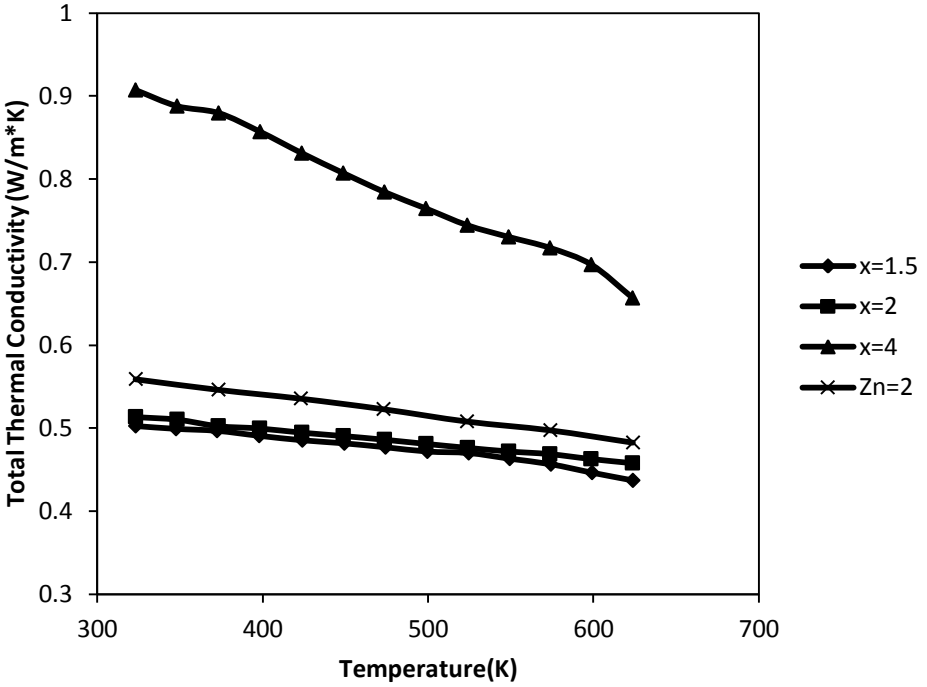

Figure 41 Temperature dependence of total thermal conductivity of $Cu_{12}Sb_{4-x}Te_xS_{13}$ (x = 1.5, 2), $Cu_{10}Te_4S_{13}$ and $Cu_{10}Zn_2Sb_4S_{13}$ compounds at high temperature.

The thermal conductivities of $Cu_{12}Sb_{4-x}Te_xS_{13}$ (x = 1.5, 2) are slightly smaller than that of $Cu_{10}Zn_2Sb_4S_{13}$ due to stronger alloy scattering introduced by Te substitution. The thermal conductivity curves of these three samples are flat, a typical phenomenon for compound with

intrinsic low thermal conductivity at high temperature. In contrast, the thermal conductivity of $Cu_{10}Te_4S_{13}$, which has more substituted Te atoms, is in the range of 0.7 - 0.9 W/m*K, two times larger than that of $Cu_{10}Zn_2Sb_4S_{13}$ and decreases with temperature noticeably. The drastic change in thermal conductivity for $Cu_{10}Te_4S_{13}$ results from the crystal structure difference. In the original tetrahedrite structure, the buckling of the triangularly-coordinated Cu atoms are proved to be the origin of intrinsic low thermal conductivity. In the end member goldfieldite ($Cu_{10}Te_4S_{13}$), two of the triangularly-coordinated Cu atoms sites are vacant in order to balance the charge resulting from the replacement of trivalent Sb by tetravalent Te. The absence of two out of six triangularly-coordinated Cu atoms will cause a reduction in the strength of anharmonicity and therefore $Cu_{10}Te_4S_{13}$ loses part of its intrinsic low thermal conductivity character. This is another proof for the importance of triangularly-coordinated Cu in the low thermal conductivity found in tetrahedrite structure.

In summary, we successfully synthesized and studied the thermoelectric properties of $Cu_{12}Sb_{4-x}Te_xS_{13}$ (x = 0.1, 0.5, 1, 1.5, 2) and $Cu_{10}Te_4S_{13}$ compounds. The first four compositions have enhanced thermoelectric performance compared to pure $Cu_{12}Sb_4S_{13}$ compounds. The highest *ZT* value obtained in this study is 0.92 at 723 K for x = 1 sample, comparable to other p-type thermoelectric materials at this temperature range. Te substitution can thus be considered as an effective way to enhance the thermoelectric performance of tetrahedrites. It is worth noting that at the optimum composition the Te concentration in these compounds amounts to only 3.4 atomic percent, so this type of substitution should have minimal impact on the cost effectiveness of these materials.

4.5 Summary of the chapter

We systematically studied the substitution effects of Zn, Fe for Cu and Te for Sb in $Cu_{12}Sb_4S_{13}$ on the thermoelectric properties. All three substitution types will introduce additional electrons into the compound, filling the hole states in valence band. This gives rise to increase in both electrical resistivity and the Seebeck coefficient. In most cases, the substitutions of alien atoms cause reduction in power factor but overall *ZT* values are enhanced by a large decrease in total thermal conductivity due to smaller electronic contribution. In a wide range of alien atoms (Zn, Fe, Te) substitution, high *ZT* values above 0.6 can be maintained, which means the thermoelectric properties of these compound are insensitive to impurity levels and quite suitable for large-scale production.

Chapter 5 Enhancement of Figure of Merit of Tetrahedrite by Co-doping

In the work described in the previous chapters, the earth-abundant natural mineral-based tetrahedrite compound family, substituted with Zn, Fe and Te, has been found to display high performance thermoelectric properties. The highest *ZT* values of Zn and Te substituted compound reported is approximately 0.9. However, the enhancement of figure of merit is at the expense of reduction in power factor. In this chapter, we will show that enhancement in *ZT* values while maintaining power factor can be achieved by careful Ni and Zn co-doping. Through manipulation of the position of the Fermi level near top of valence band, a maximum *ZT* value over unity is attained.

5.1 Theoretical background of Ni and Zn co-doping for tetrahedrite

For semiconductor materials, adding two or more elements into a parent compound to improve its performance is called co-doping. The co-doping technique has been proved successful in different TE materials systems, such as Mg_2Si and PbTe [84, 85]. It helps to adjust both the electronic structure and the phonon transport at the same time, leading to enhancement in figure of merit for TE materials. More often than not, the added two doping elements have different effects on the properties of the parent compound.

Both experimental and theoretical results show that Zn and Ni doping have different effects on the electronic structure of these compounds. Since undoped $Cu_{12}Sb_4S_{13}$ is a metal-like heavily doped p-type semiconductor with the Fermi level below the top of the valence bands, Zn doping

provides extra electrons to fill the holes in valence the band, moving the Fermi level into the energy gap, which is approximately 1.7 eV. Since undoped $Cu_{12}Sb_4S_{13}$ has two empty hole states per formula unit, $Cu_{10}Zn_2Sb_4S_{13}$ is almost insulating, but for Zn substitutions ≤ 2 the properties may be tuned to provide for large *ZT*. On the other hand, Ni doped tetrahedrites are still conducting at x = 2 and achieve their highest *ZT* at x = 1.5 [76]. In order to understand the different effects of Zn and Ni doping, DFT calculation was employed by our UCLA collaborators to perform structural relaxations and to give information about electronic band structures and densities of states. Structures for $Cu_{11}NiSb_4S_{13}$ and $Cu_{10}Ni_2Sb_4S_{13}$ were obtained via picking the lowest-energy configuration among all symmetry-inequivalent substitutions on Cu sites after fully relaxing all structural degrees of freedom. Relaxation was stopped when all forces were below 0.02 eV/Å. It was found that tetrahedral 12*d* sites are preferred energetically. Band structures were calculated along high symmetry lines in reciprocal space of the body-centered cubic lattice for both majority spin and minority spin states. The calculated results of electronic structure for $Cu_{11}NiSb_4S_{13}$ and $Cu_{10}Ni_2Sb_4S_{13}$ are shown in Figure 42.

The electronic structure of Zn substituted tetrahedrite is given in Chapter 4. The addition of Zn will fill the hole states in the valence band, moving the Fermi level into the energy gap. The behavior with Ni doping, however, is quite different. For $Cu_{11}NiSb_4S_{13}$ we assume a ferromagnetic (FM) configuration rather than an antiferromagnetic configuration since our calculations predict that the antiferromagnetic (AF) spin alignment is 0.1 eV higher in energy than FM. As the Ni 3*d* states are only slightly higher in energy than the Cu 3*d* states, it can be expected that they will strongly hybridize with the valence bands of the host. The majority spin e_g and t_{2g} states of Ni indeed lie in the same energy range as the Cu 3*d* states and are fully occupied (upper left panel of Figure 42).

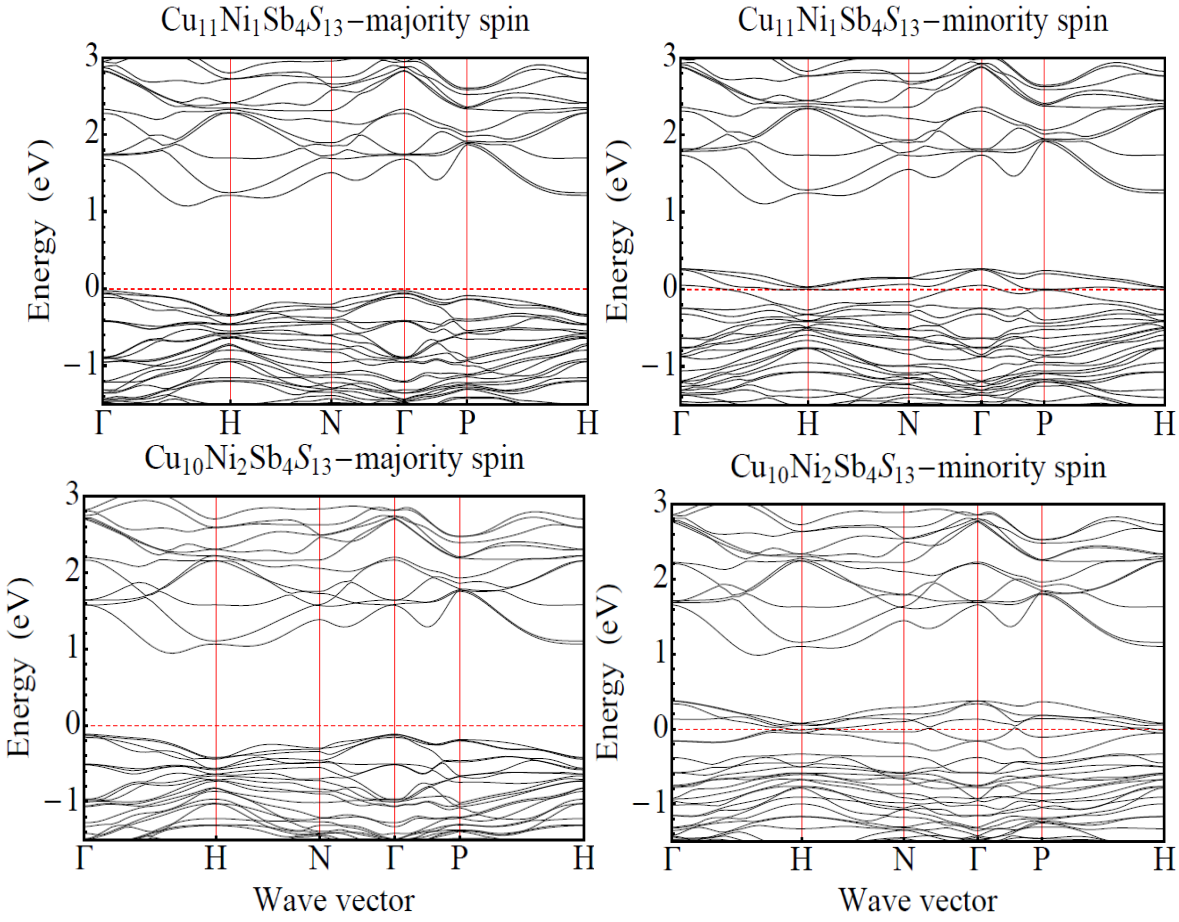

Figure 42 Calculated electronic structure of $Cu_{11}NiSb_4S_{13}$ and $Cu_{10}Ni_2Sb_4S_{13}$.

In the minority spin channel, however, three partially empty acceptor-like bands exist above the Fermi level (upper right panel of Figure 42), but these bands overlap with the filled valence bands of the host and there is a finite DOS at the Fermi level. The total spin is found to be 3/2 per formula unit of $Cu_{11}NiSb_4S_{13}$, giving S(S+1) = 3.75 in good agreement with the effective magnetization values of 3.6 deduced from magnetic susceptibility measurements by Suekuni et

al. [86]. The results for the double-substituted $Cu_{10}Ni_2Sb_4S_{13}$ compound in Figure 42 (lower panel) show that the band structures of $Cu_{11}NiSb_4S_{13}$ and $Cu_{10}Ni_2Sb_4S_{13}$ differ by the existence of an additional partially empty minority spin band at the Fermi level, giving a total spin S = 2.

Analysis of the partial DOS curves of the Ni-substituted compounds (Figure 43) shows that the partially empty bands are formed by hybridizing Ni 3*d* states with the *p-d* hybridized valence bands of the host. Since the number of holes per formula unit varies from 2 for the pure compound (x = 0), to 3 for x = 1, and to 4 for x = 2, this suggests that each substitutional Ni introduces an additional hole state into the VB of the host. At all Ni concentrations considered, the resulting band structure remains metallic, in agreement with the experimental results of Suekuni *et al*.on Ni-doped tetrahedrite [76]. Here we hypothesize that further optimization of Ni-doped tetrahedrite may be achieved by re-adjusting the Fermi level close to the top edge of the valence band by addition of Zn and filling the holes introduced by Ni substitution.

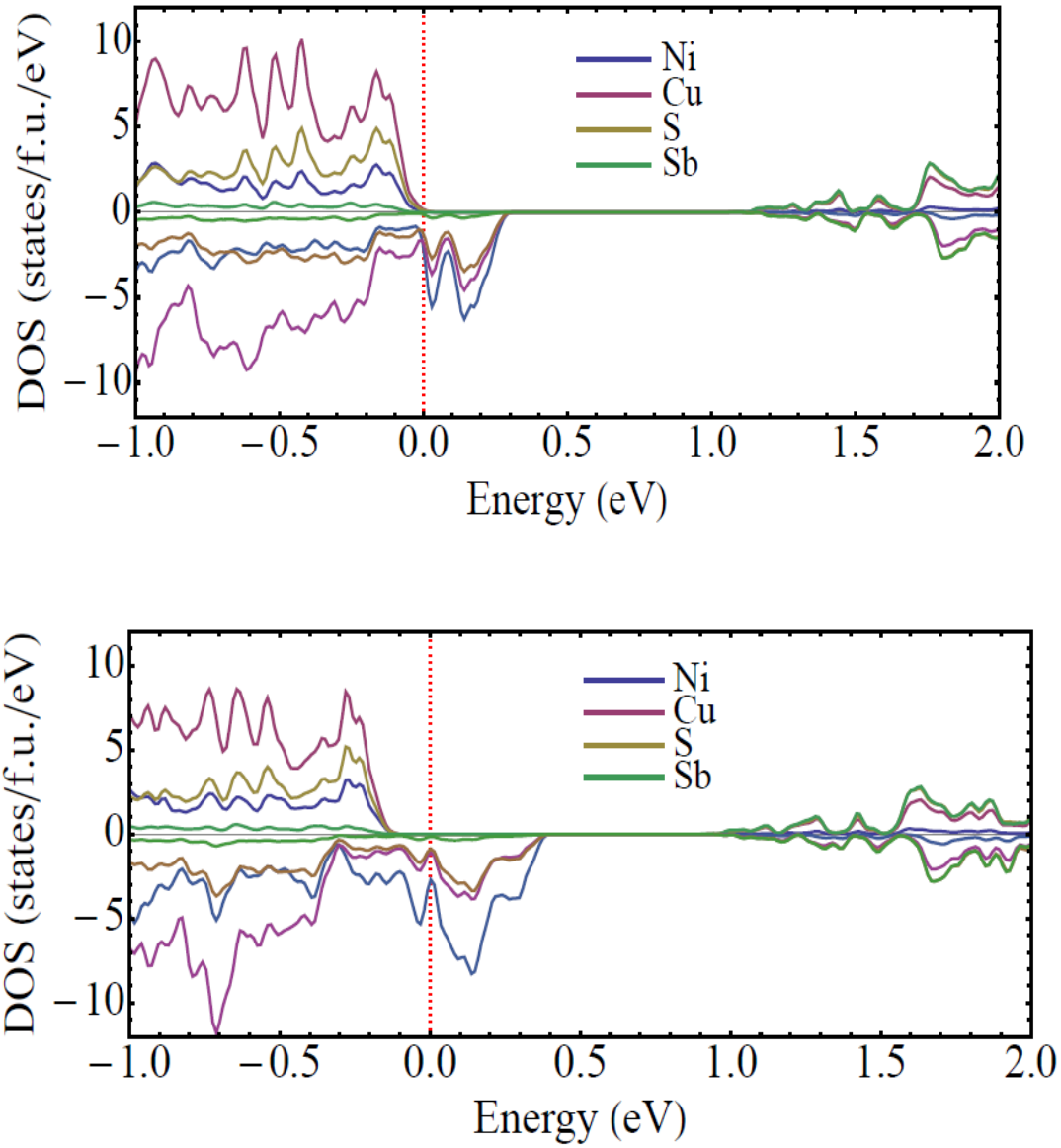

Figure 43 Calculated partial electron density of states of $Cu_{11}NiSb_4S_{13}$ (top) and $Cu_{10}Ni_2Sb_4S_{13}$ (bottom).

5.2 Thermoelectric properties of Ni and Zn co-doping tetrahedrite

In order to test the argument given above, we begin with a Ni doping level yielding the highest *ZT* $Cu_{10.5}Ni_{1.5}Sb_4S_{13}$, and progressively substitute Zn for Ni. $Cu_{10.5}Ni_{1.5-x}Zn_xSb_4S_{13}$ (x = 0, 0.2 0.5, and 1) samples were synthesized following the same routine used for other single doping tetrahedrite samples. Figure 44 shows the temperature dependence of the electronic transport properties of $Cu_{10.5}Ni_{1.5-x}Zn_xSb_4S_{13}$ (x = 0, 0.2 0.5, and 1). As shown in the upper left panel, the electrical resistivity of these samples decreases weakly until the mid-temperature region, and then rises at higher temperature. This behavior is consistent with a highly degenerate semiconductor or weakly metallic system with low carrier mobility. The same behavior has been observed in Zn-doped samples. For the x = 0 sample ($Cu_{10.5}Ni_{1.5}Sb_4S_{13}$), the resistivity at 723 K is $4.1*10^{-3}$ Ohm*cm, much lower than that of $Cu_{10.5}Zn_{1.5}Sb_4S_{13}$, which has a resistivity of $1.2*10^{-2}$ Ohm*cm. This can be explained by the spin splitting of the Ni t_{2g} states as discussed above for Figure 42. After adding a small amount of Zn (x = 0.2 and 0.5) into $Cu_{10.5}Ni_{1.5}Sb_4S_{13}$, the resistivities are increased by 6% and 30%, respectively. At x = 1, the resistivity becomes two times larger than that of the x = 0 sample. The additional electrons from Zn fill the holes in the valence band, moving the Fermi level closer to the top of the valence band and decreasing the carrier density. In order to tune the Seebeck coefficient, the optimum position of the Fermi level should be close to the band edge where a large energy dependence of the electronic DOS can be obtained. The upper right panel of Figure 44 displays the temperature dependence of Seebeck coefficients: for the three co-doped samples, the Seebeck coefficients are all increased, as we expect.

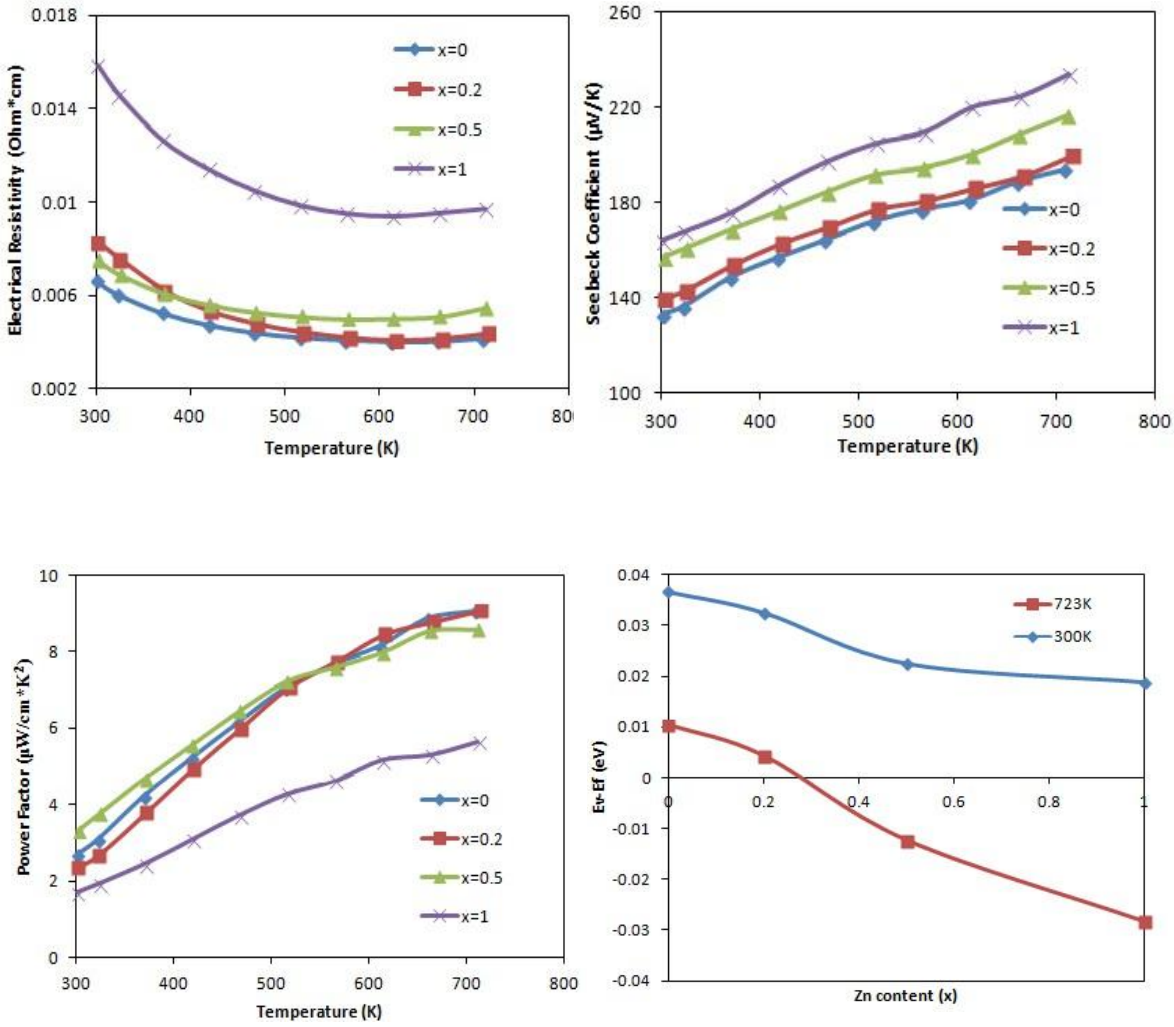

Figure 44 Temperature dependence of electronic transport properties of $Cu_{10.5}Ni_{1.5-x}Zn_xSb_4S_{13}$(x = 0, 0.2 0.5, 1) compounds .

In order to determine the optimal position of the Fermi level, we estimated the reduced Fermi energy by using a single parabolic band model with acoustic phonon scattering as the predominant scattering mechanism through equation 30. The calculated energy difference between the top of the valence band and the Fermi energy in units of eV is shown in the lower left panel of Figure 44 as a function of Zn content for two temperatures. The Fermi energy moves closer to the top of the valence band with increasing Zn content, and at high temperatures even moves slightly into the gap. The power factor for all samples is displayed in lower right panel of Figure 44. Due to the enhancement in Seebeck coefficients, the power factors of the x = 0.2 and x = 0.5 samples are changed hardly at all although their resistivities increase during Zn co-doping.

Figure 45 (top left panel) shows the total thermal conductivity as a function of temperature for all $Cu_{10.5}Ni_{1.5-x}Zn_xSb_4S_{13}$ samples (x = 0, 0.2 0.5, 1) together with pure $Cu_{12}Sb_4S_{13}$ and $Cu_{10}Zn_2Sb_4S_{13}$ for comparison. The total thermal conductivity of all samples increases with increasing temperature due to an increased electronic contribution – with the exception of $Cu_{10}Zn_2Sb_4S_{13}$, which is almost insulating and thus has a negligible electronic contribution. Pure $Cu_{12}Sb_4S_{13}$ has a total thermal conductivity in the range of 1.2 W/m*K to 1.5 W/m K from room temperature to high temperature, while the total thermal conductivities of all the other samples are below 0.8 W/m*K due to reduction in both electronic and lattice contributions. In order to clarify the effect of Ni and Zn co-doping on the lattice thermal conductivity, we subtract the electronic thermal conductivity obtained by applying Wiedemann-Franz law from total thermal conductivity. The Lorenz numbers (shown in Figure 45 top right panel) are calculated using the equation 37 and employing the reduced Fermi energy values found previously from the Seebeck data [87].

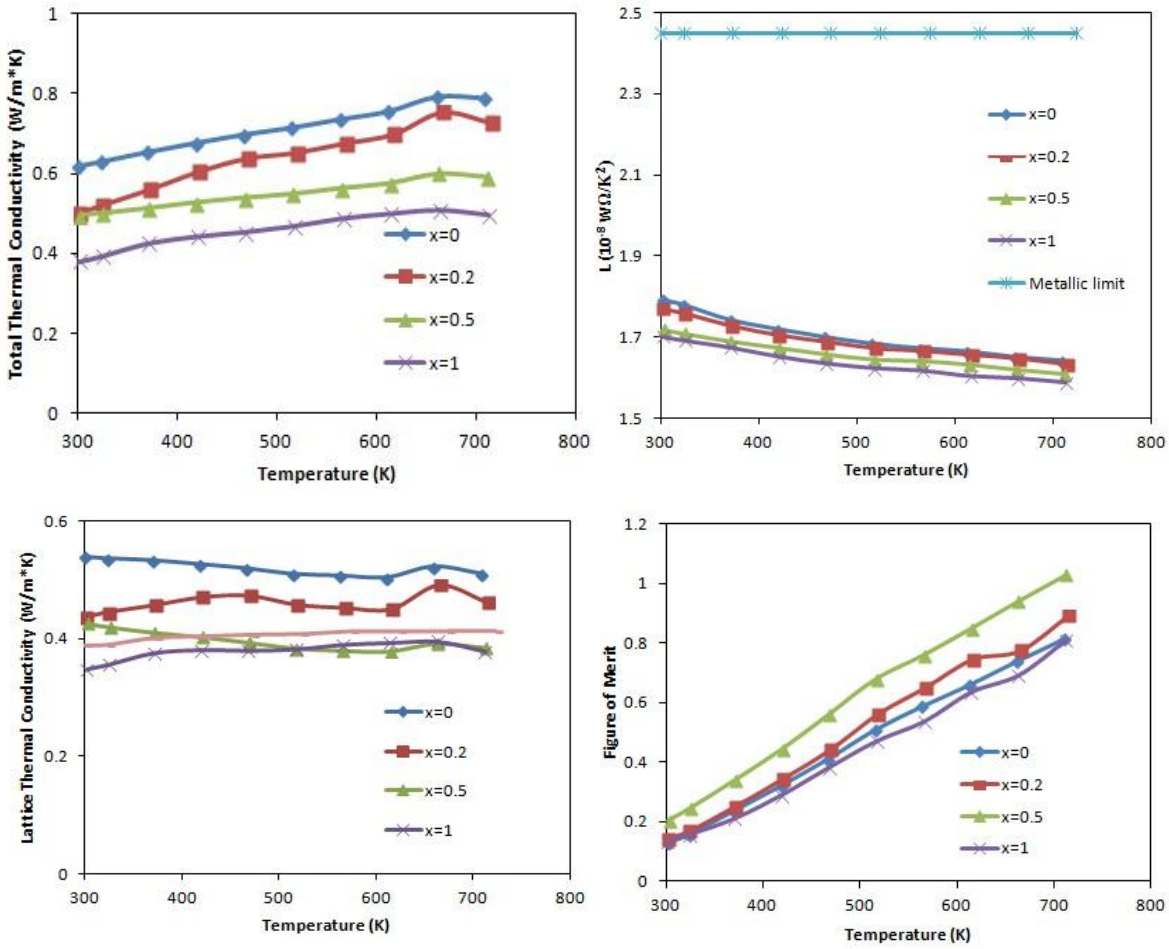

Figure 45 Temperature dependence of total thermal conductivity, Lorenz numbers, lattice thermal conductivity and figure of merit of $Cu_{10.5}Ni_{1.5-x}Zn_xSb_4S_{13}$ (x = 0, 0.2 0.5, 1) compounds.

The calculated Lorenz numbers for all co-doped samples are in the range of $1.8*10^{-8}$ to $1.6*10^{-8}$ $W*\Omega/K^2$ from room temperature to high temperature, significantly lower than the metallic limit of 2.45×10^{-8} $W*\Omega/K^2$. Using these calculated Lorenz numbers, we determine the lattice thermal conductivity by subtracting the electronic contribution from the total: the results are shown in the lower left panel of Figure 45. The theoretical minimum lattice thermal

conductivity estimated by formula $k_{min} = \frac{1}{3} C_v v l$ is also shown as brown line. For the latter estimate we use the specific heat C_v data obtained from our experiments and a mean sound velocity $v = 2500\ \mathrm{m/s}$ estimated from elastic properties measurements. For the phonon mean free path we use the interatomic distance *l* = 0.226 nm. The lattice thermal conductivity of pure $Cu_{12}Sb_4S_{13}$ decreases from 1.0 W/m*K to 0.6 W/m*K with increasing temperature, following a 1/T law, where the phonon mean free path exceeds the interatomic distance. Therefore, the lattice thermal conductivity of pure $Cu_{12}Sb_4S_{13}$ is close to but still above the theoretical minimum value of about 0.4 W/m*K. As pointed out previously, the anharmonicity in the tetrahedrite structure leads to the intrinsic low thermal conductivity. Here, we find that the dopant atoms (Ni and Zn) replacing Cu atoms in tetrahedrites further decrease the lattice thermal conductivity through solid solution point defect phonon scattering, pushing the lattice thermal conductivity down close to theoretical minimum. The lattice thermal conductivity of all the doped samples is temperature independent throughout the measured temperature range. The single element doped sample, $Cu_{10}Zn_2Sb_4S_{13}$ in which both of the two available Cu atoms are replaced by Zn atoms, exhibits a lattice thermal conductivity of 0.45 W/m*K.

By combining the electronic transport and thermal conductivity data, the overall figure of merit is computed, and the results are shown in the lower panel of Figure 45. By addition of Zn to $Cu_{10.5}Ni_{1.5}Sb_4S_{13}$, *ZT* can be enhanced from 0.81 to 0.99 and 1.03 for x = 0.2 and x = 0.5, respectively.

5.3 Summary of the chapter

In summary, with optimum Fermi energy level and minimum lattice thermal conductivity by Zn and Ni co-doping for $Cu_{10.5}Ni_{1.5-x}Zn_xSb_4S_{13}$ (x = 0, 0.2, 0.5, 1) tetrahedrites, the *ZT* value of x = 0.5 sample is over unity at 723 K, which is among the best p-type TE materials in this temperature region. Considering the low cost and earth abundant elements in tetrahedrites, this class of materials should be a good candidate for large scale thermoelectric applications.

Chapter 6 Synthesis of TE Materials Directly from Natural Mineral Tetrahedrite

In traditional thermoelectric materials synthesis, researchers purchase pure elements extracted from natural minerals and combine these elements into compounds with highly controlled chemical stoichiometry by heating or mechanical alloying in vacuum or inert atmosphere. In addition, careful doping, band structure engineering or nanostructuring are required to achieve higher figure of merit. In these procedures, more energy and human labor are used, largely reducing efficiency/cost ratio for TE materials, which impedes the large-scale application of TE materials. In this chapter, we will discuss the methods of directly using natural mineral tetrahedrite as raw source (at least 50 weight percent) for synthesis of TE materials [88].

6.1 Synthesis of TE materials by natural mineral/synthetic powder solid solution

One advantage of tetrahedrite based TE materials is that they already possess intrinsic low lattice thermal conductivity due to strong anharmonicity. Therefore, no further work is required to reduce thermal conductivity. Another advantage found in this system is the fact that the figure of merit is not sensitive to the impurity concentration but rather is related to the hole filling fraction in the valence band. The wide range of hole filling fraction also allows for a wide range of impurity concentrations in these materials. Natural minerals often have a wide range of element content variation. The results on synthetic tetrahedrites suggest that many natural minerals may possess compositions that are in the range of optimal thermoelectric performance, and therefore may be used directly as source TE material.

As source materials for synthesis of our samples, two natural mineral specimens, here designated Natural Mineral 1 (NM1) and Natural Mineral 2 (NM2), were purchased from a mineral specimen company [89]. In order to obtain compositional information on these two specimens, we performed energy-dispersive X-ray analysis using a SEM 7500F. Based on the results, the compositions of NM1 and NM2 are approximately $Cu_{10.5}Fe_{1.5}As_{3.6}Sb_{0.4}S_{13}$ and $Cu_{9.7}Zn_{1.9}Fe_{0.4}As_4S_{13}$ respectively. Like all minerals given the geological tetrahedrite designation, these two specimens are solid solutions of pure tetrahedrite ($Cu_{12}Sb_4S_{13}$, which does not occur naturally) and tennantite ($Cu_{12}As_4S_{13}$), with substitution of Zn or Fe on the copper site. Unfortunately, the hole filling fractions of the two specimens are much higher than the fraction expected to give rise to high *ZT*, which means we cannot directly use these two specimens as TE materials without any adjustment of the composition. Therefore, a simple method of "diluting" these rocks into the right hole filling fraction region was developed by mixing small amounts of pure synthetic $Cu_{12}Sb_4S_{13}$ with the natural mineral to form a solid solution within the desired composition range.

The powders of pure synthetic $Cu_{12}Sb_4S_{13}$ we obtained using the approach described in Chapter 2 were mixed with natural mineral powders in a stainless balling milling vial with stainless steel balls in mass ratio of 1:3, 1:1 and 3:1. The vial was sealed in an argon-filled glove box and the powder mixture was milled for 30 min. The fine powder after the ball milling was consolidated by a standard hot pressing procedure and all the final pellets were found to be greater than 98% of theoretical density.

The powder XRD patterns of NM2, pure $Cu_{12}Sb_4S_{13}$ and a (1:1) mixture of the two are shown in Figure 46. All of the major diffraction peaks match to the pattern of tennantite ($Cu_{12}AsS_{13}$) /tetrahedrite ($Cu_{12}Sb_4S_{13}$), with only a peak shift observable. As we can see, the

pattern of mixture has no sign of any second phase and its peaks are located between the two pure phases. Therefore, we can claim that the simple dilution method can give rise to perfect solid solutions between the pure synthetic sample and the natural mineral without changing the crystal structure, which is crucial to maintaining the intrinsic low thermal conductivity.

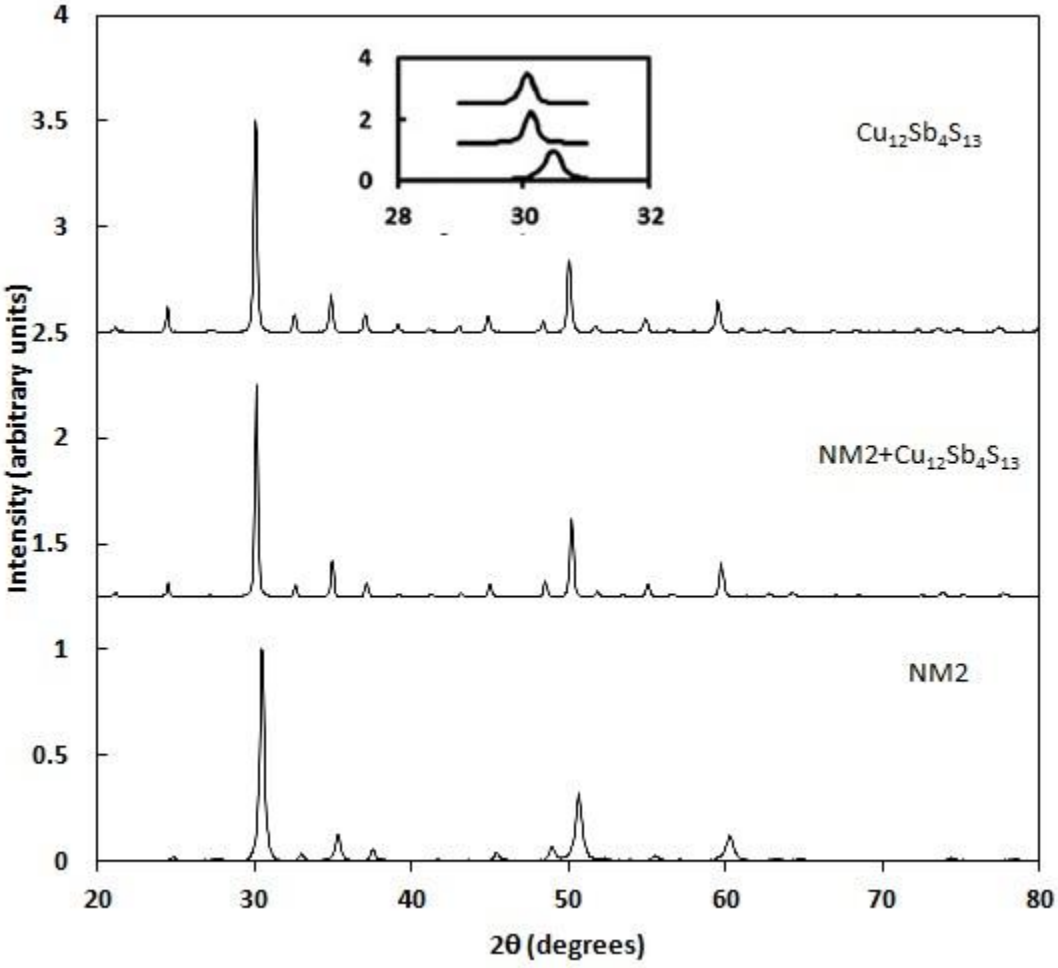

Figure 46 X-ray diffraction patterns for tetrahedrite samples.
The inset shows detail near 2θ = 30°.

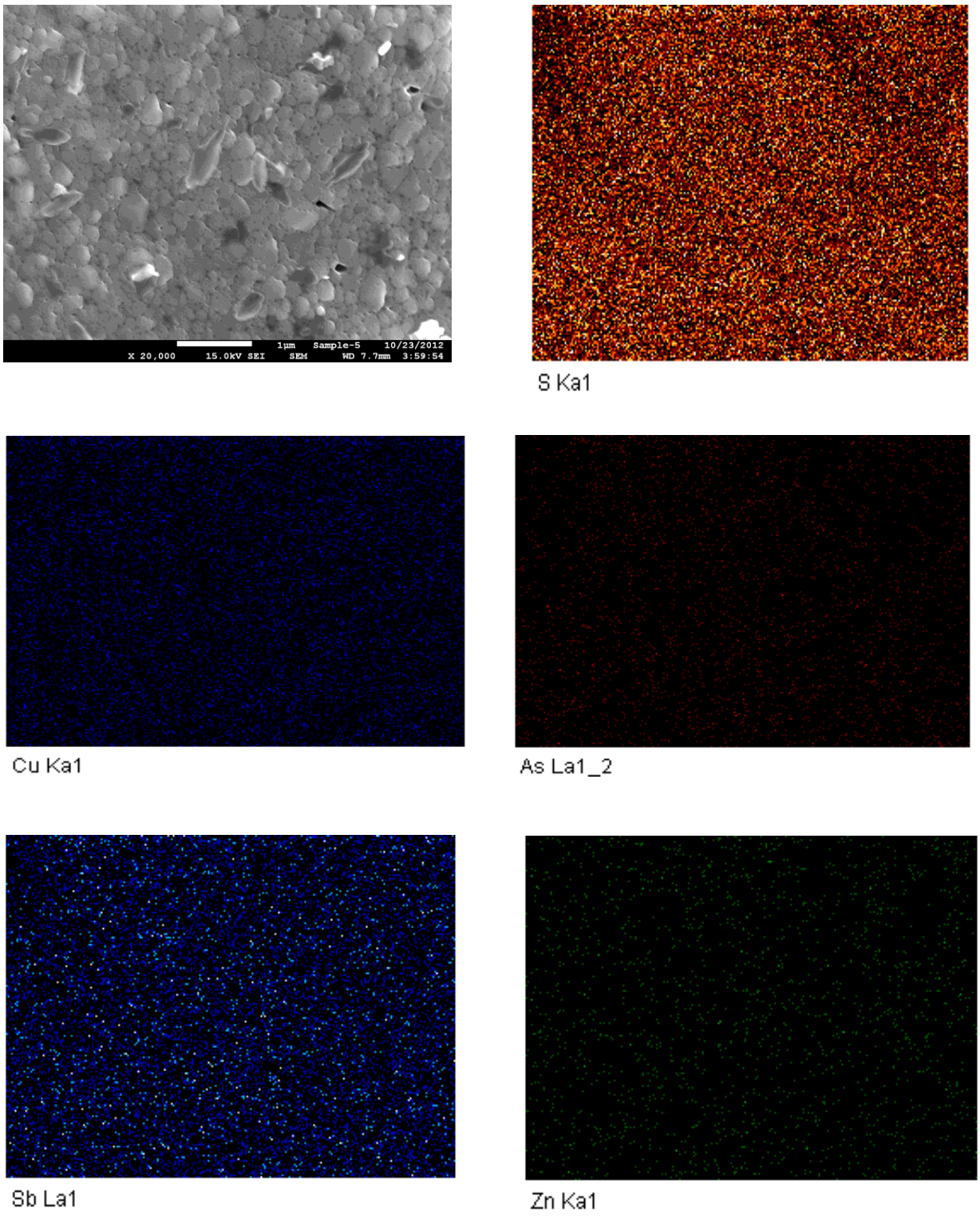

Figure 47 Scanning electron microscope (SEM) images and EDS element mapping for a hot-pressed (1:1) NM2/$Cu_{12}Sb_4S_{13}$ sample.

Figure 47 shows SEM images of the (1:1) NM2/$Cu_{12}Sb_4S_{13}$ mixture after hot pressing. The SEM image on the fracture surface reveals grain size of in the range of 100nm - 500nm. The small grain size was induced during the balling milling process, and is largely maintained throughout the hot pressing procedure, which is carried out at relatively low temperature. Although the tetrahedrites have very low intrinsic thermal conductivity, additional phonon scattering from grain boundaries may also contribute to the low thermal conductivity. Electron Dispersive X-ray (EDX) analysis performed on the same area of the SEM image shows that all the major elements in the mixture are homogeneously distributed throughout the sample, which also provides further evidence for the formation of a perfect solid solution between the natural mineral and pure $Cu_{12}Sb_4S_{13}$.

The electrical transport properties of all the NM1 and NM2 mixture samples are shown in Figure 48. The simplified notations are used to describe the compositions of mixtures. The designation "NM1+25%" means the mixture made with a combination of natural mineral (75 wt%) and synthetic pure $Cu_{12}Sb_4S_{13}$ (25 wt%). As can be seen from Figure 48, almost all of the samples show a semiconducting behavior over the temperature range studied, and as the amount of pure $Cu_{12}Sb_4S_{13}$ increases, the resistivity of the mixture decreases rapidly. Compared to pure natural mineral samples (not shown in the plots), the resistivity decreases by more than three orders of magnitude. As was mentioned previously, Fe ions in the tetrahedrite system (nominally trivalent Fe^{3+}) provide one additional electron compared to divalent Zn ions; thus NM1 is more insulating than NM2, as more holes in the valence band have been filled by electrons. This means that more of the pure compound must be added to NM1 in order to "dilute" it into the optimal range. By adding 75% pure $Cu_{12}Sb_4S_{13}$ into NM2, the mixture shows a metal-like resistivity temperature dependence.

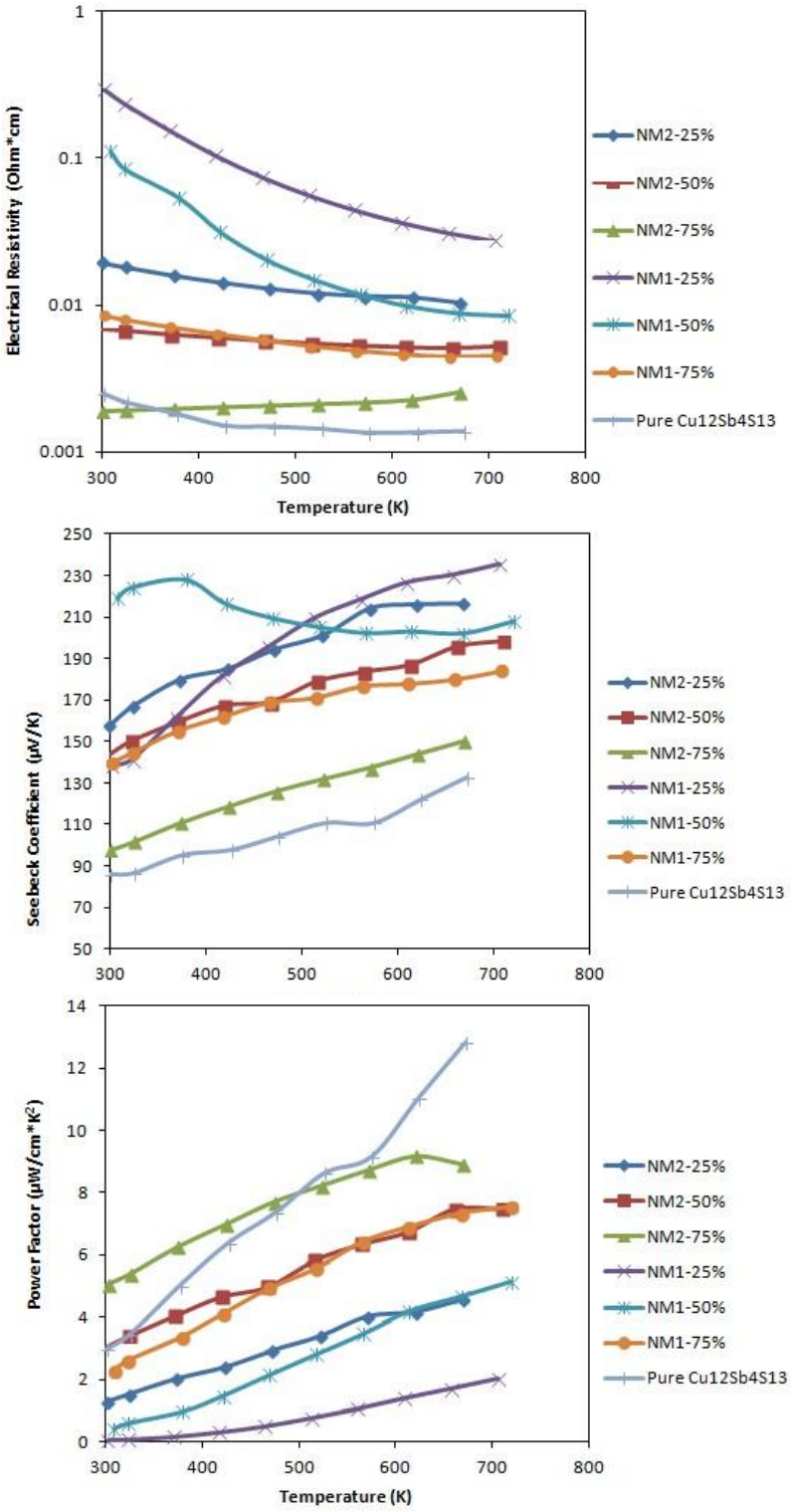

Figure 48 Temperature dependence of electronic transport properties of tetrahedrite-based samples, made by hot pressing mixtures of natural mineral (NM1 or NM2) and synthetic tetrahedrite.

Figure 48 also displays the dependence of the Seebeck coefficients on the amount of pure $Cu_{12}Sb_4S_{13}$ addition. As we expect, Seebeck coefficients are depressed by mixing, since the mixtures become more and more metallic. However, the Seebeck coefficients of all mixtures remain above 150 μV/K at 723 K. The overall power factor is greatly enhanced by addition of pure $Cu_{12}Sb_4S_{13}$ (the power factor of both natural mineral specimens are below 1 μW/cm*K^2).

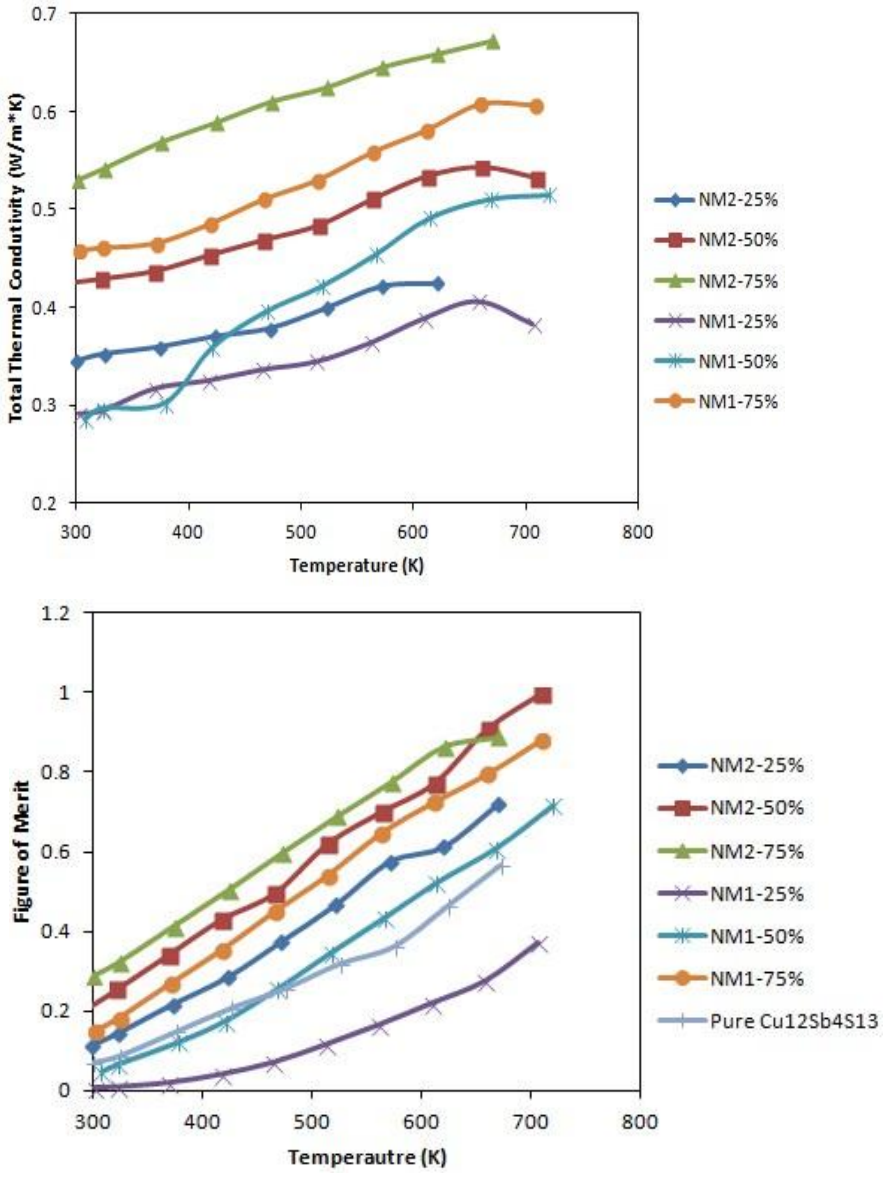

Figure 49 Temperature dependence of total thermal conductivity and figure of merit of tetrahedrite based samples, made by hot pressing mixtures of natural mineral (NM1 or NM2) and synthetic tetrahedrite.

The total thermal conductivity of all samples is displayed in Figure 49. Compared to pure $Cu_{12}Sb_4S_{13}$ with thermal conductivity of 1.5 W/m*K at 723 K, all the mixture samples have thermal conductivity below 0.7 W/m*K. With increasing temperature, the electronic part of thermal conductivity becomes dominant. The lattice thermal conductivity becomes even lower than that of their synthetic counterparts. This is a combined effect from large anharmonicity, Sb-As mass-fluctuation scattering and small grain size. We calculated the *ZT* values based the transport and thermal properties above, and the results are shown in Figure 49. For sample NM1, the *ZT* continuously increases with increasing content of pure $Cu_{12}Sb_4S_{13}$ and the highest *ZT* is 0.8 for NM1-75%, while for NM2, the highest $ZT \approx 1$ was obtained at moderate addition of 50% pure $Cu_{12}Sb_4S_{13}$. Interestingly, the samples with higher power factor do not necessarily have higher *ZT*. For example, NM2-75% has a power factor of 9 $\mu W/cm*K^2$, larger than that of NM2-50%. However, NM2-75% has higher thermal conductivity than that of NM2-50% since the electronic thermal conductivity dominates. The sample gains a benefit from the decrease in resistivity but also suffers a penalty from electronic thermal conductivity. There is a balance between power factor and thermal conductivity to get high *ZT*. From the empirical model we obtained from the Zn and Fe doped synthetic samples, when the hole filling fraction in valence band is near 0.5, maximum *ZT* can be achieved. Estimated by the hole filling model, the hole filling fraction of NM1-75% and NM2-50% are 0.4 and 0.6, respectively . Therefore, *ZT* data from this study agrees very well with this simple picture.

In conclusion, we have shown that randomly chosen natural tetrahedrite minerals can be used directly as raw material to synthesize TE materials. By mixing as prepared pure $Cu_{12}Sb_4S_{13}$ with natural mineral through ball milling and hot pressing, a maximum *ZT* value of 1 was obtained at 723 K, which is comparable to other p-type TE materials at this temperature. Zn

atoms are more preferable than Fe atoms for TE materials application in this system. Unlike traditional TE materials synthesis, in which pure elements extracted from minerals with great energy, effort, and cost are carefully combined to obtain compounds with exact chemical stoichiometry, in this study we synthesize TE materials with at least 50% of natural mineral as the source. Furthermore, the family of tetrahedrite/tennantite minerals, a chief copper ore, is among the most widespread in the world. It is highly probable that one can find natural minerals with suitable composition (and corresponding hole filling fraction) that can be directly consolidated into usable forms with little effort and energy. The use of natural minerals as low cost, abundant, and chemically stable TE materials is a new paradigm in the field and can help pave the way for the large scale application of thermoelectrics.

6.2 Rapid synthesis of TE materials from natural mineral by high energy ball milling

As discussed in previous section. Mixing natural mineral tetrahedrite and pure synthetic $Cu_{12}Sb_4S_{13}$ can make TE materials with maximum *ZT* close to unity. However, the processing of synthetic $Cu_{12}Sb_4S_{13}$, used to optimize the composition of the natural mineral, employs a traditional solid state reaction followed by at least one week anneal, which still requires significant energy and time.

High energy ball milling has been used as an efficient method to synthesize TE materials at fully scalable quantities from a few grams to kilograms in a few hours, especially for simple binary compounds such as $Si_{1-x}Ge_x$ alloy [24] and Bi_2Te_3 [33]. But for more complex systems, high energy ball milling synthesis often requires additional heat treatments [90] or gives rise to noticeable second phase [91]. In this section, we present a rapid method of synthesizing

tetrahedrite TE material by high energy ball milling [92]. A total mass around 2 g of elemental Cu (powder, 10 micron, 99.9%), Sb (shot, 99.999%), and S (pieces, 99.999%) from Alfa Aesar were weighed by stoichiometry of $Cu_{12}Sb_4S_{13}$ and loaded into a tungsten carbide vial with tungsten carbide balls. Subsequently, the raw natural mineral with composition of $Cu_{9.7}Zn_{1.9}Fe_{0.4}As_4S_{13}$ as determined by EDS was weighed with the mass ratio of 3:1 and 1:1 (compared to the mass of mixture of the elements described above), ground into a powder using mortar and pestle, and then loaded into the same vial. The vial was sealed under argon and then placed into a SPEX 8000M (SPEX SamplePrep) ball mill for high energy ball milling. Milling times of one, three, and six hours were performed to investigate the effect of milling time on the phase formation and grain size. The product powers were consolidated by hot pressing procedure used before.

X-ray diffraction (XRD) patterns of samples made by mixing 50% by weight natural mineral (nominal composition $Cu_{9.7}Zn_{1.9}Fe_{0.4}As_4S_{13}$) with Cu, Sb, and S powders (the latter in a molar ratio of 12:4:13), as a function of ball milling time, are displayed in Figure 50. Also shown in this Figure 50, for comparison, are the patterns for pure synthetic $Cu_{12}Sb_4S_{13}$ and the pure natural mineral. The latter two samples exhibit a single phase pattern corresponding to the tetrahedrite (or tennantite) crystal structure; the peaks are shifted in these two samples primarily due to the different atom on the pnictide site.

Peaks corresponding to the tetrahedrite structure for the ball milled samples lie between the patterns of pure synthetic $Cu_{12}Sb_4S_{13}$ and pure natural mineral, indicating good mechanical alloying effect. For the sample milled for one hour, a noticeable pattern of Cu_3SbS_4 (famantite) phase was observed. As we describe below, this phase forms readily when Cu, Sb, and S are ball milled together alone without the natural mineral present.

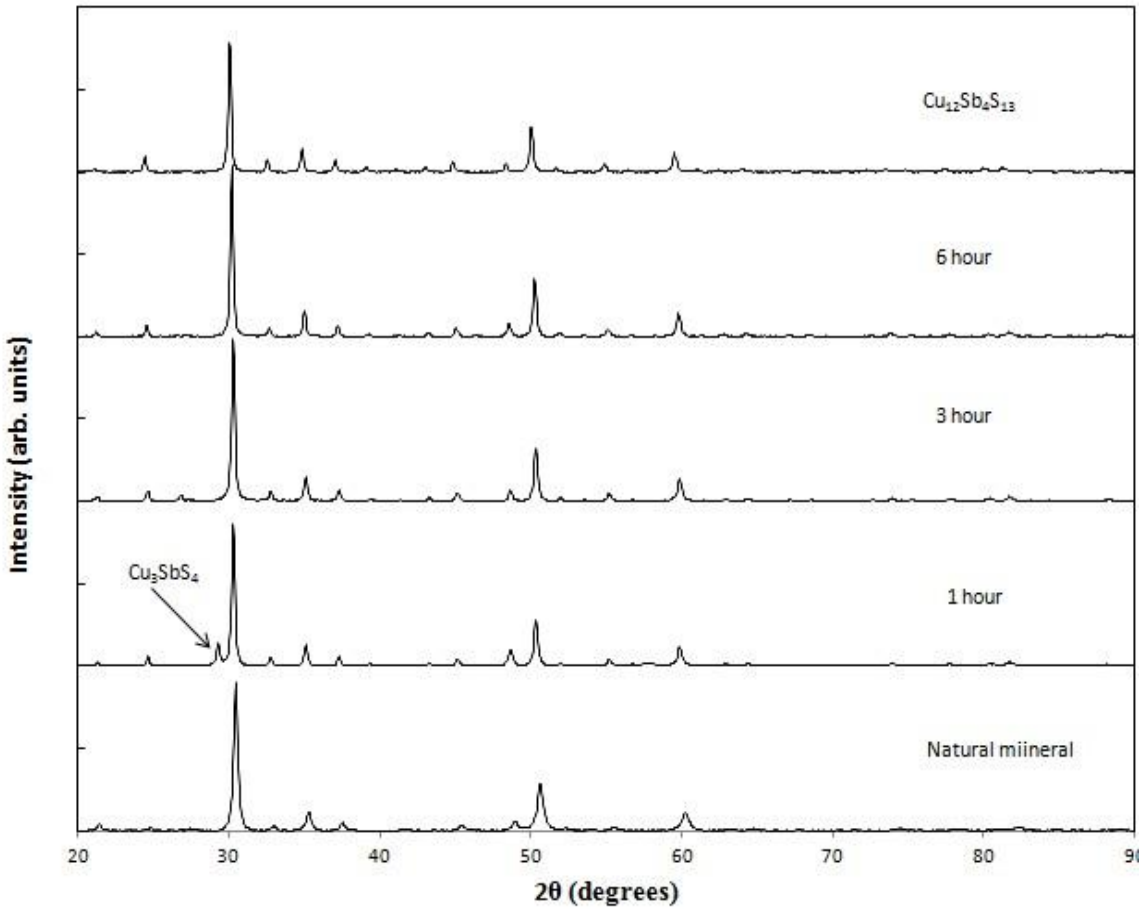

Figure 50 X-ray diffraction patterns for tetrahedrite samples with 50 wt% pure element addition in function of ball milling time.

When the ball milling time is increased to 3 hours, this impurity phase of Cu_3SbS_4 becomes minute; after six hours of milling, the sample is almost exclusively tetrahedrite structure with only a trace amount of Cu, which we observe in all of the ball milled samples. These XRD patterns thus show that that milling the elemental powders for three to six hours is sufficient to form single phase tetrahedrite solid solution in the presence of the natural mineral. To verify the

role of the natural mineral as a "seed matrix" for the formation of single phase tetrahedrite structure, we ball milled the pure elements by in the ratio of 12:4:13 without the presence of the natural mineral. After 6 hours of ball milling, the final product has at least 50% Cu_3SbS_4. Therefore, we reach the conclusion that natural mineral serves as a parent matrix, efficiently absorbing Cu, Sb, and S elements into the crystal structure, altering its composition but maintaining its single phase tetrahedrite character.

SEM images of fracture surfaces of a disk hot pressed using powder consisting of 50% elements and 50 % natural mineral as a function of ball milling time are shown in Figure 51. As the ball milling time is increased from one to three hours, the average grain size is reduced from 330 nm to 180 nm; milling for six hours, however, reduces the grain size to only 150 nm. Detailed EDS mapping results (shown in Figure 52) show that all of the major elements are homogenously distributed in the sample without any sign of segregation. It is quite remarkable that, while forming the tetrahedrite phase by synthesis directly from the elements requires a very extended anneal (one week or longer), the elements can be incorporated readily into the natural mineral tetrahedrite matrix within a few hours simply by mechanical alloying.

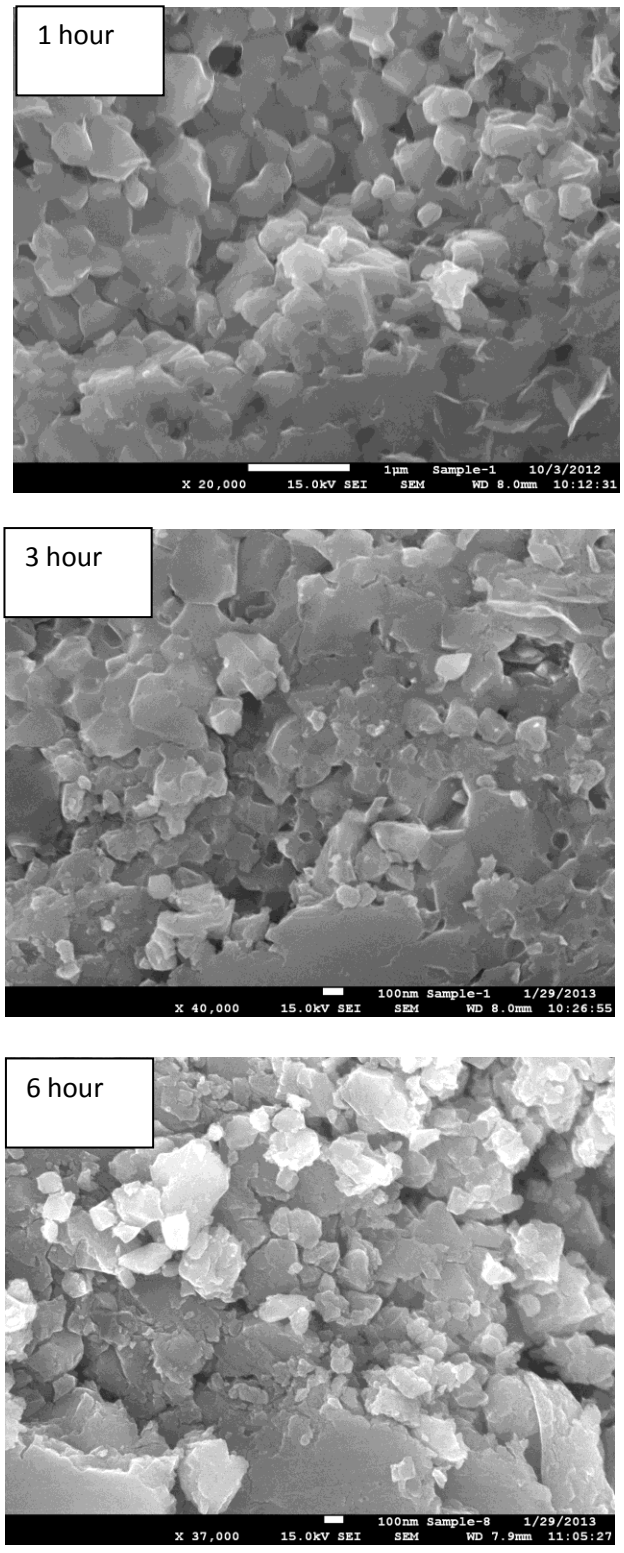

Figure 51 SEM images for a samples with 50%wt pure element addition in function of different ball milling time.

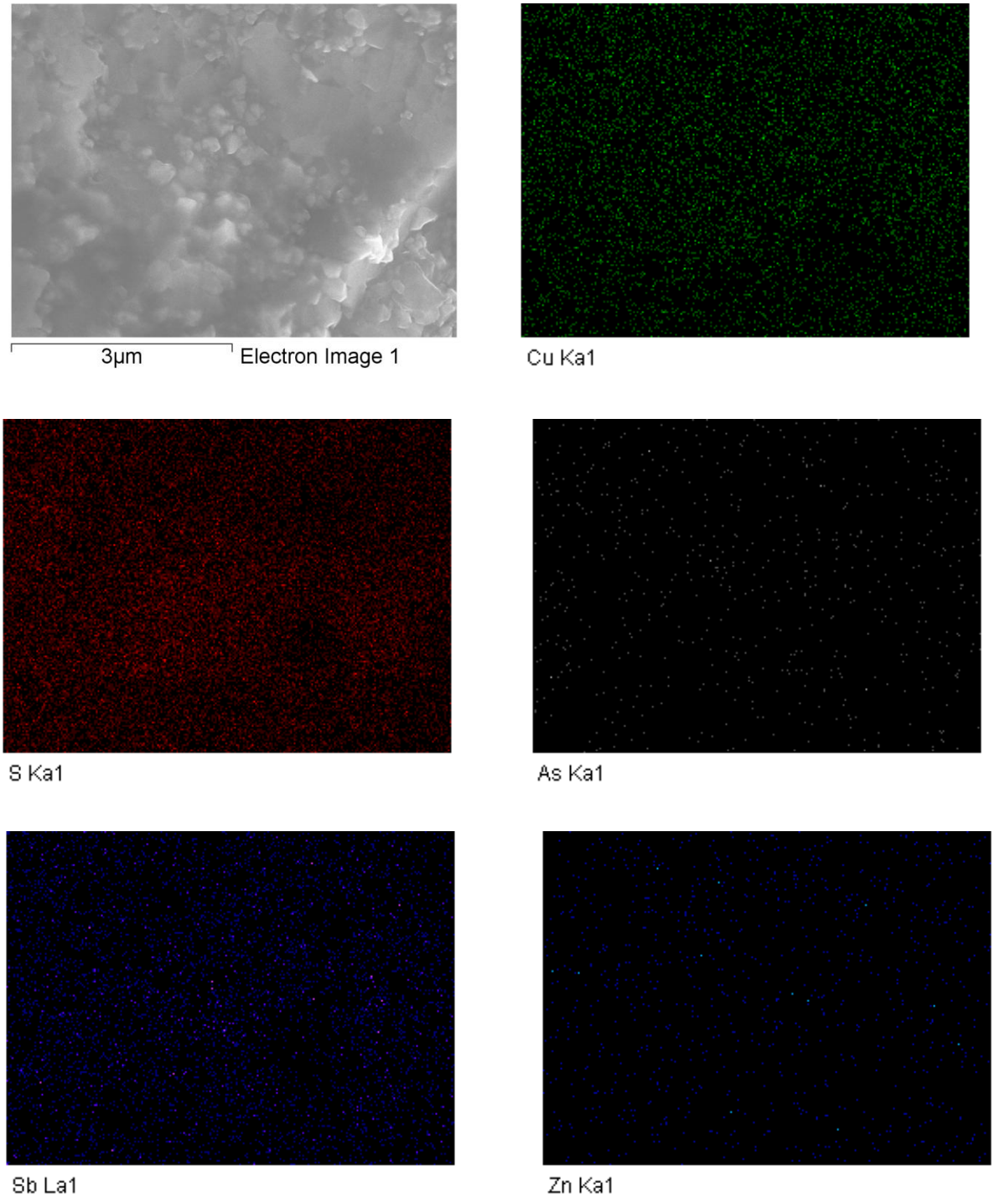

Figure 52 EDS analysis of atomic distribution maps of different elements in 50%-6h specimen.

Figure 53 shows the temperature dependence of the electrical transport properties of the mixture of natural mineral and pure elements after ball milling and consolidation. Samples with 25 wt% and 50 wt% pure elements added to the natural mineral for different ball milling time were investigated. We use a simplified notation to describe different samples. For example, 50%-3 hour means the ample has 50 wt% pure elements addition and a three hour ball milling time. As mentioned above, the Zn(Fe) substitution value of the natural mineral we used in this study is close to two and thus it is insulating with Fermi level in the wide band gap. Notably, by adding Cu into the natural mineral (along with stoichiometric amounts of Sb and S), we are able to move the Fermi level back down close to the top of the valence band in order to optimize the transport properties. The resistivity of samples with 50 wt% pure element addition is a 5-6 times smaller than that of 25 wt% element addition samples. Increasing the ball milling time from one to three hours reduces the resistivity for a given composition since the additional milling suppresses the amount of the impurity Cu_3SbS_4 phase. When the ball milling time was extended to six hours, the resistivities increase for both 25 wt% and 50 wt% additions, which is typical for ball milling synthesis with extended ball milling time. The contamination from the milling media and wear on the jar, an increased density of nanosized defects on the surface of grains and strain in the crystal lattice induced by ball milling may all contribute to the degradation of electrical properties.

The amount of pure element addition also has significant effect on the Seebeck coefficient, which is shown in Figure 53. For the 25 wt% element addition samples, the Seebeck coefficients are all between 250 and 300 μV/K while for 50 wt% element addition samples, the Seebeck coefficients are reduced to 150-200 μV/K due to an increase in carrier concentration. The power factor results indicate that the 25% pure element addition samples have a maximum value of

power factor of 3 μW/cm*K^2 with three hour ball milling. For the 50% pure element addition samples with six hours of ball milling, the degradation of electrical conductivity is offset by enhancement of the Seebeck coefficient, and the power factor remains at a high value of 5.8 μW/cm*K^2. Therefore, the ball milling time can be extended without degrading power factor if more pure elements are added for ball milling.

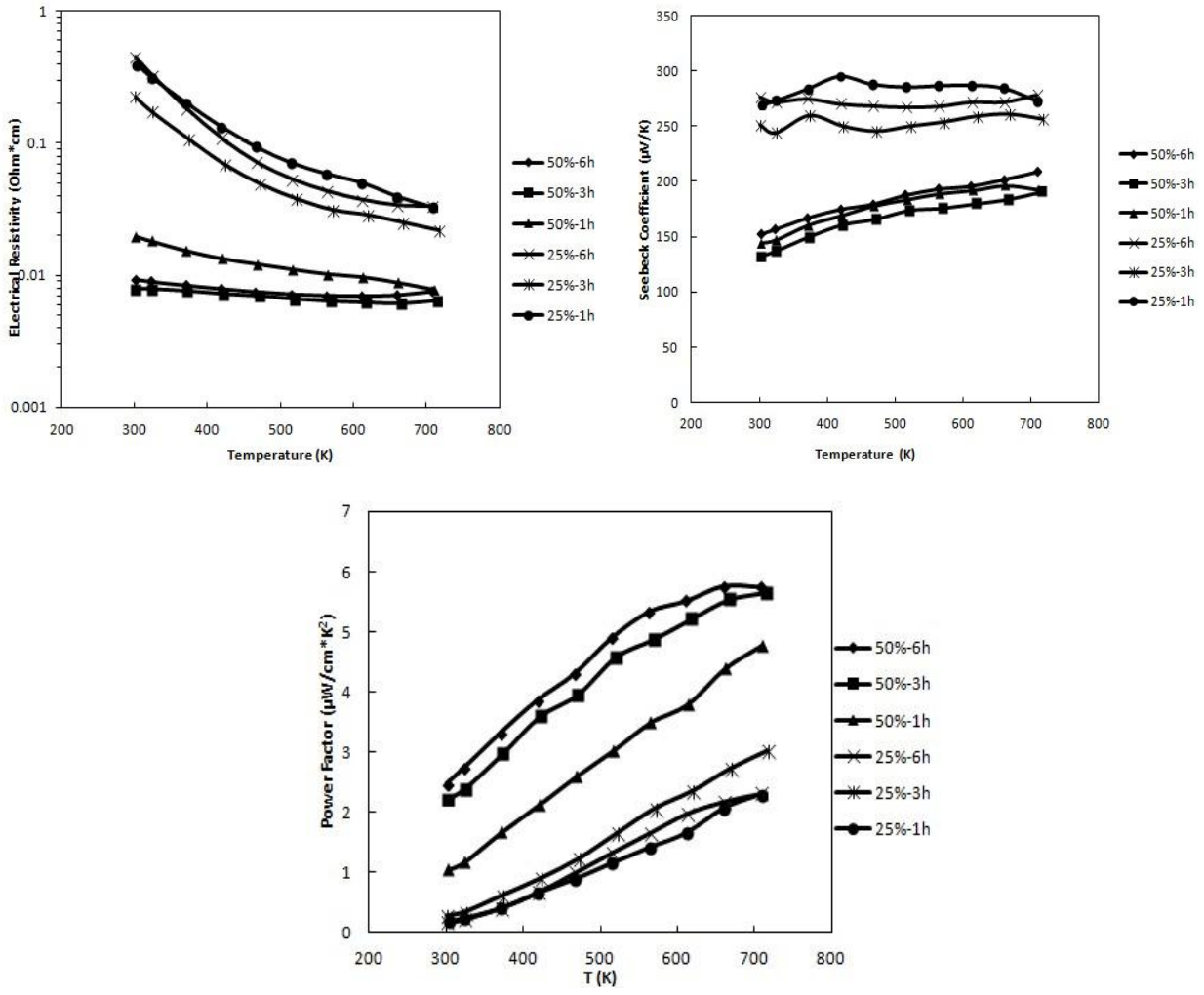

Figure 53 Temperature dependence of electronic transport properties of all ball milling tetrahedrite samples.

Figure 3(d) shows the temperature dependence of total thermal conductivity of all samples. The 25 wt% element addition samples have a weakly temperature dependent thermal conductivity with values in the range of 0.3 - 0.4 W/m*K, indicating the intrinsic low lattice thermal conductivity from tetrahedrite structure dominates. In contrast, the total thermal conductivity of the 50 wt% addition samples increases significantly with increasing temperature since these samples have much lower resistivity and thus a larger electronic thermal conductivity contribution that increases quickly with increasing temperature. At the highest test temperature of 723 K, the total thermal conductivity begins to decline. This same phenomenon was also found in our synthetic tetrahedrite study, and is consistent with the increase in resistivity in this temperature range. Interestingly, although sample 50%-1h has higher resistivity than that of 50%-3h and 50%-6h, it still has higher total thermal conductivity over the entire temperature range. This can be explained by its larger grain size and presence of small amounts of Cu_3SbS_4, which has much higher thermal conductivity than tetrahedrite. The 50%-6h sample has lower total thermal conductivity than that of 50%-3h, resulting from both the reduced electronic part and smaller grain size. Combining the results for the power factor and total thermal conductivity yields the figure of merit *ZT*, shown in Figure 54. The *ZT* value of sample 50%-6h reaches 0.9 at 723 K, which is comparable to other p type TE materials at this temperature. For the 25 wt% element addition samples, *ZT* reaches 0.7 after 3 hours of ball milling. These results indicate that the optimal ball milling time is variable with different amount of pure element addition.

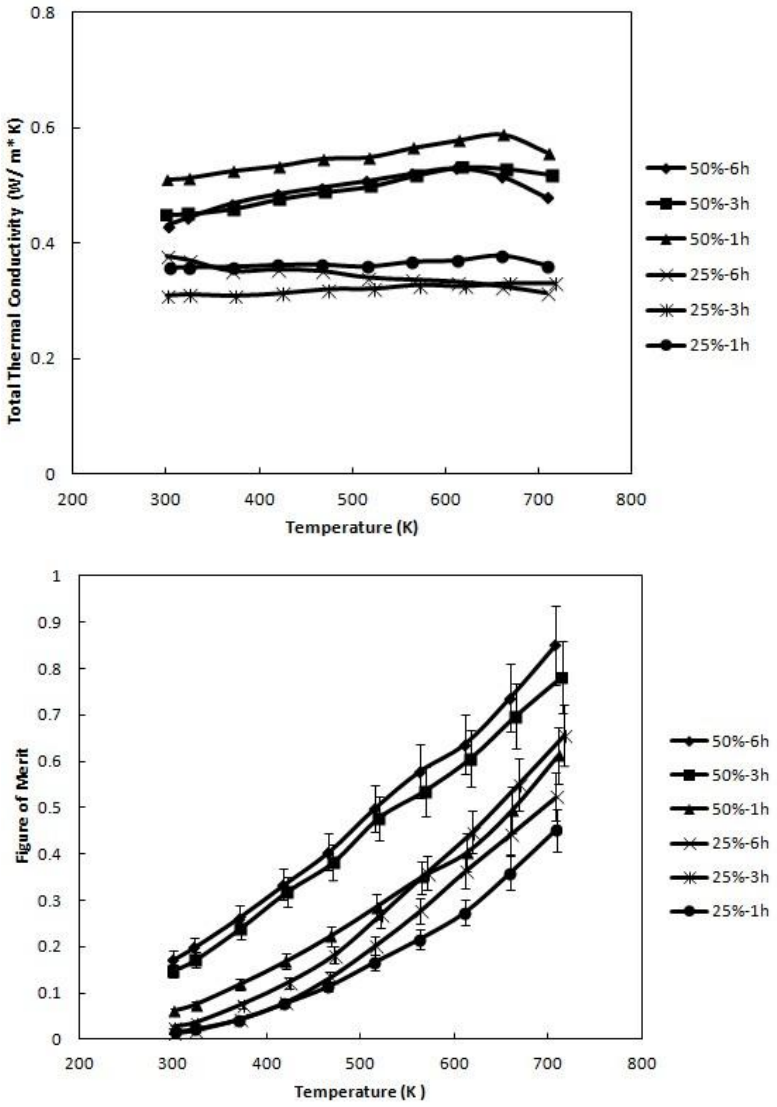

Figure 54 Temperature dependence of total thermal conductivity and figure of merit of all ball milling tetrahedrite samples.

In conclusion, high performance TE materials were synthesized by using natural mineral tetrahedrite and a high energy ball milling method. Nearly single phase tetrahedrite with compositions optimized for thermoelectric performance were obtained after ball milling the natural mineral tetrahedrite and pure elements without additional heat treatment. By adjusting the addition amount of pure elements and ball milling time, a maximum *ZT* value of 0.9 can be

obtained. The high *ZT* value results from the intrinsic low thermal conductivity of the tetrahedrite crystal structure and the small grain size of the pressed pellets. It is believed that the process described here represents the simplest and most economical method for synthesizing high performance TE materials, requiring neither expensive starting materials nor complex synthesis procedures, and thus has great potential for implementation in a wide range of power generation and heat recovery scale applications.

6.3 Summary of the chapter

In summary, we synthesized tetrahedrite based TE materials directly from natural mineral by two methods: i) making solid solution with synthetic $Cu_{12}Sb_4S_{13}$; or ii) high energy balling with pure elements. Both methods give rise to high performance TE materials with maximum *ZT* of 0.9, which is comparable to the best synthetic samples we carefully synthesized in previous chapters. Considering the cost and convenience of directly using natural minerals as source for TE materials, these methods have great potential in real-market applications.

Chapter 7 Phase Stability, Crystal Structure and TE Properties of $Cu_{12}Sb_4S_{13-x}Se_x$ Solid Solution

Among all the compositions synthesized in this work, both synthetic and natural mineral mixed, the pure synthetic sample $Cu_{12}Sb_4S_{13}$ is always reported to have highest power factor. Any substitution on Cu sites will cause a degradation of power factor. The simultaneous decoupling of electrical resistivity and Seebeck coefficient along with lattice thermal conductivity in power factor enhancement has been still challenging for the most of TE materials [93]. Here we have studied thermoelectric properties of $Cu_{12}Sb_4S_{13-x}Se_x$ solid solution, showing a 30% enhancement in power factor for the x = 1 composition at 700 K. The observed "decoupling" effect in electrical resistivity, Seebeck coefficient and thermal conductivity, which are usually entangled in TE materials, is proved to result from the increased band degeneracy/additional carrier pockets near Fermi level. Furthermore, the phase stability and distribution of Se in the solid solution are also investigated by phase diagram calculations and x-ray synchrotron scattering measurements.

7.1 Phase stability and crystal structure of $Cu_{12}Sb_4S_{13-x}Se_x$ solid solution

The $Cu_{12}Sb_4Se_{13}$ phase was recently predicted by Zhang *et al*. [94], to be stable at high temperatures and isostructural with $Cu_{12}Sb_4S_{13}$. Electronic structure and phonon calculations indicated that $Cu_{12}Sb_4Se_{13}$ could be a promising TE material with low thermal conductivity. Our previous attempts to synthesize this compound, however, were unsuccessful, leading us to approach this problem in a more systematic way by investigating the possibility of synthesizing

$Cu_{12}Sb_4S_{13-x}Se_x$ (x = 0, 0.5, 1, 2, 3) solid solutions from the end member of pure tetrahedrite $Cu_{12}Sb_4S_{13}$. All of the solid solutions were synthesized by vacuum melting, long-term heat treatment, and hot pressing described in previous chapters for synthetic tetrahedrites.

Figure 50 shows the (XRD) patterns for $Cu_{12}Sb_4S_{13-x}Se_x$ (x = 0.5, 1, 2, 3). No second phases are detected up to x = 2. A peak shift to the left is observed, indicating an expansion of the unit cell upon substitution of the larger Se ion. For x = 3, two tiny additional peaks appear near the strongest peak, and these remain even after two weeks of heat treatment, indicating an excess substitution of Se over the solubility limit.

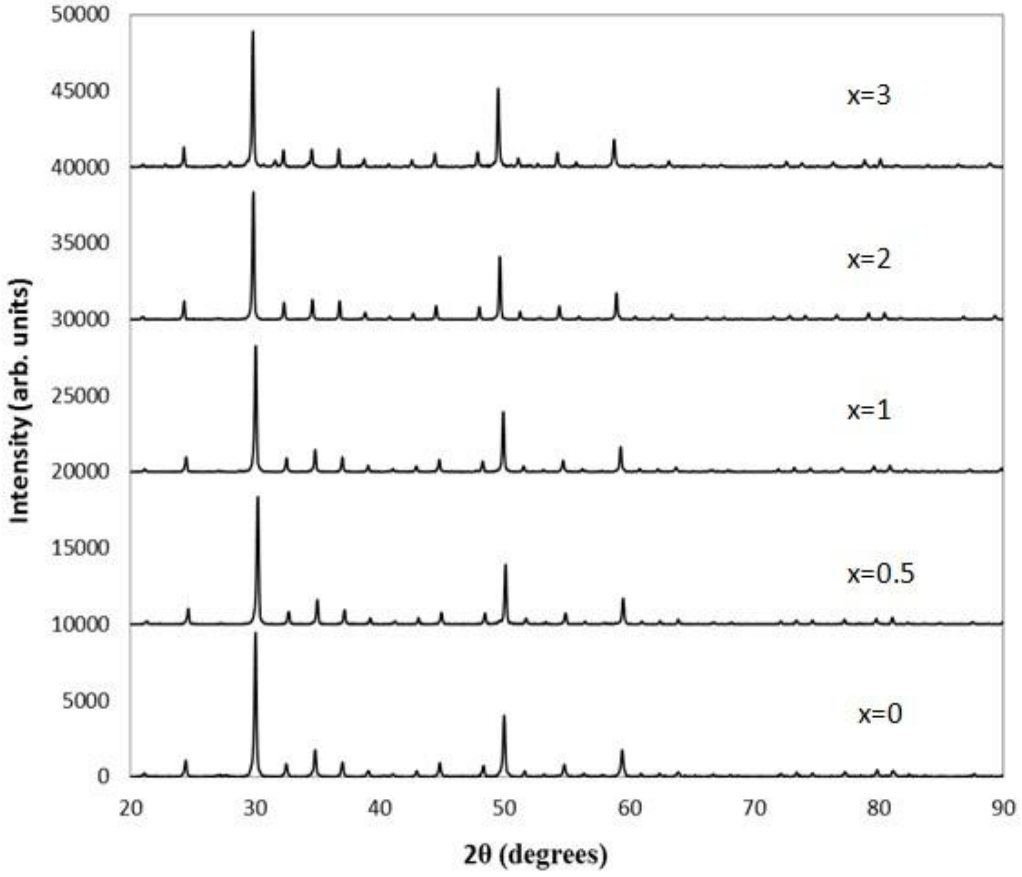

Figure 55 X-ray diffraction patterns for $Cu_{12}Sb_4S_{13-x}Se_x$ (x=0, 0.5, 1, 2, 3) solid solution.

The samples with x = 0 and x = 1 were studied with our collaborators at MSU in more detail using high-resolution X-ray synchrotron (HRXRS). The data were collected at the 11BM beamline at the Advanced Photon Source (APS) at Argonne National Laboratory at 295 K using a wavelength of 0.459004 Å. Rietveld refinement was carried out using the software package Jana2006. For the x = 0 sample, strong anisotropic atomic displacement was found for Cu-12e site (U11: 0.0846 $Å^2$, U22 = U11, U33 = 0.0225 $Å^2$, U12 =-0.0582 $Å^2$, U13 = U23 = 0). These values are similar to those reported earlier for the same compound. Such anisotropic atomic displacement parameters (ADPs) indicate strong out-of-plane vibration of Cu-12*e* site, consistent with that reported for the same compound and Ni-doped sample. For the x = 1 sample, if Se atoms are placed both at the 2*a* and 24*g* site, Rietveld refinement yielded the occupancy of Se at 2*a* site close to zero. This suggests that Se atoms are incorporated into 24*g* site, which is in agreement with the DFT-based energy calculation. Furthermore, stronger out-of-plane vibration was found for Cu-12*e* site in x = 1 sample, from examination of ADPs (U11: 0.0925 $Å^2$, U22 = U11, U33 = 0.021 $Å^2$, U12 = -0.0648 $Å^2$, U13 = U23 = 0). This could contribute to lowering the lattice thermal conductivity of x = 1 sample, as will be discussed in section 7.4.

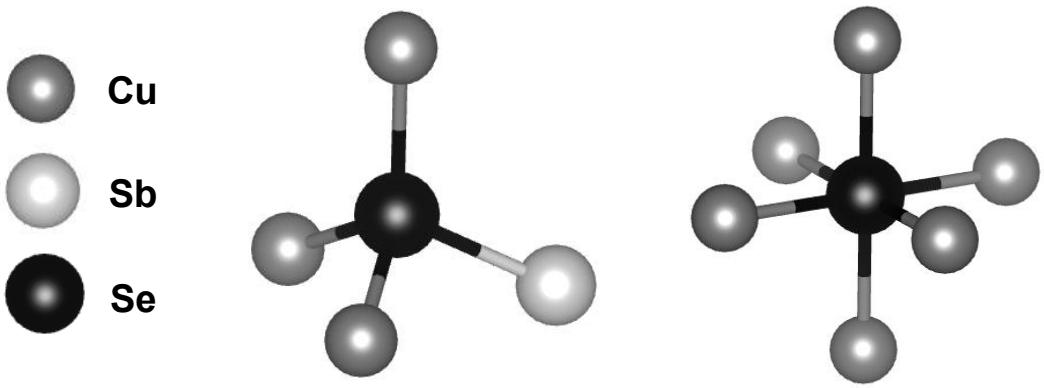

Figure 56 Structure and bonding of the selenium atom substituting for sulfur after full relaxation at the tetrahedral 24*g* (left) and octahedral 2*a* (right) sites respectively.

The fully relaxed structures of Se atom are shown in Figure 56. There are two distinct S sites in tetrahedrite, indicated as S(1) and S(2). The S(1) atoms are tetrahedrally coordinated by Cu (24*g* site), while S(2) is surrounded by six Cu atoms in a regular octahedral arrangement (2*a* site). In the calculations, we considered substitution of Se for S in tetrahedrite on either of these sites. Energy-preferred Se sites were identified by choosing the lowest energy state among all the symmetry-inequivalent configurations. It was found that the tetrahedral 24*g* site is always energy-preferred for Se-substituted tetrahedrite, while substitution on the octahedral site has a positive formation energy.

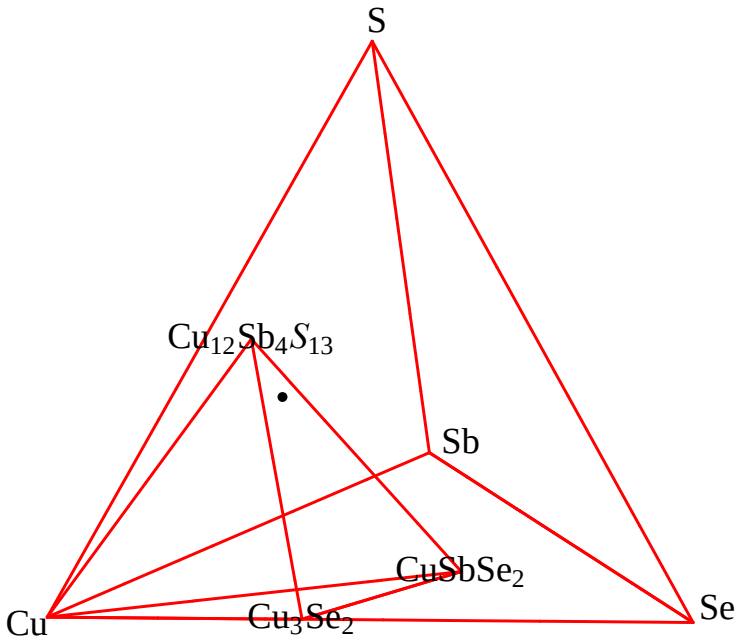

Figure 57 Illustration of quaternary phase diagram and the equilibrium tetrahedron in which Se-substituted tetrahedrite lies. The black point is Se substituted tetrahedrite phase

These experimental results were confirmed by the phase diagram calculations using the methods described in reference 94. The calculated Cu-Sb-S-Se quaternary phase diagram is shown in Figure 57. In this phase diagram, we include elemental, binary and ternary phases and we detect which phase constitutes the equilibrium tetrahedron in which Se-doped tetrahedrite lies

by minimizing the total energy of the these phases. Energy-preferred Se sites were identified by choosing the lowest energy state among all the symmetry-inequivalent configurations. Using this procedure, we find that all Se-substituted tetrahedrite phases lie in the tetrahedron composed of Cu, $Cu_{12}Sb_4S_{13}$, Cu_3Se_2 and $CuSbSe_2$.

The energy difference between the minimized and DFT-calculated total energies of Se-doped tetrahedrite is actually the formation energy and determines directly whether the Se-doped tetrahedrite is stable or not. The formation energy of Se substitution as a function of the number of Se atoms is displayed in Figure 58. One Se atom substitution in the unit cell is energetically favorable, with a formation energy of -47.4 meV/unit cell. The substitution of a second Se atom increases the formation energy rapidly to -23.2 meV/unit cell and upon a third substitution is marginally stable, with a formation energy close to -10 meV/unit cell. Here the trend that formation energy of substitution is approaching zero indicates the $Cu_{12}Sb_4S_{13-x}Se_x$ solid solutions become more unstable with more Se substitution, which explains the occurrence of a second phase in the x = 3 sample.

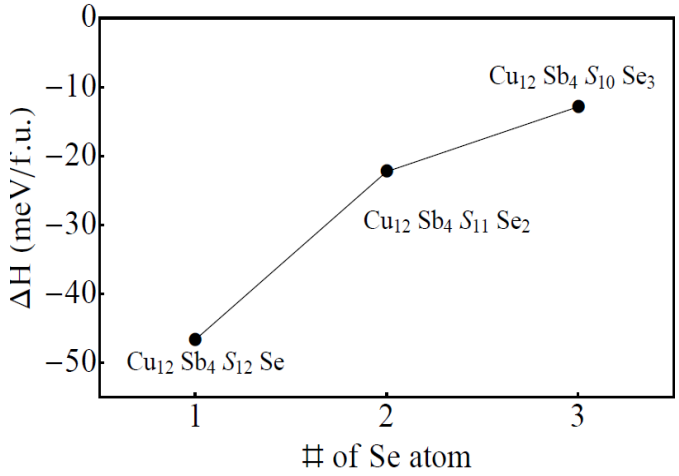

Figure 58 Formation energy per primitive cell as a function of the number of Se atoms in Se substituted tetrahedrite.

7.2 Low temperature electrical transport properties of $Cu_{12}Sb_4S_{13-x}Se_x$ solid solution

Low temperature (3 K-300 K) electrical transport properties measurements were performed on Physical Property Measurement System (PPMS) instruments with collaboration of researchers from Michigan State University and University of Michigan. Figure 59 displays the temperature dependence of resistivity at low temperature. In order to facilitate a more complete discussion of the low temperature transport mechanism, the data of $Cu_{11}ZnSb_4S_{13}$ is also included.

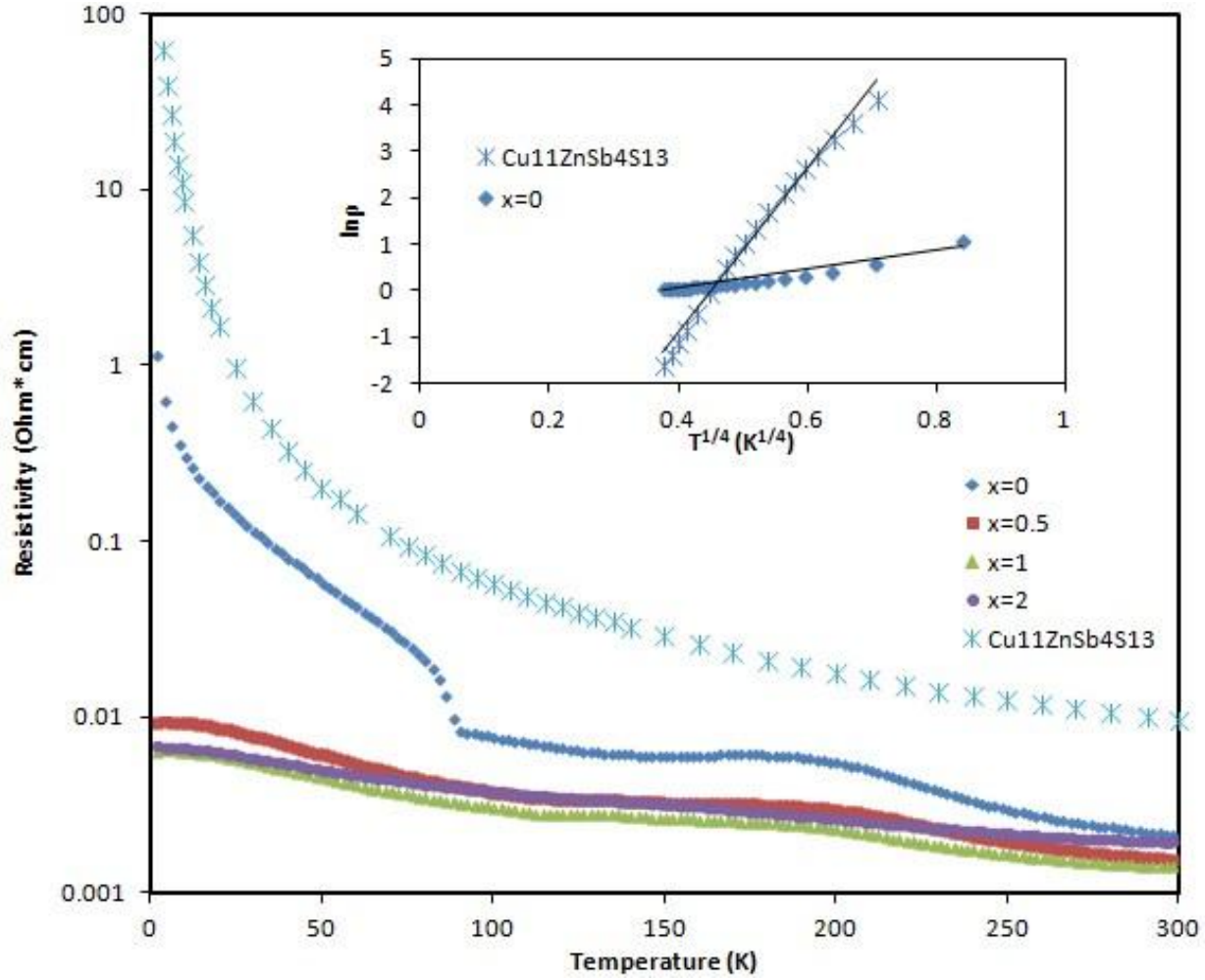

Figure 59 Temperature dependence of electrical resistivity of $Cu_{12}Sb_4S_{13-x}Se_x$ (x = 0, 0.5, 1, 2) solid solution at low temperature.

The electrical resistivity curve of pure $Cu_{12}Sb_4S_{13}$ shows a semiconductor-metal transition between 50 K and 90 K, where resistivity decreases rapidly. This transition is considered as a first order structure phase transition and can be ascribed to the possible rotation of Cu atoms on tetrahedral sites. In order to maintain the threefold axes of the cubic space group, the tilting angle between adjacent tetrahedral Cu atoms will change during the rotation and thus cause the change of unit cell dimension and the structural rearrangement of whole system. Furthermore, at low temperature region (3 K - 50 K), the $ln\rho$ curves of pure $Cu_{12}Sb_4S_{13}$ and $Cu_{11}ZnSb_4S_{13}$ show a linear relationship with respect to $T^{1/4}$, which is a typical temperature dependence of three-dimensional variable-range-hopping (VRH) conduction mechanism described by equation 28. The detailed plot of the logarithm of the electrical resistivity with respect to $T^{1/4}$ is depicted as inset in Figure 59. A similar mechanism were also found in other Cu containing complex compound like colusites $Cu_{26-x}ZnV_2M_6S_{32}$ (M = Ge, Sn) and chalcogenide spinel $Cu_yFe_4Sn_{12}SX_{32}$ (x = S, Se) [95, 96]. In those compounds, Cu-3*d*/S-3*p* orbitals are at the top of valence band, where the Fermi level is located. For pure synthetic tetrahedrite, some of the Cu atoms on tetrahedral sites are found to be divalent as mentioned in Chapter 2. The random distribution of divalent Cu atoms in tetrahedrite sites results in disorder in system and isolated energy states near the Fermi level, which is believed to be the origin of VRH conduction mechanism observed at low temperature. For the Zn = 1 sample, the substituting Zn atoms will replace divalent Cu atoms but still randomly distribute on tetrahedral sites, maintaining VRH conduction at low temperature. In the high temperature region (200 K-300 K), more band-like states are activated and the resistivity of pure $Cu_{12}Sb_4S_{13}$ and $Cu_{11}ZnSb_4S_{13}$ show a thermally-activated conducting behavior like normal semiconductors. For all three of the Se substituted samples, there are two main differences in the electrical resistivity behavior compared to pure

$Cu_{12}Sb_4S_{13}$. The first observation is the suppression of the structure phase transition; it is speculated that Se atoms, with larger radius, impede the rotation of tetrahedral Cu atoms at low temperature. Secondly, the resistivity of all Se substituted samples is lower than that of pure $Cu_{12}Sb_4S_{13}$ and exhibits band-conduction behavior over the entire temperature region. At the lowest temperatures, the resistivity is decreased by more than two orders of magnitude. As Se and S are in the same column of the periodic table, additional carriers are not expected to be introduced by Se substitution for S in the solid solution. We speculate, rather, that there is an increase in band degeneracy and carrier pocket density near the Fermi level with Se substitution, which provide additional pathways for conduction. With increasing Se substitution content, the resistivity decreases due to increased band degeneracy caused by Se. However, for the x = 2 sample, an increase in electrical resistivity is observed. The electronic transport taking place among multiple bands may cause concomitantly strong inter-valley scattering, reducing the mobility of charge carriers [97]. However, it is also possible, in light of the rapid increase in formation energy for the second Se substitution shown in Figure 53, that there are unsuccessfully substituting Se atoms existing in interstitial sites of x = 2 sample, serving as scattering centers for carrier transport [98]. At room temperature, the resistivity is reduced to $1.39*10^{-3}$ Ohm*cm for the x = 1 sample from $2.12*10^{-3}$ Ohm*cm for pure $Cu_{12}Sb_4S_{13}$.

Temperature dependence of the Seebeck coefficient and power factor of the $Cu_{12}Sb_4S_{13-x}Se_x$ (x = 0, 0.5, 1, 2) solid solution are shown in Figure 60 and Figure 61. The Seebeck coefficient curve of pure $Cu_{12}Sb_4S_{13}$ shows a large "bump" due to the structural phase transition described above. In the low temperature region (3 K-50 K), the Seebeck coefficient of pure $Cu_{12}Sb_4S_{13}$ is in linear with $T^{1/2}$, agreeing with VRH conduction given by equation 34. The fitting of the Seebeck coefficient versus $T^{1/2}$ (3 K-50 K) is displayed in the inset of Figure 60, indicating the

large Seebeck coefficient at this region is due to hopping of holes. The Seebeck coefficients of the Se substituted samples suggest band-like conduction, where Seebeck coefficient increases linearly with increasing temperature.

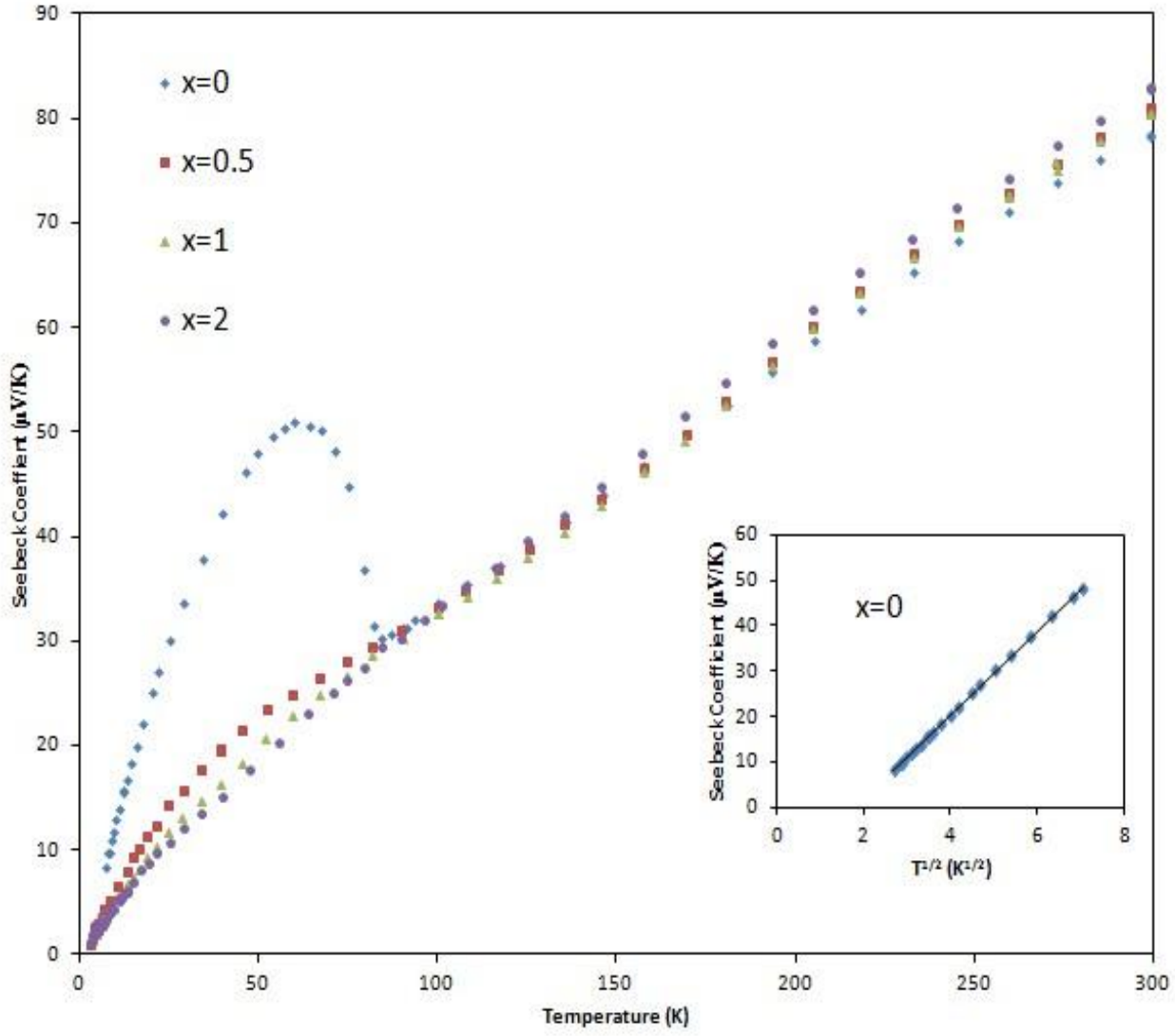

Figure 60 Temperature dependence of Seebeck coefficient of $Cu_{12}Sb_4S_{13-x}Se_x$ (x = 0, 0.5, 1, 2) solid solution at low temperature.

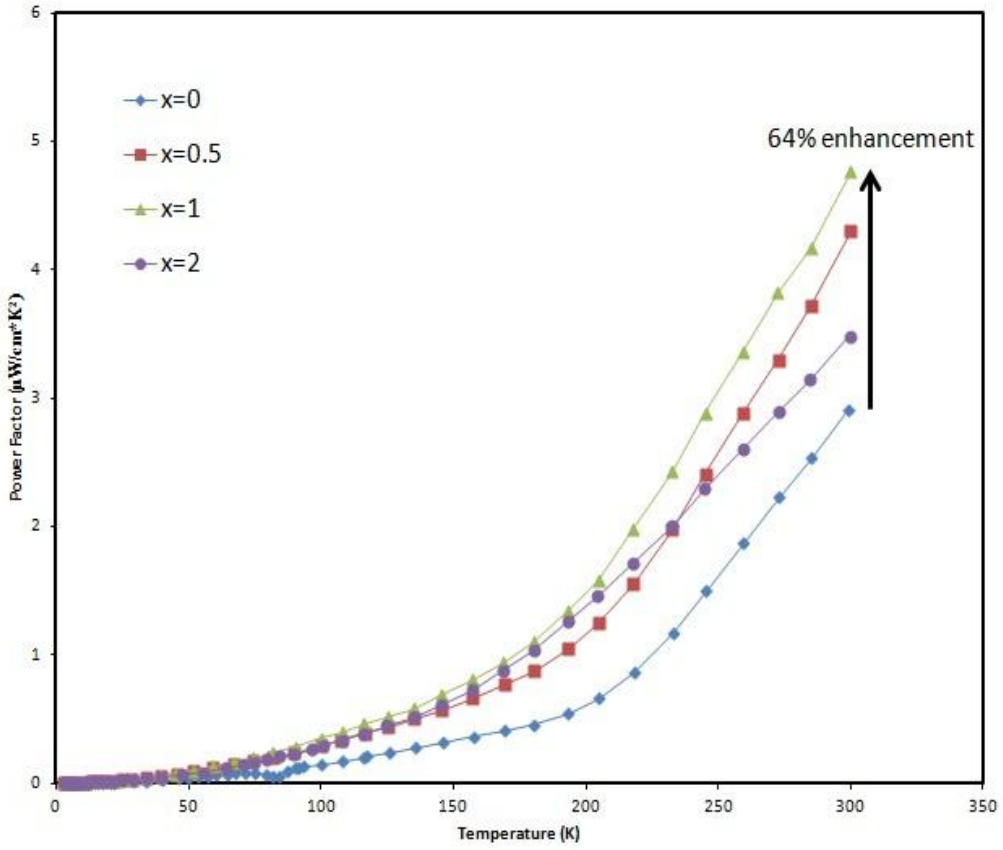

Figure 61 Temperature dependence of power factor of $Cu_{12}Sb_4S_{13-x}Se_x$ (x = 0, 0.5, 1, 2) solid solution at low temperature.

More interestingly, the Seebeck coefficients of the Se substituted samples do not decrease with respect to Se content. Inherently, the Seebeck coefficient and electrical resistivity are both related to carrier concentration, exhibiting a coupled relationship in most materials. This can also be explained by the assumption that the substitution of one Se atom in the tetrahedrite unit cell introduces an additional valence band close to the Fermi level, providing an additional pathway for charge carrier transport without altering the Seebeck coefficient [99, 100]. The Seebeck coefficient is unchanged, since Se substitution for S does not alter the Fermi level, which determines the Seebeck coefficient. This same mechanism involving increased band degeneracy

has recently been reported in PbTe/PbSe and $Mg_2Si_{1-x}Sn_x$ solid solutions. Combining the decreased electrical resistivity and unchanged Seebeck coefficient, the power factors of all Se substituted samples are enhanced. The largest enhancement is found for x = 1 sample, a 64% increase compared to that of pure sample at 300 K.

7.3 Electronic structure of $Cu_{12}Sb_4S_{13-x}Se_x$ solid solution

The above experimental results suggest some interesting changes in electronic structure, specifically an increase in band degeneracy near the Fermi level, of tetrahedrite under Se substitution. In order to investigate this, DFT electronic structure calculations were performed. The results are shown in Figure 62.

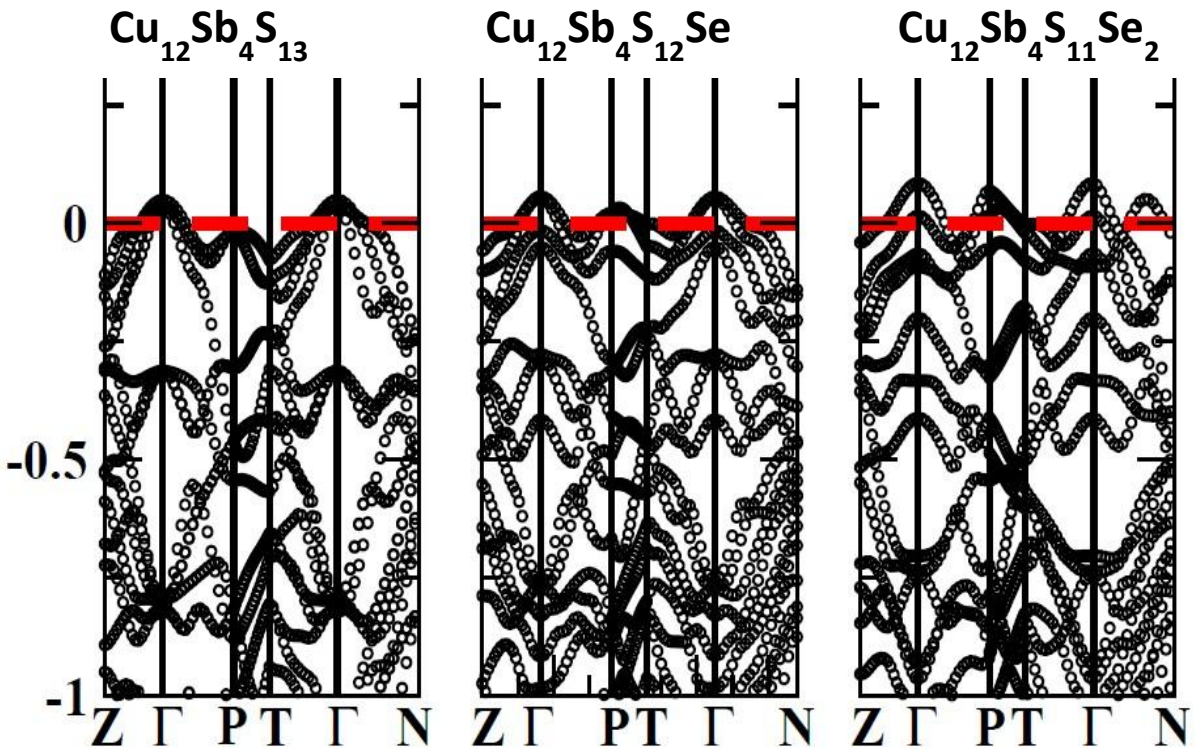

Figure 62 Electronic band structure of $Cu_{12}Sb_4S_{13-x}Se_x$ (x = 0, 1, 2) solid solution.

For pure $Cu_{12}Sb_4S_{13}$, the Fermi level is located close to the top of valence band, which means the density of states is finite at low temperatures, since in DFT calculation the system is assume to be at 0 K. In a typical crystalline material, this suggests that pure $Cu_{12}Sb_4S_{13}$ should be a metallic compound at low temperature with electrical resistivity tending to a finite small value, since the resistivity depends only on those carriers that have energies near the Fermi level and on their interaction with phonons and impurities. However, this is quite different from the experimental observation that pure $Cu_{12}Sb_4S_{13}$ has quite large resistivity at low temperature. Taking the disordered divalent Cu atoms into account as described above, the system should rather be considered as a non-crystalline system at low temperature. In that case, the states with energies near the Fermi level are localized, conduction will be by hopping, and the resistivity will tend to infinite values as exp(constant/$T^{1/4}$), as indicated by the fitting in figure 59. In addition, the energy difference between the Gamma and P points is 70 meV. In general, the condition for two bands to be degenerate is that their energy difference should be within $\sim 2k_BT$ of each other, owing to the broadening of Fermi distribution. A simple estimation under this condition requires a 54 meV energy difference at 300 K for Gamma and P bands to be degenerate, lower than the calculated 70 meV, which means only carriers from Gamma band take part in conduction. In this case, the Gamma band dominated by localized Cu *p* states at low temperature contributes to the conduction, causing the observed VRH conduction. With increasing temperature, more band-like carriers in Gamma band are activated by thermal energy . This is the reason why band-like conduction is observed at high temperature for pure $Cu_{12}Sb_4S_{13}$. With one Se atom substituting for S, the valence bands near P rise, closing the energy difference between Gamma and P bands in $Cu_{12}Sb_4S_{12}Se$ at 0 K. Therefore, the electrical resistivity of the Se substituted samples are two orders of magnitude lower at low temperature and behave like

heavily doped semiconductors, since their conduction is governed by P band uplifted by Se substitution. With Se substitution, the degeneracy between Gamma and P bands can occur without thermal- activation. This degeneracy yields additional carrier pathways at the same temperature and same carrier concentration, resulting in the observation that the resistivity of all Se substituted samples is lower than that of pure $Cu_{12}Sb_4S_{13}$ over the entire temperature region. As mentioned above, the increased degeneracy will not affect the Seebeck coefficient, which is determined solely by the location of the Fermi level. For $Cu_{12}Sb_4S_{11}Se_2$, not only the P point but also along Gamma-N, the valence bands are degenerate with the Gamma points. Although the additional carrier pocket along the Gamma-N direction gives rise to more pathways for carriers, the inter-valley scattering and potential impurity scattering caused by more Se substitution will lower the mobility of carriers and prevent a further decrease of the electrical resistivity.

Figure 63 and Figure 64 show the detailed information of the partial density of states from individual atom species, helping to identify contributions from each atom species to the total density of states near the Fermi level. For pure $Cu_{12}Sb_4S_{13}$, as we expect, the tetrahedral Cu (Cu1) *d* orbital and tetrahedral S (S1) *p* orbital compose the main part of the density of states near Fermi level. In $Cu_{12}Sb_4S_{12}Se$, an additional contribution from the Se orbital is added into density of states, changing the electronic band structure shown in Figure 62.

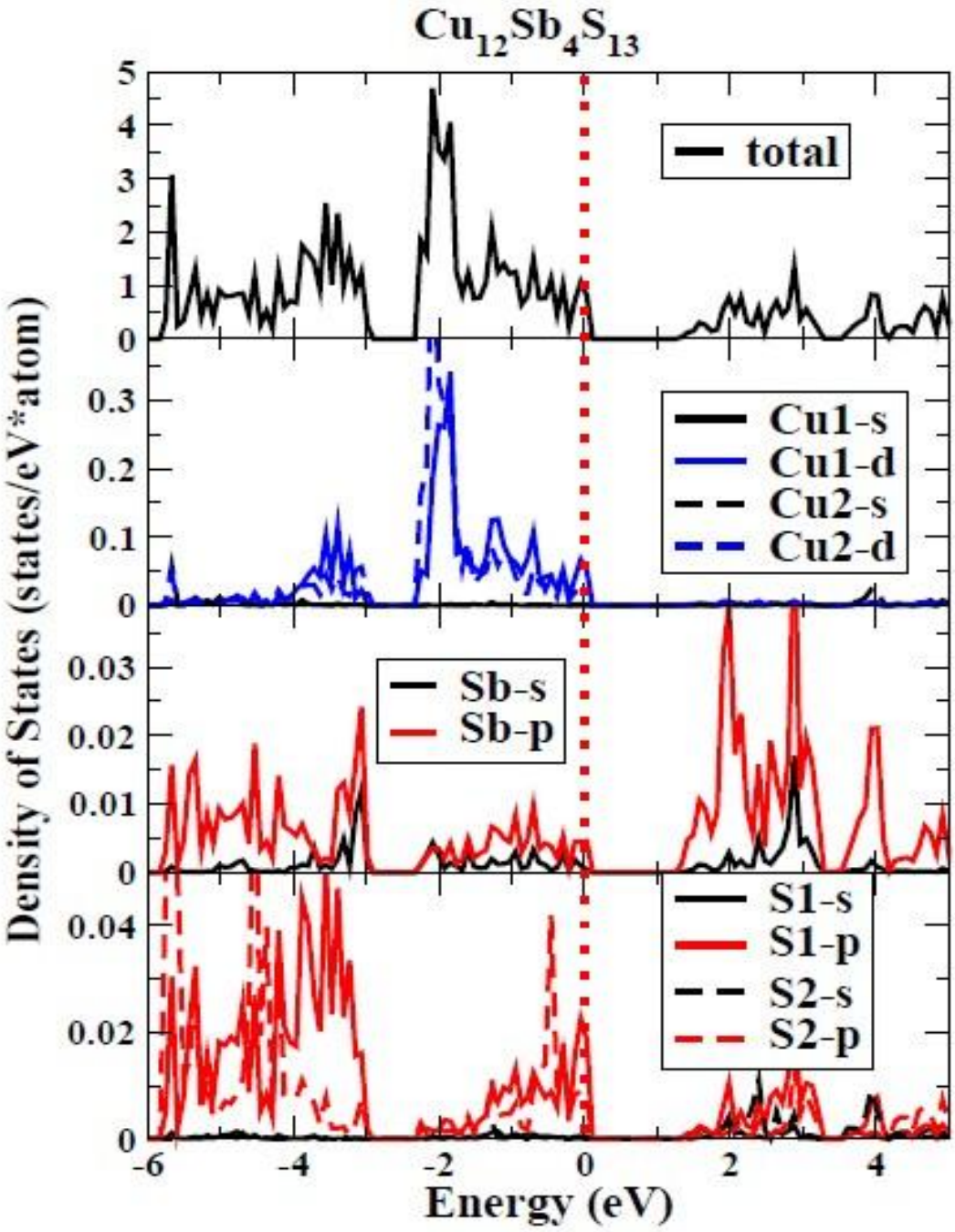

Figure 63 Calculated partial density of states of $Cu_{12}Sb_4S_{13}$.

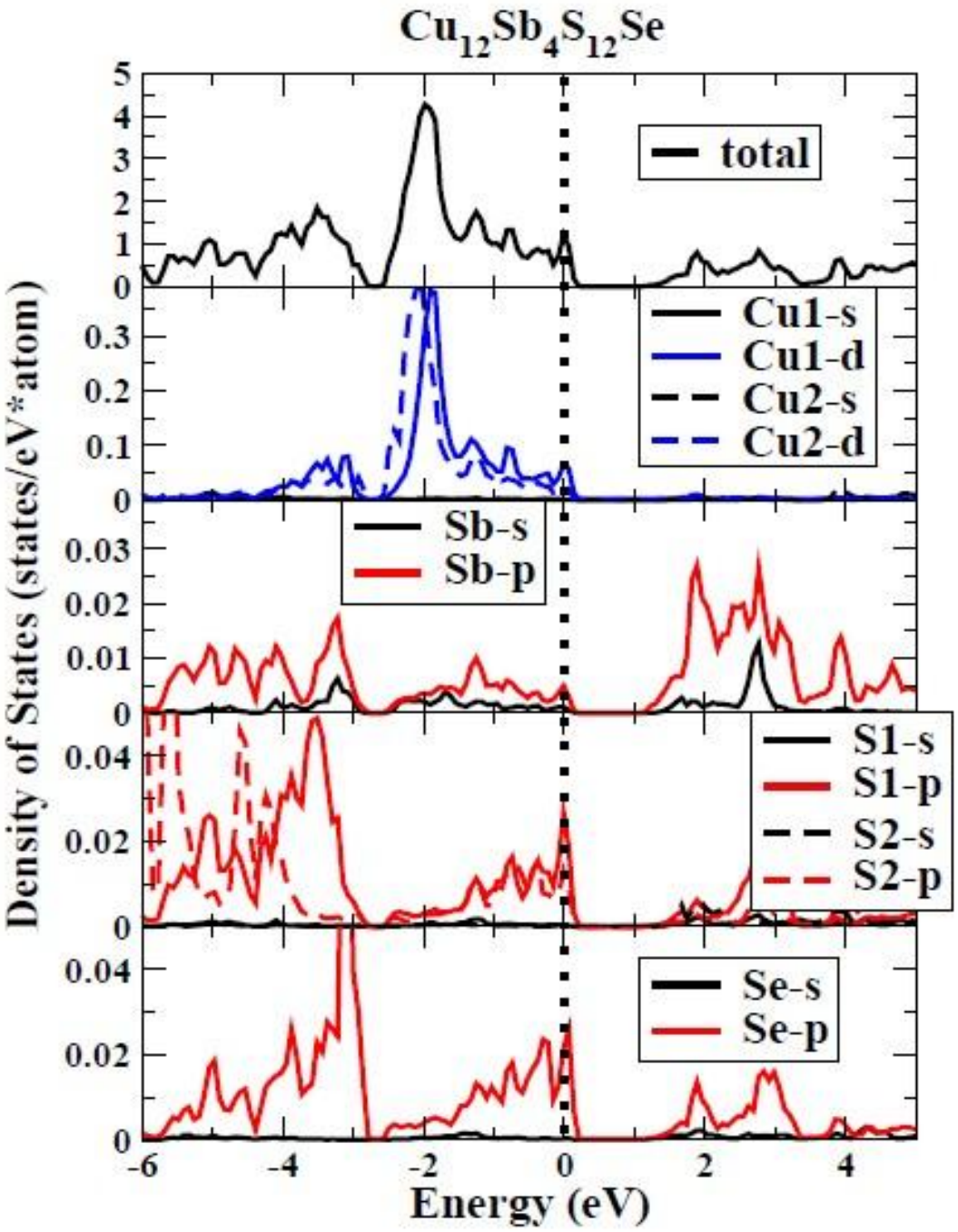

Figure 64 Calculated partial density of states of $Cu_{12}Sb_4S_{12}Se$.

7.4 High temperature TE performance of $Cu_{12}Sb_4S_{13-x}Se_x$ solid solution

The high temperature electrical transport properties of $Cu_{12}Sb_4S_{13-x}Se_x$ (x = 0, 0.5, 1, 2) are shown in Figure 65. The resistivity curves show the same trend as that in the low temperature measurement with respect to Se content. For all the Se substituted samples, the resistivity is reduced over the entire temperature range compared to that of the pure sample. The resistivity of all samples has the same temperature dependent character, first decreasing with temperature from room temperature to 400 K, and then flattening. At high temperatures (600 K- 720 K), the resistivity increases with increasing temperature; in this range, all the carriers have been activated, and carrier-phonon scattering begins to dominate, leading to a decreased mobility and thus increased resistivity. As at low temperature, the high temperature Seebeck coefficients of the Se substituted samples do not change with composition. The power factor reaches a maximum value of 16 $\mu W/cm*K^2$ for the x = 1 sample, a 30% enhancement relative to that of the pure sample.

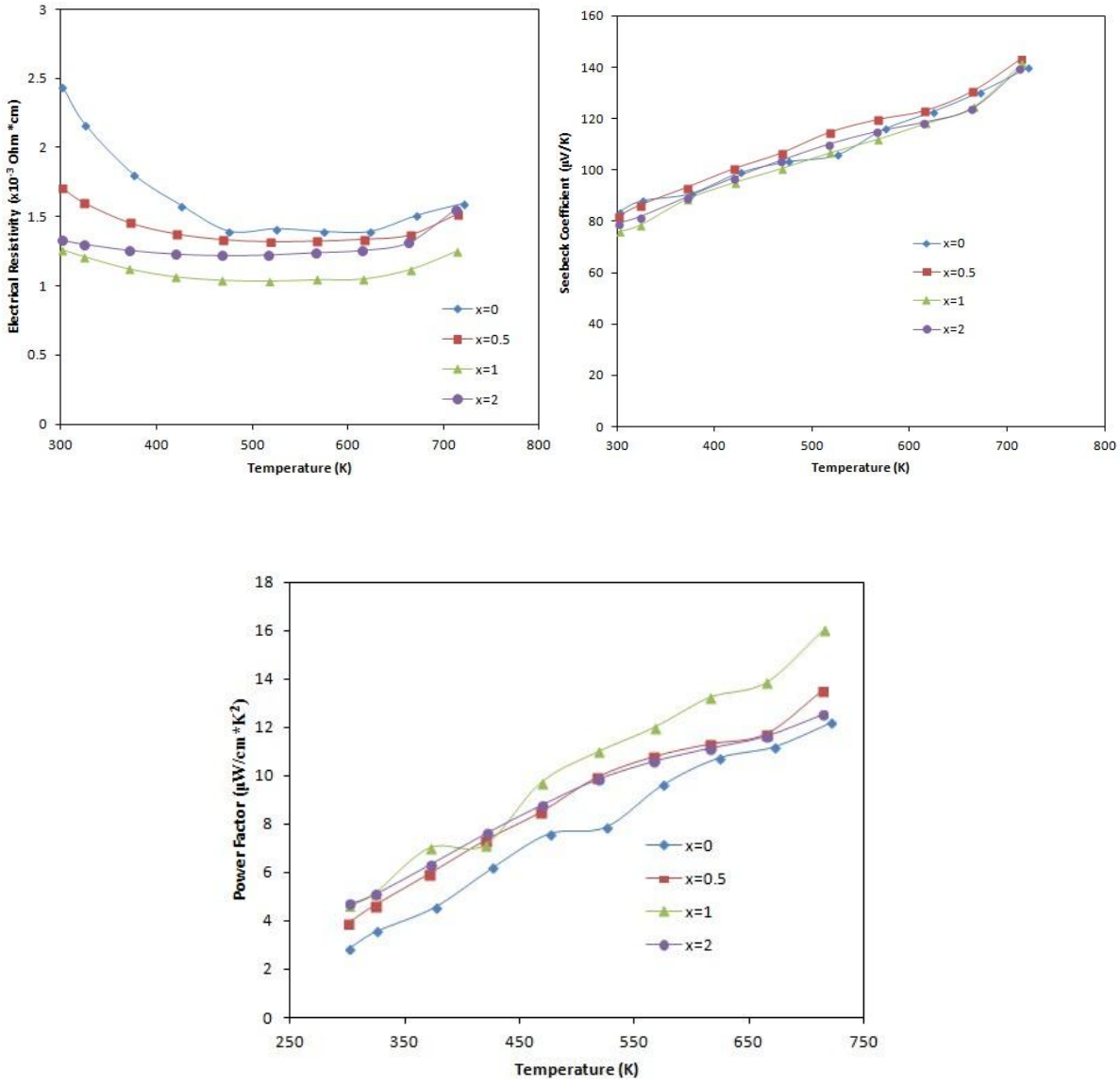

Figure 65 Temperature dependence of electronic transport properties of $Cu_{12}Sb_4S_{13-x}Se_x$ (x = 0, 0.5, 1, 2) solid solution at high temperature.

The total thermal conductivity, lattice thermal conductivity and figure of merit are shown in Figure 66. Again, the samples all display a similar temperature dependence: the thermal conductivity increases from room temperature to 600 K, then begins to fall. This diminution is consistent with a decrease in the electronic contribution of thermal conductivity due to the increasing electrical resistivity shown in Figure 65. Although pure $Cu_{12}Sb_4S_{13}$ has the highest electrical resistivity and thus smallest electronic contribution to total thermal conductivity, all the Se substituted samples have lower total thermal conductivity over the entire temperature range. This implies a large reduction in the lattice thermal conductivity in Se substituted samples. To clarify this, we subtract the electronic thermal conductivity from the total thermal conductivity to estimate the lattice thermal conductivity of $Cu_{12}Sb_4S_{13-x}Se_x$ (x = 0, 0.5, 1). The calculation method for electronic thermal conductivity used here is the same as that described in Chapter 5. The lattice thermal conductivity of $Cu_{12}Sb_4S_{13-x}Se_x$ (x = 0, 0.5, 1), decreases with increasing temperature, which is typical for most TE materials at high temperatures where phonon-phonon scattering dominates. The lattice thermal conductivity is reduced from 0.61 W/m*K to 0.33 W/m*K at 720 K, a value approaching the amorphous limit for tetrahedrite. While the lattice thermal conductivity of all tetrahedrites is low, due to the strong anharmonicity of the lattice vibrational spectrum, Se substitution induces additional scattering of phonons due to the large mass difference between S and Se atoms. The resulting reduction in lattice thermal conductivity compensates for the increase in the electronic portion, further lowering the total thermal conductivity. Thus, Se substitution also successfully decouples the electrical resistivity and total thermal conductivity in tetrahedrite. The combination of increased power factor and reduced total thermal conductivity results in an enhancement of the dimensionless figure of merit shown in Figure 66. The x = 1 sample has the maximum *ZT* value of 0.86 at 720 K, a nearly 40 %

increase over that of $Cu_{12}Sb_4S_{13}$. This value is comparable to that reported for transition metal substituted tetrahedrite, but in this case the increase occurs through and enhancement of the power factor.

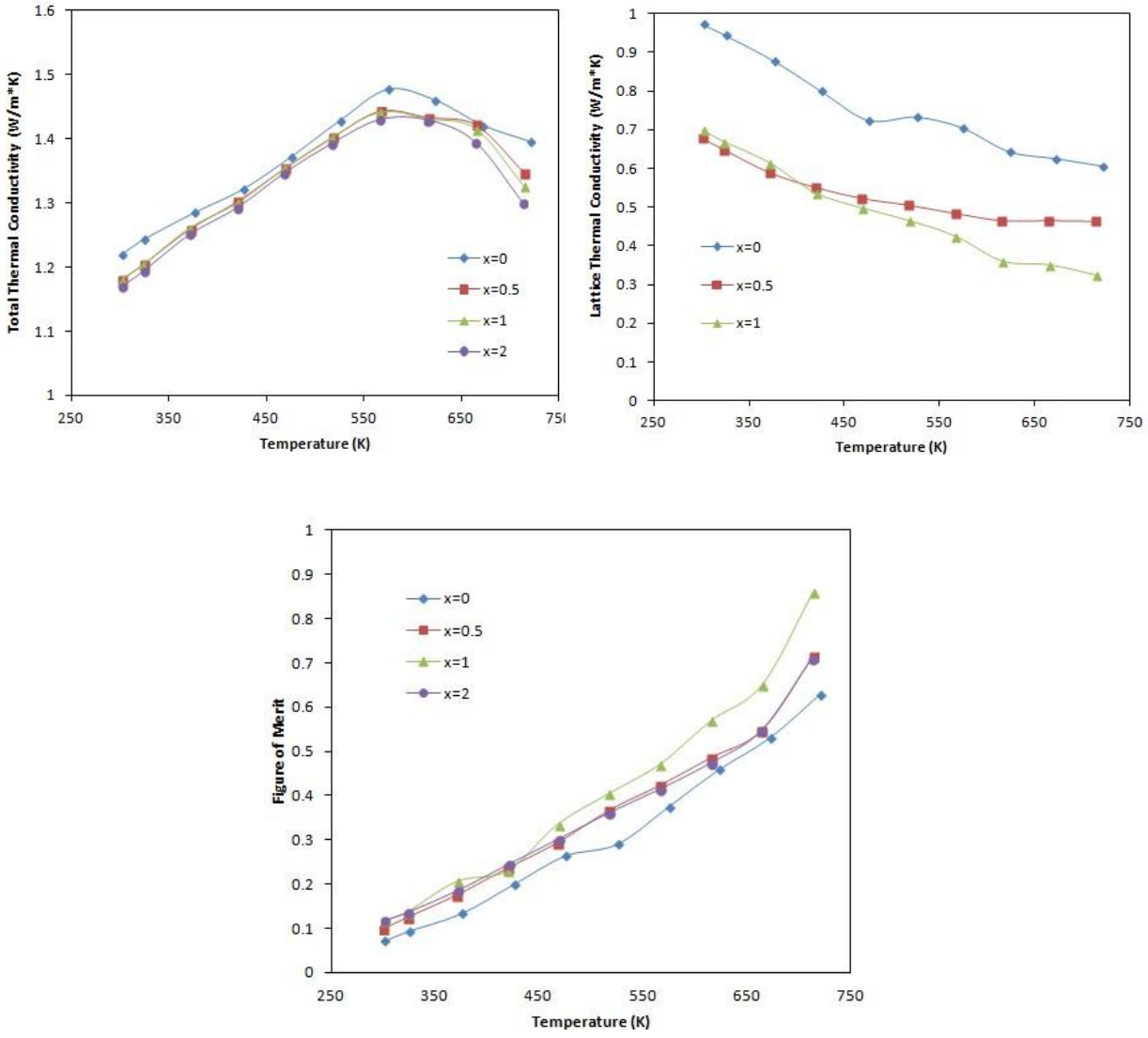

Figure 66 Temperature dependence of total thermal conductivity, lattice thermal conductivity and figure of merit of $Cu_{12}Sb_4S_{13-x}Se_x$ (x = 0, 0.5, 1, 2) solid solution at high temperature.

7.5 Summary of the chapter

In sum, we have presented a new pathway for enhancing figure of merit by decoupling the Seebeck coefficient, electrical resistivity and total thermal conductivity in tetrahedrite through Se substitution. We show that, due to band degeneracy and convergence effects, with Se substitution the electrical resistivity is decreased without diminution of the Seebeck coefficient, leading to an enhanced thermoelectric power factor and thermoelectric figure of merit. Based on these results, it is speculated that further improvement in figure of merit of tetrahedrite can be achieved by co-doping with transition metal elements and Se.

Chapter 8 Conclusions and Future Work

The objective of this work has been to identify natural mineral based TE materials with intrinsically low thermal conductivity, adjustable electronic properties and inexpensive/nontoxic elemental composition. With collaborative work on theoretical calculations and advanced characterization techniques, we have been able to demonstrate that the compound $Cu_{12}Sb_4S_{13}$, which is based on the natural mineral tetrahedrite family, meets the criteria mentioned above and could be a potential p-type TE materials for low-cost, large scale application. After carefully investigating the TE properties of tetrahedrite, we have also developed rapid scalable methods for the synthesis of this material.

The first part of this work is to design TE materials with intrinsically low thermal conductivity. Commonly in TE materials, the dominant portion of thermal conductivity is due to lattice vibrations, or phonons. In the past, many studies have focused on reducing lattice thermal conductivity by creating solid solutions, controlling grain boundaries, and adding nanosized phonon scattering centers, all of which require careful manipulation and are difficult to reproduce consistently. Our approach is to find TE materials which already possess intrinsically low thermal conductivity, so that no further reductions are needed. Based on predictions from our collaborators at UCLA, the compound $Cu_{12}Sb_4S_{13}$ was successfully synthesized, with lattice thermal conductivity approaching the theoretical minimum. Using the neutron scattering facility in ORNL, we have identified several unusual phonon modes that arise due to an anharmonic vibration of Cu atoms in the S trigonal plane, which we believe is the origin of the strong phonon scattering and intrinsically low thermal conductivity.

The second part of this to work has been to explore the modulation of electronic transport properties of TE materials by doping or substitution. Like any semiconductor, the electronic properties of TE materials can be adjusted by doping with various elements. In this work, we have undertaken a systematic study of the doping effects of different elements, including Zn, Fe, Ni, and Te, all of which are found in tetrahedrite when it occurs in nature. For the majority of these elements, additional electrons will be introduced which serve to fill the holes in this p-type semiconductor, thereby increasing electrical resistivity but at the same time enhancing the Seebeck coefficient - a typical coupled effect in TE materials. In addition, the electronic thermal conductivity is also reduced with increasing resistivity. This tradeoff between electronic and thermal properties leads to an optimum doping level. By experimentally varying the doping elements and concentrations, we have proved that TE performance is not sensitive to the doping elements and concentration, but instead depends primarily on the filling fraction of holes. The results indicate that a high *ZT* can be maintained over a wide range of doping levels, with a peak of 0.9 at 700K. Using these findings, we have proposed a new model to evaluate peak *ZT* in terms of the hole filling fraction.

After understanding the independent doping effects of Zn and Ni, Zn and Ni co-doping was performed to both tune the Fermi level closer to the top of the valence band and further reduce lattice thermal conductivity, which a procedure which aids in elevating the figure of merit above unity. Furthermore, we were able to engineer the band structure by substituting Se for S, which leads to a decrease in electrical resistivity without adversely affecting the Seebeck coefficient, causing an overall increase in *ZT*. This decoupling effect is unusual in most TE materials and is ascribed to increased band degeneracy and carrier density of states near Fermi level.

The last part of our work has been to develop a rapid synthesis method of TE materials directly from natural minerals. Following the success in optimizing the tetrahedrite compound, we studied methods to improve and streamline the synthesis of this compound. With the findings that doping levels and specific doping elements were not a critical overall factor, we hypothesized that the naturally occurring mineral, having the same structure as synthetic $Cu_{12}Sb_4S_{13}$ but containing various amounts of impurities, can be used as raw source for TE materials synthesis. It was identified that the naturally occurring specimens show a lower *ZT* than our optimized synthetic samples, as expected, but we that found we could easily modify them to improve performance. The first technique attempted was to grind the natural specimens and mix them with ground synthetic powders; and after hot-pressing this mixture of powders, a sample with the optimized stoichiometry was obtained. The second method adapted was to simply combine the natural rock with high purity raw elements mix them by high energy ball milling, and hot press into a consolidated body. Both methods can produce samples with *ZT* ranging from 0.8 to 1.0. The second method is more efficient and economical, since no synthetic material, which requires melting and long term annealing to produce, is required. Most interestingly, during the process of high energy ball milling, the natural mineral is shown to act as a "seed crystal" for accepting the raw elements into the tetrahedrite matrix, resulting in the desired crystal structure without any additional heat treatment. This allows for large scale material production in very short times.

Future study on tetrahedrites should investigate the possibility to further enhance figure of merit by band structure engineering, which requires careful selection of doping elements and doping levels, supported by theoretical calculations. Nanostructuring of tetrahedrite and other Cu containing compound may be another promising route to enhance their TE properties [101-103].

And so some of the natural mineral based compounds including tetrahedrite show potential for solar cell application [104-106], where future work is needed for further study. It should be noted that like many other copper-containing compounds, pure synthetic $Cu_{12}Sb_4S_{13}$ has at least a small portion of ionic conductivity. The migration of Cu ions in TE materials will deteriorate their performance under large DC electrical current [107-119]. Thus, further study on methods of mitigating ion migration in tetrahedrite will be crucial for advancing these materials to the application stage.

Overall, the idea of directly using natural minerals as raw materials for TE application will help reduce the cost and make large scale waste heat recovery using thermoelectrics a reality. There are still thousands of natural minerals with unknown TE properties that can be explored [110-112]. With the help of powerful calculation tools such as those employed in this work, it is our hope that we will be able in the near future to find more natural mineral based TE materials with high efficiency and low cost, especially an n-type TE counterpart material to match the performance of tetrahedrite.

BIBLIOGRAPHY

BIBLIOGRAPHY

[1] I.B. Cadoff, E. Miller, *Thermoelectric Materials and Devices*, Reinhold Publishing Corporation, New York (1960).

[2] G.S. Nolas, J. Sharp, H.J. Goldsmid, *Thermoelectrics Basic Principles and New Materials Developments*, Springer-Verlag Berlin Heideberg, New York (2001).

[3] A. Shakouri, *Annual Review of Materials Research* **41**, 399 (2011).

[4] C.B. Vining, *Nature Materials* **8**, 83 (2009).

[5] T.M. Tritt, *Annual Review of Materials Research* **41**, 433 (2011).

[6] T.C. Harman, J.M. Honig, *Thermoelectric and Thermomagnetic Effects and Applications*, McGraw-Hill, Inc. (1967)

[7] N.F. Mott, E.A. Davis, *Electronic Processes in Non-Crystalline Materials*, Clarendon Press, Oxford (1979).

[8] J.P. Heremans, V. Jovovic, E.S. Toberer, A. Saramat, K. Kurosaki, A. Charoenphakdee, S. Yamanaka, G.J. Snyder, *Science* **321**, 554 (2008).

[9] O. E. Parfenov, F. A. Shklyaruk, *Semiconductors* **41**, 1021 (2007).

[10] T.M. Tritt, Thermal Conductivity, Theory, Properties and Applications, Kluwer Academic/Plenum Publishers, New York. (2004)

[11] G.A. Slack, S. Galginaitis , *Physical Review* **133**, A253 (1964).

[12] S.D. Mahan, J. O. Sofo, *Proceedings of the National Academy of Sciences USA* **93**, 7436 (1996).

[13] J. P. Heremans, C. M. Thrush, D. T. Morelli, *Physics Review B* **70**, 115334 (2004).

[14] Y.Z. Pei, H. Wang, G. J. Snyder, *Advanced Materials* **24**, 6125 (2012).

[15] Y.Z. Pei , X. Shi , A. LaLonde , H. Wang , L.D. Chen , G. J. Snyder, *Nature* **478**, 66 (2011)

[16] A. F. Ioffe, *Semiconductor Thermoelement and Thermoelectric Cooling*, Infosearch, London (1957).

[17] G. J. Snyder, E.S. Toberer, *Nature Materials* **7**, 105 (2008).

[18] G. A. Slack, in: *Solid State Physics*, edited by H. Ehrenreich, F. Seitz, D. Turnbull, Academic Press, New York (1979).

[19] B.C. Sales, D. Mandrus, R.K. Williams, *Science* **22** 1325 (1996).

[20] G.S. Nolas, G.A. Slack, D.T. Morelli, T.M. Tritt, A.C. Ehrlich, *Journal of Applied Physics* **79**, 4002 (1997).

[21] D.T. Morelli, G.P. Meisner, *Journal of Applied Physics* **77**, 3777 (1995).

[22] X. Shi, J. Yang, J.R. Salvador, M. Chi, J. Y. Cho, H. Wang, S. Bai, J. Yang, W. Zhang, and L. Chen, *Journal of The American Chemical Society* **133**, 7837 (2011).

[23] G. Rogl, A. Grytsiv, E. Royanian, P. Heinrich, E. Bauer, P. Rogl, M. Zehetbauer, S. Puchegger, M. Reinecker, W. Schranz, *Acta Materialia* **61**, 4066 (2013).

[24] G. Joshi, H. Lee, Y. Lan, X. Wang, G. Zhu, D. Wang, R.W. Gould, D.C. Cuff, M.Y. Tang, M.S. Dresselhaus, G. Chen, Z.F. Ren, *Nano Letters* **8**, 4670 (2008).

[25] S. K. Bux, R. G. Blair, P. K. Gogna, H. Lee, G. Chen, M.S. Dresselhaus, R. B. Kaner, J.-P. Fleurial, *Advanced Functional Materials* **19**, 2445, (2009).

[26] L.D. Zhao, J.Q. He, S.Q. Hao, C.-I Wu, T.P. Hogan, C. Wolverton, V.P. Dravid, M.G. Kanatzidis, *Journal of The American Chemical Society* **134**, 16327 (2012).

[27] L.D. Zhao, J.Q. He, C.-I Wu, T.P. Hogan, X.Y. Zhou, C. Uher, V.P. Dravid, M.G. Kanatzidis, *Journal of The American Chemical Society* **134**, 7902 (2012).

[28] K. Biswas, J.Q. He, Q.C. Zhang, G. Y. Wang, C. Uher, V.P. Dravid, M.G. Kanatzidis, *Nature Chemistry* **3**, 160 (2011).

[29] K. Biswas, J.Q. He, I.D. Blum, C.-I Wu, T.P. Hogan, D.N. Seidman, V.P. Dravid, M.G. Kanatzidis, *Nature* **489**, 414 (2012).

[30] D.M. Rowe, *CRC Handbook of Thermoelectrics*. Boca Raton, FL (1995).

[31] M. Zebarjadi, K. Esfarjani, M.S. Dresselhaus, Z.F. Ren, G. Chen, *Energy & Environmental Science* **5**, 5147 (2012).

[32] X. Yan, B. Poudel, Y. Ma,W. S. Liu, G. Joshi, H. Wang, Y. C. Lan, D. Z. Wang, G. Chen and Z. F. Ren, *Nano Letters* **10**, 3373 (2010).

[33] B. Poudel, Q. Hao, Y. Ma, Y. Lan, A. Minnich, B. Yu, X. Yan, D.Z. Wang, A. Muto, D. Vashaee, X. Chen, J. Liu, M.S. Dresselhaus, G. Chen, G. Chen, Z.F. Ren, *Science* **320**, 634 (2008).

[34] X. W. Wang, H. Lee, Y. C. Lan, G. H. Zhu, G. Joshi, D. Z. Wang, J. Yang, A. Muto, M. Y. Tang, J. Klatsky, S. Song, M.S. Dresselhaus, G. Chen and Z.F. Ren, *Applied Physics Letters* **93**, 193121 (2008).

[35] A. D. Lalonde, Y.Z. Pei, G. J. Snyder, *Energy & Environmental Science* **4**, 2090 (2011).

[36] W. Liu, X. Tan, K. Yin, H. Liu, X. Tang, J. Shi, C. Uher, *Physics Review Letters* **108**, 166601 (2012).

[37] H. Gao. T. Zhu. X. Liu, L. Chen, X. Zhao, *Journal of Material Chemistry* **21**, 5933 (2011).

[38] P.F. Qiu, J. Yang, R.H. Liu, X. Shi, X.Y. Huang, G.J. Snyder, W. Zhang, L.D. Chen, *Journal of Applied Physics* **109**, 063713 (2011).

[39] G. Joshi, X. Yan, H. Wang, W. Liu, G. Chen, Z.F. Ren, *Advanced Energy Materials* **1**, 643 (2011).

[40] X. Yan, G. Joshi, W.S. Liu, Y.C. Lan, H. Wang, S. Lee, J.W. Simonson, S.J. Poon, T.M. Tritt, G. Chen, Z.F. Ren, *Nano Letters* **11**, 556 (2011).

[41] G. Kresse, J. Hafner, *Journal of Physical Review B* **47**, 558 (1993).

[42] G. Kresse, J. Hafner, *Journal of Physical Review B* **49**, 14251 (1994).

[43] G. Kresse, J. Furthmüller *Journal of Physical Review B* **54**, 11169 (1996).

[44] J.P. Perdew, K. Burke, M. Ernzerhof, *Physical Review Letters* **77**, 3865 (1996).

[45] J.P. Perdew, K. Burke, M. Ernzerhof, *Physical Review Letters* **78**, 1396 (1997).

[46] A. Migliori, J.L. Sarrao, *Resonant Ultrasound Spectroscopy: Applications to Physics, Materials Measurements, and Non-destructive Evaluation*, Wiley-Interscience, Hoboken (1997).

[47] F. Ren, E.D. Case, J.R. Sootsman, M.G. Kanatzidis, H. Kong, C. Uher, E. Lara-Curzio, R.M. Trejo, *Acta Materialia* **56**, 5954 (2008).

[48] R.D. Schmidt, E.D. Case, G.J. Lehr, D.T. Morelli, *Intermetallics* **35**, 15 (2013).

[49] T.J. Seebeck, *Abh. Akad. Wiss. Berlin* **1820-21**, 289 (1822).

[50] M. Telkes, *American Mineralogist* **35**, 536 (1950).

[51] E. Mackovicky, K. Forcher, W. Lottermoser, G. Amthauer, *Mineralogy and Petrology* **43**, 73 (1990).

[52] S. Fadda, M. Fiori, S.M. Grillo, *Geochemistry, Mineralogy, and Petrology* **43**, 79 (2005).

[53] S. Kitazono, H. Ueno, *Resource Geology* **53**, 143 (2003).

[54] T. Arlt and L.W. Diamond, *Mineralogical Magazine*, **62**, 801 (1998).

[55] A. Pfitzner, M. Evain, V. Petricek, *Acta Crystallographica* **B53**, 337 (1997).

[56] R. Jeanloz, M. L. Johnson, *Physics and Chemistry of Minerals* **11**, 52 (1984).

[57] R.A.D. Pattrick, G.van der Laan, D.J. Vaughan, C.M.B. Henderson, *Physics and Chemistry of Minerals* **20**, 395 (1993).

[58] F. Di Benedetto, G.P. Bernardini, C. Cipriani, C. Emiliani, D. Gatteschi, M. Romannelli, *Physics and Chemistry of Minerals* **32**, 155 (2005).

[59] D.G. Cahill, R.O. Pohl, *Physical Review B* **35**, 4067 (1987).

[60] G.S. Nolas, G.A. Slack, *American Scientist* **89**, 136 (2001).

[61] D.T. Morelli, V. Jovovic, J.P. Heremans, *Physical Review Letters* **101**, 035901 (2008).

[62] E.J. Skoug, J. D. Cain, D.T. Morelli, *Applied Physics Letters* **96**, 181905 (2010).

[63] E.J. Skoug, D.T. Morelli, *Physical Review Letters* **107**, 235901 (2011).

[64] R. Berman, *Thermal Conduction in Solids* Oxford, London (1976).

[65] Y. Zhang, E.J. Skoug, J. Cain, V. Ozoliņs, D.T. Morelli, C. Wolverton, *Physical Review B* **85**, 054306 (2012).

[66] M.D. Nielsen, V. Ozolins, J.P. Heremans, *Energy & Environmental Science* **6**, 570 (2013).

[67] N. W. Ashcroft, N. D. Mermin, *Solid State Physics*, Brooks & Cole (1976).

[68] S. Ganesan, *Philosophy Magazine* **7**, 197 (1962).

[69] X.F. Fan, E.D. Case, X. Lu, D.T. Morelli, *Journal of Material Science* **48**, 7540 (2013).

[70] G. A. Slack, *Solid State Phys*ics **34**, 1 (1979).

[71] D. T. Morelli, J.P. Heremans, *Applied Physics Letters* **81**, 5126 (2002).

[72] D.G. Cahill, S.K. Watson, R.O. Pohl, *Physical Review B* **46**, 6131 (1992).

[73] E. Lara-Curzio, A.F. May, O. Delaire, M. A. McGuire, X. Lu, C-Y. Liu, E.D. Case, D.T. Morelli, *Journal of Applied Physics* **115**, 193515 (2014).

[74] K. Suekuni, K. Tsuruta, T. Ariga, M. Koyano, *Applied Physics Express* **5**, 051201 (2012).

[75] X. Lu, D.T. Morelli, Y. Xia, F. Zhou, V. Ozolins, H. Chi, C. Uher, *Advanced Energy Materials* **3**, 342 (2013).

[76] K. Suekuni, K. Tsuruta, M. Kunii, H. Nishiate, E. Nishibori, S. Maki, M. Ohta, A. Yamamoto, M. Koyano, *Journal of Applied Physics* **113**, 043712 (2013).

[77] J. Heo, G. Laurita, S. Muir, M.A. Subramanian, D.A. Keszler, *Chemistry of Materials* **26**, 2047 (2014).

[78] K. Tatsuka, N. Morimoto, *American Mineralogist* **58**, 425 (1973).

[79] N. Mozgova, V. Mikucionis, V.I. Valiukenas, A. Tsepin, A. Orliukas, *Physics and Chemistry of Minerals* **15**, 171 (1987).

[80] M. Makovicky, K. Forcher, W. Lottermoser, G. Amthauer, *Mineralogy and Petrology* **43**, 73 (1990).

[81] M.L. Johnson, R. Jeanloz, *American Mineralogist* **68**, 220 (1983).

[82] A. G. Trudu, U. Knittel, *The Canadian Mineralogist* **36**, 1115 (1990).

[83] X. Lu, D.T. Morelli, *Journal of Electronic Materials* **43**, 1983 (2014).

[84] W. Liu, X.F. Tang, H. Li, J. Sharp, X.Y Zhou, C. Uher, *Chemistry of Materials* **23**, 5256 (2011).

[85] J. Androulakis, I. Todorov, D-Y. Chung, S. Ballikaya, G.Y. Wang, C. Uher, M. Kanatzidis *Physical Review B* **82**, 115209 (2010).

[86] K. Suekuni, Y. Tomizawa, T. Ozaki, M. Koyano, *Journal of Applied Physics* **115**, 143702 (2014).

[87] A.F. May, E.S.Toberer, A. Saramat, G.J. Snyder, *Physical Review B* **80**, 125205 (2009).

[88] X. Lu, D.T. Morelli, *Physical Chemistry Chemical Physics* **15**, 5762 (2013).

[89] Stefano Fine Minerals, Inc., Ann Arbor, Michigan, USA.

[90] J. Li, J. Sui, Y. Pei, C. Barretean, D. Berardan, N. Dragoe, W. Cai, J. He, L. Zhao, *Energy & Environmental Science* **5**, 8543 (2012).

[91] A. Zevalkink, E.S. Toberer, W.G. Zeier, E. Flage-Larsen, G.J. Snyder, *Energy & Environmental Science* **4**, 510 (2011).

[92] X. Lu. D.T. Morelli, *MRS Communications* **3**, 129 (2013).

[93] P. Puneet , R. Podila , S. Zhu , M.J. Skove , T.M. Tritt , J. He, A. M. Rao, *Advanced Materials* **25**, 1033 (2013).

[94] Y. Zhang, V. Ozoliņs, D.T. Morelli, C. Wolverton, *Chemistry of Materials* **26**, 3427 (2014).

[95] K. Suekuni, F.S. Kim, T. Takabatake, *Journal of Applied Physics* **116**, 063706 (2014).

[96] K. Suekuni, K. Tsuruta, T. Ariga, M. Koyano, *Journal of Applied Physics* **109**, 083709 (2011).

[97] C. Herring, E. Vogt, *Physical Review* **101**, 944 (1956).

[98] I. Kudman, *Journal of Material Science* **7**, 1027 (1972).

[99] Y.Z. Pei, A. D. Lalonde, H. Wang, G. J. Snyder, *Energy & Environmental Science* **5**, 7963 (2012).

[100] D. Bilc, S.D. Mahanti, E. Quarez, K.F. Hsu, R. Pcionek, M.G. Kanatzidis, *Physical Review Letters* **93**, 146403 (2004).

[101] C.H. An, Y. Jin, K.B. Tang, Y.T. Qian, *Chemistry of Materials* **13**, 301 (2003).

[102] J. van Embden, Y. Tachibana, *Journal of Materials Chemistry* **22**, 11466 (2012).

[103] F.J. Fan, B. Yu, Y.X. Wang, Y.L. Zhu, X. J. Liu, S.H. Yu, Z.F. Ren, *Journal of The American Chemical Society* **133**, 15910 (2011).

[104] C. Yan, Z. Su, E. Gu, T. Cao, J. Yang, F.Y. Liu, Y.Q. Lai, J. Li, Y. X. Liu, *RSC Advances* **2**, 10481 (2012).

[105] J. van Embden, K. Latham, N.W. Duffy, Y. Tachibana, *Journal of The American Chemical Society* **135**, 11562 (2013).

[106] C. Tablero, *The Journal of Physical Chemistry C* **118**, 15122 (2014).

[107] H. Liu , X. Shi , F. Xu , L. Zhang , W. Zhang , L. Chen , Q. Li , C. Uher , T. Day , G.J. Snyder , *Nature Materials* **11** , 422 (2012).

[108] Z.H. Ge , B.P. Zhang , Y.X. Chen , Z.X. Yu , Y. Liu , J.F. Li , *Chemical Communications* **47** , 12697 (2011).

[109] G. Dennler, R. Chmielowski, S. Jacob, F. Capet, P. Roussel, S. Zastrow , K. Nielsch, I. Opahle , G. K. H. Madsen, *Advanced Energy Materials* **4**, 1301581 (2014).

[110] J. H. Li, Q. Tan, J.F. Li, *Journal of Alloys and Compounds* **551**, 143 (2013).

[111] P.F. Qiu, T.S. Zhang, Y.T. Qiu, X. Shi, L. D. Chen, *Energy & Environmental Science* DOI: 10.1039/c4ee02428a

[112] Y. He, T. Day, T. Zhang, H. Liu, X. Shi, L. Chen, G. J. Snyder, *Advanced Materials* **26**, 3974 (2014)